UC San Diego
UC San Diego Electronic Theses and Dissertations

Title

Investigation of Cathodes for Next Generation High Energy: Lithium-ion Batteries and Post

Permalink

https://escholarship.org/uc/item/6rv6529d

Author

Zhang, Minghao

Publication Date

2017

Peer reviewed|Thesis/dissertation

UNIVERSITY OF CALIFORNIA, SAN DIEGO

Investigation of Cathodes for Next Generation High Energy: Lithium-ion Batteries and Post

A dissertation submitted in partial satisfaction of the
requirements for the degree Doctor of Philosophy

in

Materials Science and Engineering

by

Minghao Zhang

Committee in charge:

      Professor Ying Shirley Meng, Chair
      Professor Renkun Chen
      Professor Eric E. Fullerton
      Professor Jian Luo
      Professor Yu Qiao

2017

The Dissertation of Minghao Zhang is approved, and it is acceptable in quality and form for

publication on microfilm and electronically:

_____

_____

_____

_____

_____

Chair

University of California, San Diego

2017

iii

DEDICATION

To my parents: Fenglan Xu and Wenbao Zhang, Sujuan Gao and Mingan Bai

To my loving and supportive wife, Shuang Bai

TABLE OF CONTENTS

LIST OF FIGURES

LIST OF TABLES

ACKNOWLEDGEMENTS

This work would not have been possible without infinite support of many. First, I would like to thank my PhD advisor Dr. Ying Shirley Meng for providing me all the opportunities to do this research. It has been an honor working alongside Dr. Meng, whose expertise, understanding, and patience, added considerably to my graduate experience. I appreciate her vast knowledge and skill in many areas (e.g., research, vision, communication, ethics). I would also like to express my deepest gratitude to my committee members: Professor Renkun Chen, Professor Eric E. Fullerton, Professor Jian Luo, and Professor Yu Qiao for their time and guidance.

I am especially grateful for my loving family. I would like to thank my parents, Fenglan Xu and Wenbao Zhang and Sujuan Gao and Mingan Bai, who provided me support through my life. Their love has encouraged and uplifted me through the difficult times. And in particular, I must acknowledge my wife and best friend, Shuang, without whose love, encouragement and assistance, I would not have finished this thesis. She was always there cheering me up and stood by me through the good times and bad. Thank you all for empowering me to be the strong and confident person that I am today.

I would like to express my gratitude to Dr. Miaofang Chi from at Oak Ridge National Laboratory (ORNL). She offered me to intern and work alongside her talented group whose generosity in sharing knowledge, time and expertise in TEM research at a critical stage of my research is greatly appreciated. I also would like to acknowledge my collaborators and co-authors at UC San Diego: Dr. Danna Qian, Dr. Haodong Liu, Dr. Judith Alvarado, Dr. Sunny Hy, Dr. Jing Xu, Mr. Alex C. MacRae, Mr. Thomas Wynn, and Ms. Chengcheng Fang have helped and inspired me in many ways. The Laboratory for Energy Storage and Conversion group (past

and present) members' insight and helpful discussions contributed to a significant portion of this work.

author was the primary investigator and first author of this paper. All of the experiment parts were performed by the author except for the TXM measurement.

Chapter 5, in full, is a reprint of the material "Gas–solid Interfacial Modification of Oxygen Activity in Layered Oxide Cathodes for Lithium-ion Batteries" as it appears in the Nature Communications, Qiu, B.; Zhang, M.; Wu, L.; Wang, J.; Xia, Y.; Qian, D.; Liu, H. D.; Hy, S.; Chen, Y.; An, K.; Zhu, Y.; Liu, Z.; Meng, Y. S., 2016, 7, 12108. The dissertation author was the co-primary investigator and co-first author of this paper. All of the tests were performed and analyzed by the author except for the neutron diffraction and STEM-EELS data. Both Qiu and the author designed and analyzed, and wrote the results.

Chapter 6, in full, is currently being prepared for submission for publication "Structural and Voltage Recovery Driven by Defects Elimination in Li-rich Layered Oxide Cathode", Qiu, B.; Zhang, M.; Liu, H. D.; Wynn, T. A.; Xia, Y.; Liu, Z.; Meng, Y. S. The dissertation author was the co-primary investigator and co-first author of this paper. All of the experiment parts were performed and analyzed by the author except for the neutron diffraction and electrochemical measurement. Both Qiu and the author designed and analyzed, and wrote the results.

Chapter 7, in full, is a reprint of the material "Investigation of Anatase-TiO_2 as an Efficient Electrode Material for Magnesium-Ion Batteries" as it appears in Journal of The Electrochemical Society, Zhang, M.; MacRaea, A. C.; Liu, H. D.; Meng, Y. S., 2016, 163(10), A2368. The dissertation author was the primary investigator and first author of this paper. All of the experiment parts were performed by the author except for the UV−vis spectra.

VITA

2009	Bachelor of Science in Physics
	Nankai University
2012	Master of Engineering in Materials Chemistry and Physics
	Chinese Academy of Sciences
2017	Doctor of Philosophy in Materials Science and Engineering
	University of California San Diego

PUBLICATIONS

(* authors contributed equally to the work)

1. **Zhang, M.***; Yin, K.***;** Hood, Z. D.***;** Bi, Z.; Bridges, C. A.; Dai, S.; Meng, Y. S.; Paranthaman M. P.; Chi, M., "In situ TEM Observation of the Electrochemical Lithiation of N-doped Anatase TiO_2 Nanotubes as Anodes for Lithium-ion Batteries", Journal of Materials Chemistry A, 2017, 38, 20651

2. Yin, K.***; Zhang, M.***; Hood, Z. D.***;** Pan, J.; Meng, Y. S.; Chi, M., "Self-Assembled Framework Formed During Lithiation of SnS_2 Nanoplates Revealed by in Situ Electron Microscopy", Accounts of Chemical Research, 2017, 50 (7), 1495

3. Wang, X.; **Zhang, M.**; Alvarado, J.; Wang, S.; Sina, M.; Lu, B.; Bouer, J.; Xu, W.; Xiao, J.; Meng, Y. S., "New Insights on the Structure of Electrochemically Deposited Lithium Metal and Its Solid Electrolyte Interphase via Cryogenic TEM", ACS Nano Letters, 2017

4. Qiu, B.***; Zhang, M.***; Xia, Y.; Liu, Z.; Meng, Y. S., "Understanding and Controlling Anionic Electrochemical Activity in High-Capacity Oxides for Next Generation Li-Ion Batteries", Chemistry of Materials, 2017, 29, 908

5. Meng, Y. S.; **Zhang, M.**; Liu, H. D.; Qian, D.; Fang, C., "Lithium-excess Cathode Material and Co-precipitation Formation Method", 2017, Patent No. WO2017087403

6. Radin, M. D.; Hy, S.; Sina, M.; Fang, C.; Liu, H.; Vinckeviciute, J.; **Zhang, M.**; Whittingham, M. S.; Meng, Y. S.; Van der Ven A., "Narrowing the Gap between Theoretical and Practical Capacities in Li-Ion Layered Oxide Cathode Materials", Advanced Energy Materials, 2017, 7, 1602888

7. Singer, A.; **Zhang, M.**; Hy, S.; Cela, D.; Fang, C.; Wynn, T. A.; Qiu, B.; Xia, Y.; Liu, Z.; Ulvestad, A.; Hua, N.; Wingert, J.; Liu, H.; Sprung, M.; Zozulya, A. V.; Maxey, E.; Harder, R.; Meng, Y. S.; Shpyrko, O. G., "Nucleation of Dislocations and Their Dynamics in Oxygen Redox Active Cathode Materials During Battery Charging", Nature Energy, 2017, (under review)

8. **Zhang, M.**; Liu, H. D.; Liu, Z.; Fang, C.; Meng, Y. S., "Modified Co-precipitation Synthesis of Meso-structure Controlled Li-rich Layered Oxides for Minimizing Voltage Degradation", 2017, (in preparation)

9. Qiu, B.*; **Zhang, M.***; Liu, H. D.; Wynn, T. A.; Xia, Y.; Liu, Z.; Meng, Y. S., "Structural and Voltage Recovery Driven by Defects Elimination in Li-rich Layered Oxide Cathode", 2017, (in preparation)

10. Meng, Y. S.; **Zhang, M.**; Qiu, B.; Liu, Z., "Structural and Voltage Recovery in Li-rich Layered Oxides", 2017, (patent in application)

11. **Zhang, M.**; MacRaea, A. C.; Liu, H. D.; Meng, Y. S., "Investigation of Anatase-TiO_2 as an Efficient Electrode Material for Magnesium-Ion Batteries", Journal of The Electrochemical Society, 2016, 163(10), A2368

12. Qiu, B.*; **Zhang, M.***; Wu, L.; Wang, J.; Xia, Y.; Qian, D.; Liu, H. D.; Hy, S.; Chen, Y.; An, K.; Zhu, Y.; Liu, Z.; Meng, Y. S., "Gas–solid Interfacial Modification of Oxygen Activity in Layered Oxide Cathodes for Lithium-Ion Batteries", Nature Communications, 2016, 7, 12108

13. Hy, S.; Liu, H. D.; **Zhang, M.**; Qian, D.; Hwang, B.-J.; Meng, Y. S., "Performance and Design Considerations for Lithium Excess Layered Oxide Positive Electrode Materials for Lithium Ion Batteries", Energy & Environmental Science, 2016, 9, 1931

14. Shi, Y.; **Zhang, M.**; Qian, D.; Meng, Y. S., "Ultrathin Al_2O_3 Coatings for Improved Cycling Peroformance and Thermal Stability of $LiNi_{0.5}Co_{0.2}Mn_{0.3}O_2$ Cathode Material", Electrochemica Acta, 2016, 203(10), 154

15. Liu, H. D.; Chen, Y.; Hy, S.; An, K.; Venkatachalam, S.; Qian, D.; **Zhang, M.**; Meng, Y. S., "Operando Lithium Dynamics in the Li-Rich Layered Oxide Cathode Material via Neutron Diffraction" Advanced Energy Materials, 2016, 6, 1502143

ABSTRACT OF THE DISSERTATION

Investigation of Cathodes for Next Generation High Energy: Lithium-ion Batteries and Post

by

Minghao Zhang

Doctor of Philosophy in Materials Science and Engineering

University of California, San Diego, 2017

Professor Ying Shirley Meng, Chair

Recently, anionic activity, oxygen redox reaction, has been discovered in the electrochemical processes, providing extra reversible capacity for lithium-rich layered oxide cathode. However, the huge irreversible capacity loss in the first charge–discharge cycle and voltage degradation during cycling process prevent their utilization in LIBs. Herein, modified carbonate co-precipitation synthesis without addition of chelating agent is introduced to obtain meso-structure controlled Li-rich layered oxides. This unique design not only decreases surface

area compared with the sample with dispersive particles, but also increases overall structure mechanical stability compared with the sample with larger secondary particles as observed by TXM. As a result, the voltage decay and capacity loss during long term cycling have been minimized to a large extent.

Gas–solid interface reaction is designed to achieve delicate control of oxygen activity through uniformly creating oxygen vacancies without affecting structural integrity of Li-rich layered oxides. Theoretical calculations and experimental characterizations demonstrate that oxygen vacancies provide a favorable ionic diffusion environment in the bulk and significantly suppress gas release from the surface. The target material is achievable in delivering a discharge capacity as high as 301 mAh g^{-1} with initial Coulombic efficiency of 93.2%. After 100 cycles, a reversible capacity of 300 mAh g^{-1} still remains without any obvious decay in voltage. We further design a path to remove the defects in the structure of Li-rich layered oxides by high temperature annealing. This treatment recovers the superstructure and average discharge voltage. The novel understanding of the structure metastability and reversibility phenomenon will provide clues for identifying more realistic pathway to fully address voltage decay issue of high-capacity Li-rich layered oxide electrodes.

On the other hand, Magnesium-ion batteries (MIBs) have twofold volumetric energy density than that of lithium without the dendritic deposition morphology associated with Li, which makes MIBs attractive options. We investigate the feasibility of using anatase-phase TiO_2 as an electrode material for MIBs. Electrochemical, microscopic, and spectroscopic analyses are performed in order to probe Mg-ion insertion as well as determine the limitation of TiO_2 as a viable electrode material.

Chapter 1. Motivation and Outline

The energy and material is foundation and driving force of the development of society. With the rapid development of modern society, the huge demand for energy from traditional fossil fuels (oil, coal, natural gas, etc.) leads to dramatic increasing depletion of greenhouse gases. There is an urgent need to develop novel type of energy with less pollution. Therefore, renewable energy sources such as solar energy, wind energy, tidal energy and geothermal energy have attracted extensive attention. At the same time, as an energy conversion and storage device which converts different type of energy into electric energy, battery has a very broad vision for development.

Batteries (including zinc manganese/mercury/silver/air batteries, nickel cadmium batteries, nickel hydrogen batteries, lead-acid batteries, lithium ion batteries, activated batteries, solid electrolyte battery, fuel cell, redox flow battery, etc.) can be divided into two main types according to their usage: primary cells or non-rechargeable batteries, and secondary cells or rechargeable batteries. LIBs as new generation of rechargeable batteries have been widely used in mobile phone, notebook computer, music player and other personal electronic devices for their high specific energy, high operation voltage, wide working temperature, long cycle life.[1] With the expansion of application field, the demand for LIBs put forward higher requirement from the portable electronic devices to electric vehicle (EV) which can to a large extent reduce greenhouse gases release that leads to global warming. For the application of LIBs in EV, the energy density of the mass production is required to achieve at least 300 Wh kg^{-1}, the long-term goal is as high as 500 Wh kg^{-1}, the life cycle is more than 3000 times, and the cost is less than $150 kWh^{-1}.[2] At present, the energy density of the mass produced lithium-ion battery system is mainly around 115-130 Wh kg^{-1}, and the cost is much higher than $200 kWh^{-1}.[3] Therefore, the

energy density and cycling life of LIBs must extend beyond the current reach of commercial electrodes to meet the performance requirements for transportation applications.

As an important component of LIBs, cathode material to a large extent determines the electrochemical performance of the whole battery. It is estimated that if the charge/discharge specific capacity of the cathode material increases by 50%, the power density of the whole battery will increase by 28%.[4] For the cathode materials, the current generation LIBs mainly focused on classical lithium metal oxide layered structure ($LiCoO_2$), lithium iron phosphate ($LiFePO_4$) olivine and spinel lithium manganate ($LiMn_2O_4$).[5] The above three materials are widely used and produced by mainstream power battery manufacturers, but these materials have their intrinsic disadvantages. The high cost of cobalt and the relatively low practical capacity of $LiCoO_2$ ($\sim$ 140 mAh g^{-1}) inhibits its further use in price-sensitive applications.[6] In comparison, despite the abundance of iron and manganese, the capacities of olivine $LiFePO_4$ and spinel $LiMn_2O_4$ are limited in satisfying the demands of high energy density.[7, 8] These difficulties have generated considerable worldwide efforts to seek new cathode materials with higher energy density.

In this regard, lithium- and manganese- enriched oxides, which are the solid solutions between layered $Li[Li_{1/3}Mn_{2/3}]O_2$ (commonly designated as Li_2MnO_3) and $LiMO_2$ (M = Ni, Co, Mn) have been found recently to be of high fundamental and technological interest as some of them exhibit much higher capacity with lower cost and better safety than the currently used $LiCoO_2$ cathode. For example, these layered lithium-rich compositions such as $Li_{1.2}Ni_{0.2}Mn_{0.6}O_2$ and $Li_{1.2}Ni_{0.13}Co_{0.13}Mn_{0.54}O_2$ can deliver reversible discharge capacities as high as 250 mAh g^{-1} when cycled between 2-4.8 V (vs. Li^+/Li^0).[9, 10] The high capacities of these solid solutions have been attributed to the reversible oxygen redox from the lattice during the first charge.[11, 12]

Despite its high capacities, this material has several challenges (voltage fading, structural instability, sluggish kinetics, cathode electrolyte interphase instability, etc.) that must be overcome in order to reach commercialization. In order to improve the initial Coulombic efficiency, the surface coating with oxides, fluoride, and other resistant materials have been conducted.[13, 14] Various doping elements and surface modification methods have been adopted to improve cycle stability, and rate performance of these lithium excess materials.[15, 16] However, all of them cannot absolutely prevent internal phase transformation of the materials, which results in deterioration of the electrochemical performance. Our work demonstrates the critical needs for advanced diagnosis and characterization. It is through the in-depth understanding of these high voltage cathode materials at atomistic and molecular level and their dynamic changes during the operation of batteries; strategies can be successfully formulated to optimize this class of cathode materials.

Another way to further reduce global warming is to consider alternate energy storage systems other than LIBs. Compared with lithium ion battery system, magnesium ion battery has several superior characteristics that rank it as one of the most promising alternatives for high energy-density batteries. In view of great nature abundance, high specific volumetric capacity, stable enough in ambient atmosphere, environmental friendliness and low price, there has been an ever-growing interest in rechargeable Mg batteries in recent years.[17-19] It is worthy note that magnesium metal can be directly used as anode in full cell without any security problems related to the metallic dendrite formation so as to obtain an even higher energy density battery. One major threshold factor to realize high energy density Mg-ion battery is to develop a novel type of cathode with an extremely large theoretical capacity. Therefore, my PhD research also focuses on the investigation and development of cathode for MIBs.

My PhD thesis consists of eight chapters, including this motivation (**Chapter 1**). **Chapter 2** provides a general introduction to the function mechanism of the LIBs. It focuses on transition metal oxide cathode materials for both LIBs and MIBs. **Chapter 3** briefly introduces advanced characterization tools that I used in my research including operando SXRD, TXM, STEM-EELS, and DFT based first principles calculation. In **Chapter 4**, we clearly demonstrate that meso-structure design of Li-rich layered oxides play a key role in optimizing this class of cathode materials. In **Chapter 5**, we mainly focus on the comprehensive design and control of oxygen activity in transition-metal-oxide systems for next-generation Li-ion batteries. **Chapter 6** discusses the influence of defects generation on the structure metastability and voltage decay in lithium-rich layered oxide cathode. **Chapter 7** focuses on the feasibility of using anatase-phase TiO_2 as an electrode material for MIBs by combining electrochemical, microscopic, and spectroscopic analyses. **Chapter 8** summarizes the overall work and ideas for future research.

Chapter 2. Introduction

2.1. Introduction of Lithium-ion Batteries (LIBs)

LIBs research began in 1950s, and became practical in 70s. Lithium metal was used in the early version of LIBs. However, the formation of dendrite lithium in the process of the battery charge and discharge not only caused irreversible capacity, but also lead to internal short circuit and explosion, resulting in serious safety problems.[20] In order to improve the reliability and safety of LIBs, John Goodenough and Koichi Mizushima first demonstrated a rechargeable lithium cell with voltage in the 4 V range using lithium cobalt oxide ($LiCoO_2$) as the cathode in 1980.[21] This innovation provided a stable cathode which acts as a donor of lithium ions, which means that it can be used with a negative electrode material other than lithium metal. Subsequently, in 1990, Nagoura et al. from Sony Corp developed a lithium ion secondary battery with petroleum coke as anode and lithium cobalt oxide as cathode. Since then, LIBs have developed rapidly and occupied a large share in the portable device market, and is striding forward to the field of large power equipment and electric vehicle power supply.

The commercial lithium ion battery has different components including lithium composite metal oxide as cathode, layered graphite on copper plate as anode, ethylene carbonate electrolyte with $LiPF_6$ as salt. Polyolefin resins are commonly used as separator materials, such as polyethylene (PE), polypropylene (PP) or their composite membranes. The actual battery should also include positive and negative pole set current collector, insulation piece, safety valve, etc. The electrochemical reaction of the lithium ion secondary battery with $LiCoO_2$/C as the electrode material is as follows:

$$\text{Cathode: } LiCoO_2 \leftrightarrow Li_xCoO_2 + xLi^+ + xe^- \quad (2.1)$$

$$\text{Anode: } 6C + xLi^+ + xe^- \leftrightarrow Li_xC_6 \quad (2.2)$$
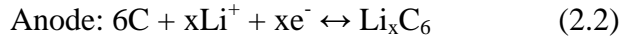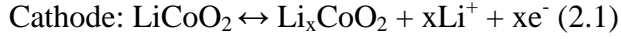
The lithium ion secondary battery is based on the lithium ion chemical potential difference in the anode and cathode to achieve rapid charge and discharge process. When charging, Li ion deintercalates from $LiCoO_2$) and passes through the Li-ion conductive electrolyte and intercalates to the layered graphite. And the external circuit is supplied with the electronic compensation from the anode, to maintain the charge balance; in the discharging process, the reverse mechanism occurs (see Figure 2.1). In the case of ideal charge/discharge cycle, the deintercalation and intercalation of Li ion in the material will not result in the structural change of cathode and anode materials. Therefore, the lithium ion battery reaction is an ideal reversible reaction. In addition, suitable electrolyte selection for a pair of electrodes in LIBs is another important aspect. For a stable cell, chemical potential of anode must be lower in energy than the LUMO of the electrolyte and on the other hand chemical potential of the cathode should be higher in energy than the HOMO of the electrolyte to prevent the reduction and oxidation of the electrolyte.[22]
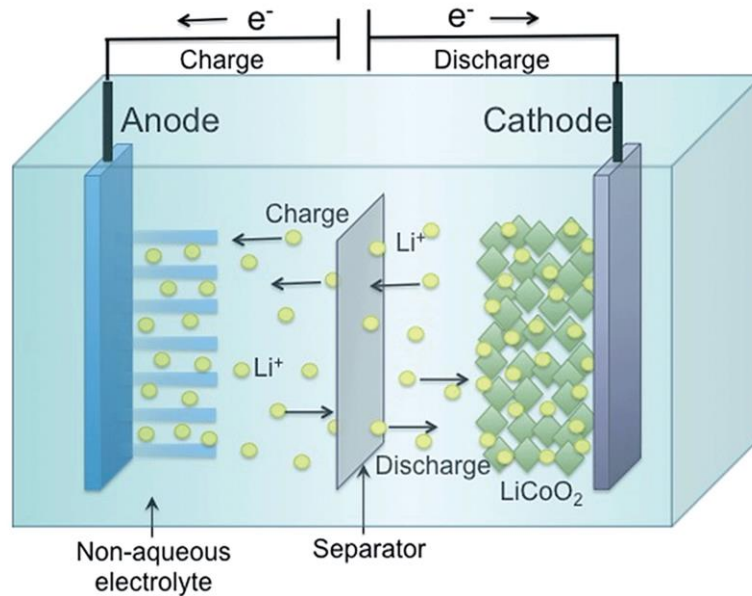
Figure 2.1. Schematic of the working mechanism of LIBs.[22]

2.2. Cathode Materials for LIBs

As mentioned in the Motivation Section, the electrode material is the core of the lithium-ion battery, and the electrochemical performance of battery mainly depends on the electrode material. Cost of cathode material is as high as 40% of the whole battery, so the research on the structure and properties of cathode material is of great significance for lithium ion battery. Generally, the selection of cathode materials for LIBs has the following guide lines:

(1) high standard electrode potential;

(2) large reversible lithiation capacity;

(3) high stability towards the electrolyte;

(4) high electronic conductivity;

(5) low cost and environmentally friendly.

In the past four decades, progress has been made steadily to improve the energy density of the various cathode materials. In the 1970s, Whittingham demonstrated that layered TiS_2 could

be a cathode material for a lithium rechargeable battery, though the voltage versus a lithium metal anode was only about 2.2 V.[20] In 1980, Goodenough and Mizushima showed that an open-circuit voltage versus lithium of 4.0 V could be achieved using $LiCoO_2$ as the cathode material.[21] Although it was not until 1991, that the material and its derivatives $Li(Co, Ni)O_2$ were used in commercial lithium ion batteries enabling the wireless revolution.[1] It was soon realized that only half of the lithium could be extracted from $LiCoO_2$ before a major phase transition occurred, leading to a significant capacity loss and in the extreme case oxygen loss.[23-25] Many alternatives of cathodes were explored, including LiM_2O_4, $LiMPO_4$, and $LiMnO_2$. Most of these materials consist of close-packed planes of oxygen ions with transition metal ions occupying octahedral sites formed by oxygen ions.

2.2.1. Spinel Compounds LiM_2O_4

The structure of LiM_2O_4 spinel is shown in Figure 2.2. Spinel LiM_2O_4 belongs to cubic *Fd-3m* space group with lattice constant around 0.825 nm. In this structure, lithium occupies tetrahedral (8a) position, transition metal occupies the octahedral site (16d), and oxygen occupies the face centered cubic position (32e). Therefore the unit cell contains 56 atoms including 32 oxygen atoms, 16 metal atoms and 8 lithium atoms. The structure is based on a three-dimensional MO_2 host and the vacancies ensure the three dimensional Li diffusion pathways as indicated by the black arrows in Figure 2.2. The electrochemical reaction equation is as follows:

$$LiM_2O_4 \leftrightarrow Li_{1-x}M_2O_4 + xLi^+ + xe^- \qquad (2.3)$$

8
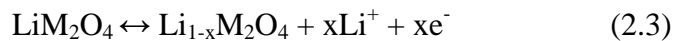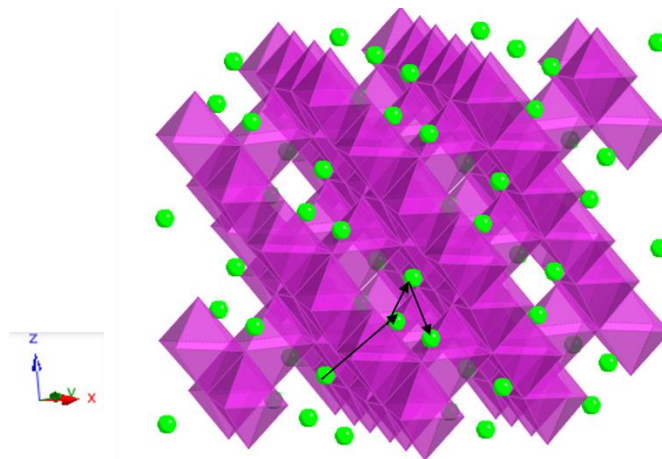
Figure 2.2. Crystal structure of spinel LiM_2O_4 (purple: transition metal ions; green: Li ions).

The spinel $LiMn_2O_4$ was proposed as the cathode of the lithium ion battery by Thackeray et al. in 1983.[26, 27] Its working voltage is around 4 V and theoretical capacity is 148 mAh g^{-1}. The actual discharge capacity is 110~120 mAh g^{-1} which is corresponding to 80% of lithium ion extraction from the structure. Additionally, $LiMn_2O_4$ also has the advantages of rich manganese source, low cost, environmental friendliness and good safety performance. However, the material was found to encounter sever capacity fading problem. Two reasons have been considered as the main sources for the capacity fading:

(1)   Jahn-Teller effect occurs in the process of deep charge and discharge of spinel material, resulting in lattice structure distortion (the ratio of lattice constant c/a increases by 16%), which leads to larger volume change and collapse of structure.[28] The tetragonal phase is formed on the surface of spinel structure, which is incompatible with the internal crystal system, resulting in the loss of capacity.[29]

(2)   The dissolution of Mn^{2+} into the electrolyte. The existence of a trace amount of water in electrolyte triggers the reaction of $LiPF_6$ salt to produce

9

hydrofluoric acid, leading to the disproportionation of Mn^{3+} to generate Mn^{2+}.[30]

2.2.2. Olivine Compounds LiMPO$_4$

Lithium iron phosphate has been postulated as a positive electrode material for secondary electrochemical cells. This olivine-structure material (see Figure 2.3) belongs to orthorhombic system with *Pmna* space group. The LiO_6 octahedra are edge-shared while the FeO_6 octahedra are corner-shared. P is located at the central position of oxygen tetrahedron, forming PO_4 tetrahedron. In this framework, iron atoms hinder the intercalation and deintercalation of lithium ions, so the ion diffusion rate of this material is relatively low at room temperature.
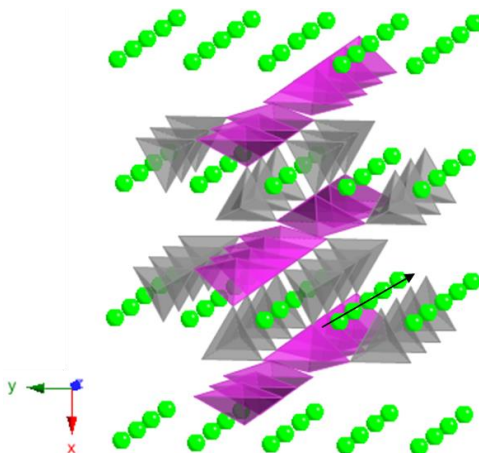
Figure 2.3. Crystal structure of olivine LiMPO$_4$ (purple: transition metal ions; grey: phosphorus ions; green: Li ions).

LiFePO$_4$ has a theoretical capacity of 170 mAh g^{-1} and Li-extraction voltage of 3.5V (vs. Li/Li$^+$).[31] The absence of cobalt results in lower cost and environmental harm than the more ubiquitous LiCoO$_2$. With this high theoretical electrochemical performance and low cost, this material has potential applications in consumer and industrial settings. However, LiFePO$_4$ has low electronic conductivity at room temperature (~10^{-9} S cm^{-1}) and the Li diffusion pathways can

be blocked during cycling.[32, 33] Proposed solutions to these issues include the preparation of LiFePO$_4$/carbon composites and decreasing the size of LiFePO$_4$ particles.[34] The preparation of nano-particulate LiFePO$_4$ has been achieved under a variety of synthetic procedures, notably under solvothermal, hydrothermal, sol-gel, and polyol processes.[33] However, the intrinsic low conductivity of this series of materials is still the key problem because the size reduction and carbon coating increases the synthesis cost drastically.

2.2.3. Layered Compounds LiMO$_2$

Many alternatives of LiMO$_2$ (M is 3+ cation to replace Co which is expensive and toxic) were explored, including LiNiO$_2$ and LiMnO$_2$.[35-38] Similar to LiCoO$_2$, LiNiO$_2$ is α-NaFeO$_2$ layered structure, in which the oxygen anions (see Figure 2.4) form a close-packed fcc lattice with cations located in the 6- coordinated octahedral crystal site. The NiO$_2$ slabs and Li layers are stacked alternatively. LiNiO$_2$ can be charged and discharged in the range of 4.3~2.5 V, and the actual specific capacity is higher than that of LiCoO$_2$, which can reach 210 mAh g^{-1}. However, all these layered oxides tend to become disordered or transform into a different structure on partial removal of lithium. Transporting the M ions to the lithium layer is thermodynamically driven, causing irreversible phase changes in the materials.
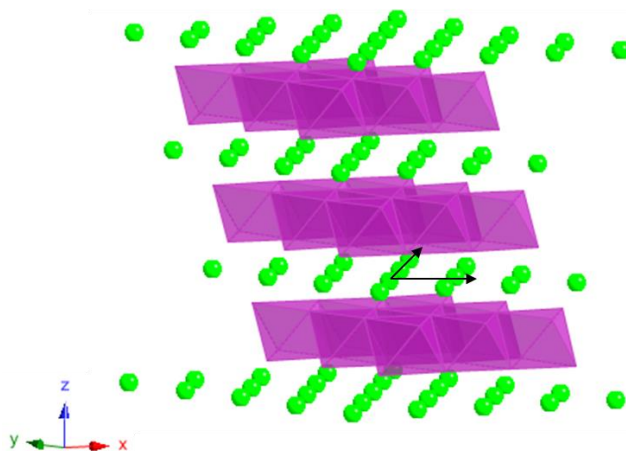
Figure 2.4. Crystal structure of layered $LiMO_2$ (purple: transition metal ions; green: Li ions).

Not much progress had been achieved in improving energy density of layered compounds until 2001 when Ohzuku and Makimura synthesized $LiMn_{0.5}Ni_{0.5}O_2$ and $LiMn_{1/3}Co_{1/3}Ni_{1/3}O_2$, delivering 20% more energy density than that of $LiCoO_2$.[39, 40] The key materials design concept is that Ni^{2+} is stable in the presence of Mn^{4+} and Ni^{2+}/Ni^{3+} and Ni^{3+}/Ni^{4+} redox couples are both pinned at the top of the oxygen $2p^6$ band, meaning there will be no voltage step while transferring two electrons from Ni^{2+} to Ni^{4+}. This illustrates the recent trend toward multicomponent transition metal layered oxides, which creates a large number of possible compositional choices.

As shown in Figure 2.5, chemical substitution of Co^{3+} with Ni^{2+}, Mn^{4+}, and Al^{3+} increases the practical capacity limit from 140 mAh g^{-1} to around 200 mAh g^{-1}. Further substitution of the transition metals by Li has been reported as $xLi_2MnO_3-(1-x)Li(Ni, Mn)O_2$ (Li-rich material) by Thackeray's group and Dahn's group.[41-43] This family of materials has

shown superior energy density (see Figure 2.5) almost two times that of LiCoO$_2$, which will be covered in detail in the following introduction.
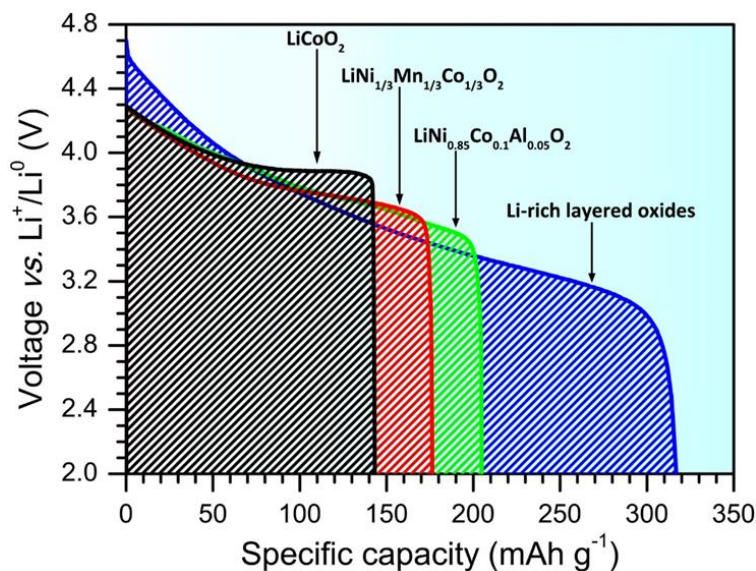
Figure 2.5. Discharge capacity in different layered oxides.

2.3. Lithium-rich Layered Oxide Cathode Materials for LIBs

Throughout history, Li-ion battery technology has relied on cationic redox reaction as the main source of energy storage.[44, 45] This is no longer true with the recent discovery of anionic (oxygen) redox in Li-rich layered oxides, which enables high reversible capacity over 300 mAh g^{-1} in these materials at room temperature. Unfortunately, there are many issues still unclear, and numerous scientific challenges (poor rate capability, and voltage degradation during cycling) of these materials that must be overcome to realize their utilization in commercial lithium-ion batteries. Our previous research experience reveals these issues can not be fully resolved without basic understanding on structure evolution and anionic electrochemical activity in these high-capacity oxides.

2.3.1. Materials Structure and Reaction Mechanism

The structure of $xLi_2MnO_3-(1-x)Li(Ni, Mn)O_2$ differs significantly from that of classical layered oxides such as $LiCoO_2$, because additional Li is present in the transition metal (TM) layer inducing cation ordering in the TM layers and symmetry breaking.[46, 47] The lithium present in the TM layer leads to formation of a partially ordered honeycomb structure as seen in the end member Li_2MnO_3, resulting in superlattice peaks between 20° and 26° 2θ (Cu Kα) in X-ray diffraction (XRD) patterns.[48, 49] Therefore, Li-rich layered oxide is considered either as a solid solution or as a nanocomposite of layered Li_2MnO_3 and $Li(TM)O_2$ (TM = Ni, Co, Mn) with excess lithium ions in the transition metal layer. The discrepancies in Li-rich layered structure determination can originate from the sample variation caused by different synthesis conditions and chemical compositions.

Upon lithium extraction, the nickel is oxidized to Ni^{4+} up to 4.4 V. Lithium may continue to be extracted from these materials despite the fact that all the manganese and nickel ions are in their fully charged (+4) oxidation state, which is associated with a plateau region at 4.5 V.[50] High operating voltage (over 4.6 V vs Li^+/Li^0), beyond the electrochemical stability window of most organic electrolytes, is usually required to activate oxygen redox in these materials. The electrolyte oxidation results in the gradual accumulation of a thick solid electrolyte interphase (SEI) layer on the electrode surface, which causes rapid increase of cell impedance. Furthermore, a considerable amount of lithium ions removal together with oxygen loss from the lattice facilitates cation migration and structural rearrangement. These surface and bulk reactions finally lead to continuous capacity fading and voltage decay during electrochemical cycling, which largely limits the practical deployment of this class of materials in industry.

Over the past decade, most of the research has been dedicated to explain precisely how the cation migrations occur as a function of the charge/discharge state and the impacts of such dynamic phenomena on electrochemistry. For this purpose, an effective characterization toolset has been established to probe cation migration and rearrangement at both long-range and local length scales, including operando XRD, operando X-ray adsorption spectroscopy (XAS), first principles calculations, and high angle annular dark field (HAADF) scanning transmission electron microscopy (STEM). It is not until recently that scientists have focused on the electrochemical activities of oxygen anions in these lithium rich layered oxides.

2.3.2. Anionic Electrochemical Activities

Although there are some discrepancies concerning the structural complexity of Li-rich layered oxide materials, it is generally acknowledged that anionic activity is involved in the electrochemistry besides the cationic redox process, by which extra capacity is obtained. When the material is charged over the transition metal redox reaction region (above 4.4 V for most of the Li-rich materials), the reversible oxygen redox process ($2O^{2-} \rightarrow O_2^{n-}$, where n = 1, 2, or 3) dominates in the bulk to compensate charge changes during delithiation.[51] Oxygen gas has also been detected which results in a large irreversible capacity. At the same time, the lattice oxygen removal in terms of O_2 gas or LiO_2, Li_2O_2, or Li_2O solids results in oxygen vacancy formation on the surface and subsurface (5−10 nm range from the surface).[51]

Reversible oxygen redox in the bulk of Li-rich material has been investigated from different aspects. Ceder and coworkers apply ab initio calculations to demonstrate that the specific Li−O−Li configurations, which are derived from the excess Li in the transition metal layer, lead to the electrochemically active oxygen states in Li-rich material.[52] As shown in Figure 2.6b, under these specific configurations, two types of O 2p orbitals are created: (1) hybridized

with TM orbitals to form the same hybridized states as in the classical layered oxides and (2) an additional unhybridized orbital in between hybridized O bonding states and the antibonding TM states, making oxygen oxidation and TM oxidation compete with each other to contribute to the extra capacity. O−O bonding (peroxo-like species) resulted from oxygen oxidation tends to form on the condition that TM−O hybridization is not strongly directional. Combining different advanced characterization tools, Bruce and co-workers prove that, compared with O−(Ni^{4+}/Co^{4+}) interactions, O−(Mn^{4+}/Li^{+}) interactions possess relatively more ionic and localized O 2p orbitals.[53] Electron transfer can occur from these O 2p orbitals to make the charge be compensated for during excess Li+ removal, leaving localized electron holes on these less covalent orbitals.

On the other hand, Tarascon and co-workers observed O−O bonding formation by the oxidation of O^{2-} to an $(O_2)^{n-}$ species through HAADF-STEM in 4d and 5d TM oxides $Li_2Ru_{1-x}Sn_xO_3$ and $Li_2Ir_{1-x}Sn_xO_3$.[54, 55] A pronounced M(nd)−O(np) metal−ligand hybridization mechanism is proposed for 4d and 5d TM oxides.[56] The ligand orbitals are highly delocalized so they form covalent bonds with the d-metals through M(d)−$O_2(\sigma)$ interactions (see Figure 2.6c). The $(O_2)^{n-}$ species will be then stabilized through their interactions over Ru−O as well as O− O σ-type bonds, therefore forming O−O dimers. Moreover, they investigated the formation of $(O_2)^{n-}$ species and their recombination into O_2 gas in the Li-rich Li_2TMO_3 family.[57] Although the exact mechanism is still under exploration, a correlation between the oxidation voltage and possibility of $(O_2)^{n-}$ recombination into O_2 is proposed that the recombination rate is enhanced at higher voltage than that at relatively lower voltage.
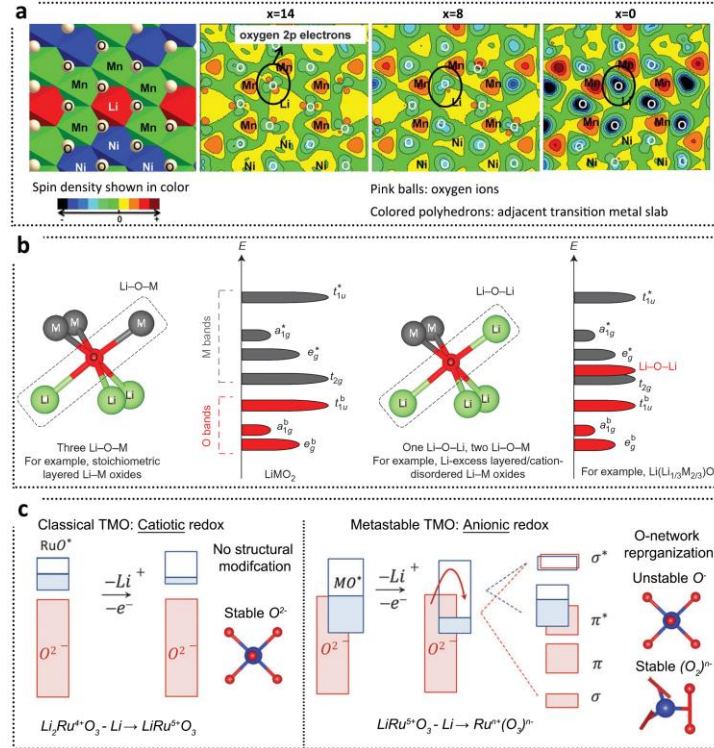
Figure 2.6. a. Sketch of a partial oxygen layer in $Li_{x/14}Ni_{1/4}Mn_{7/12}O_2$ and its calculated spin density at different x values. b. Structural and chemical origin of the preferred oxygen oxidation along the Li−O−Li configuration. c. Cationic vs anionic redox: qualitative band structure of a structurally stable and metastable transition metal oxide.[52, 56, 60]

2.3.3. Defects Formation and Correlation with Performance Issues

Meng and co-workers systematically studied the effect of oxygen vacancies on structural transformation of Li-rich material during electrochemical cycling.[58, 59] At lower lithium concentration (see Figure 2.6a), the shape of oxygen 2p electron clouds begins to distort, suggesting a potential change of oxygen valence that may promote oxygen vacancies formation.[60] As confirmed by scanning transmission electron microscopy/electron energy loss spectroscopy (STEM/EELS) experiments, oxygen vacancies mostly form near the material surfaces and subsurfaces of 5−6 atomic layers.[58] A large fraction of the TM ions in these regions therefore are in undercoordinated octahedral sites which are not stable and spontaneously

17

migrate to the fully coordinated octahedral sites nearby in the Li layer. On the other hand, the Li in the TM layer migrates to the shared tetrahedral site in the opposite site, forming a Li−Li dumbbell. The above two migrations cause the spinel-like phase to create on the surface.[60] We would like to point out that this surface phase transformation is different from the formation of the rock-salt phase in Ni-rich classical layered oxides such as $LiNi_{0.85}Co_{0.1}Al_{0.05}O_2$. And the surface phase transformation from layered to spinel-like is irreversible upon the following cycles, accompanying the increased percentage of microstrain within the particles, and finally results in voltage degradation and capacity fading during extended cycles.

All of the above investigations unequivocally demonstrate that oxygen participates in the electrochemical activity of Li-rich layered cathode material at high voltage through either an irreversible oxidation with O_2 gas release and/or a reversible redox process with either O-holes or O−O dimer formation. O−O bonding tends to form in 4d and 5d TM oxides, while localized electron holes on oxygen can exist in 3d TM systems. Different mechanisms have been proposed based on ab initio calculations to study the role of M(4d) vs M(3d) on their electrochemical behavior: (1) the holes in O 2p orbital are localized for 3d TM such as Mn, because partially filled d shells creates strong directional TM−O bonds which prevent the neighboring oxygen from rotating; (2) more ionic interactions between O−(Mn^{4+}/Li^+) place the localized O-holes near the top of the oxygen valence band; and (3) no empty MO*-orbitals in the Li_2MnO_3 structure close enough to the top of the O-band leads to a partial decoordination of the $(O_2)^{n-}$ species and O-holes localization. More in situ/operando microscopy/spectroscopy characterizations at various length and time scales are still in need focusing on O−O bonding formation/O-holes quantification to fully understand oxygen anion electrochemical activities as well as the role of transition metal species on oxygen redox behavior. It is still unclear how the

oxygen participation in electrochemical processes will impact the safety and long-term cyclability of the cathodes.

2.3.4. Design Considerations and Guidelines

The knowledge gained from the previous studies on oxygen electrochemical activity guides us to surpass the limits of the transition metal redox in conventional intercalation electrodes for next generation lithium-ion batteries. In the classical layered oxides such as $LiCoO_2$, lattice oxygen mostly acts as a pillar (host) to stabilize the structure without contributing much too any extra capacity. When extra lithium is introduced to the transition metal layer, both cationic and anionic redox participate in the electrochemical reaction, which may significantly boost overall energy density. Following this trend, Li_2O/MO nanocompositions are also proposed, in which lattice oxygen redox is considered as the equally dominating redox center.[61] By carefully examining the local structural changes surrounding the oxygen of these benchmark materials, Li/O ratio is one of the key factors to determine the utilization extent of oxygen electrochemistry activity:

(1) There is the Li/O ratio between 0 and 0.5 for classical layered and spinel oxides with Li−O−M configuration, where lattice oxygen does not involve in the electrochemical reaction.

(2) Next is the Li/O ratio between 0.5 and 1.0 for Li-rich layered oxides with Li−O−Li (M) configuration, where lattice oxygen not only stabilizes the structure but also acts as the redox center which brings in high reversible capacity over 300 mAh g^{-1}.

(3) Li/O ratio beyond 1.0 for nanocomposites between Li_2O and metal oxides (MO) with Li−O−Li configuration, where the majority of the reversible capacity is contributed

by the oxygen redox, enabling charge/discharge between condensed Li_2O, Li_2O_2, and LiO_2 without any O_2 gas.

The long-term performance of Li-rich layered oxide is also largely at the mercy of its synthesis route and conditions. Several different synthesis routes have been applied to obtain differing morphologies and sizes for this material. While there has been an exploration of sol–gel and hydrothermal synthesis methods, the most adopted has been the co-precipitation method. The oxygen activities can be further tailored by morphology engineering (e.g., nanosizing and shape controlling), compositional optimization (e.g., transition metal species and Li/O ratio), and surface modification.

2.4. Introduction of Magnesium-ion Batteries (MIBs)

While Li-ion battery technology has vastly improved upon its induction, significant problems remain intrinsically with this system. This includes the relative scarcity of Li compared to other common metals as well as the formation of dendritic Li when Li metal is used as a negative electrode In order to circumvent these issues, there is increasing interest in the development of alternative technologies based on sodium and magnesium. The use of magnesium in electrochemical cells is of particular interest to industry. In comparison to lithium, magnesium is considerably less expensive.[62] In addition, Mg has several advantages over comparable Li systems, such as nearly double volumetric capacity. This is due to potentially up to two moles of electrons transferred from the dicationic Mg^{2+} compared to one for Li^+ and Na^+. A higher volumetric energy density is especially attractive for use in cases where volumes are restrictive such as portable electronic devices such as mobile phones or laptop computers. An increase in volumetric energy density would permit for more energy storage in smaller volumes.

Finally, magnesium metal is safe enough to be used as an anode as no dendritic Mg forms upon deposition, unlike that of lithium (see Figure 2.7).
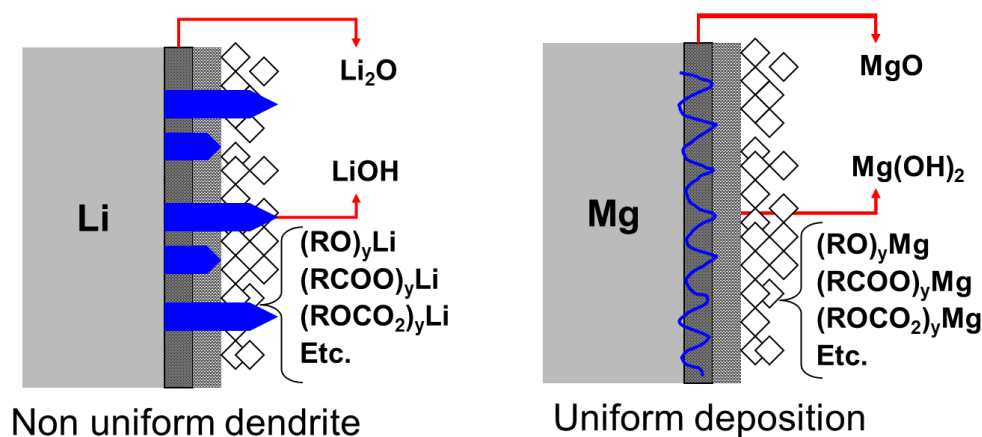
Figure 2.7. Schematic of the metal deposition comparison between Li and Mg.

2.4.1. Dendrite-free Deposition of Magnesium Metal

Initial studies probing the mechanism of Mg deposition/ dissolution were performed on Au surfaces using $Bu_2Mg/AlEtCl_2$/tetraglyme as electrolyte utilizing *in situ* atomic force microscopy (AFM).[63] The use of *in situ* AFM at various polarization potentials showed that the surface roughness of the gold working electrode is directly correlated the state of charge of the cell. That is, during the first polarization from the open circuit voltage (OCV), the Au surface became intensely rough with deposited magnesium. After dissolving the Mg and re-depositing on the Mg counter electrode, the Au electrode surface returns to its near pristine state.

Subsequent experiments applied techniques such as *in situ* electrochemical quartz crystal microbalance (EQCM) and FTIR to probe surface changes during magnesium deposition.

During initial plating, the mass change determined by EQCM indicated that upon cathodic polarization to 0.5 V (vs. Mg/Mg^{2+}), the mass per mole of electrons (m.p.e.) calculated is correlated to a value greater than 12 g mol^{-1} (molecular mass of Mg). This however, reduces to ca. 12 g mol^{-1} after moderate deposition. The researchers proposed that the high m.p.e. value is due to an adsorption process wherein either an RMg or RMg^+ species is adsorbed on the surface of the electrode. Additional evidence supporting the presence of adsorbed species was obtained using FTIR during Mg deposition using 1 M CH_3MgCl in THF as electrolyte. The spectrum shows that a new absorbance band at 525 cm^{-1} appears during the plating process. This stretching frequency is purported to be that of an Mg-C bond. Further experiments using BzMgCl/THF (Bz = benzyl) as electrolyte due to the plethora of aryl stretching frequencies on the organic moiety compared to the methyl Grignard. The FTIR spectrum showed peak growth and shifts in the aryl C=C (ν = ~1600 cm^{-1}) and C-H (ν = ~3060 cm^{-1}) regions during Mg deposition from OCV to -0.5 V (vs. Mg).

These initial reports provided an excellent foundation in the attempt to determine the mechanism of magnesium electrodeposition. However, no study was performed that probed different magnesium deposition morphologies until 2013. A recent report by the Yagi group detailed the effect of water contamination in a similar electrolyte (EtMgCl/ $AlCl_3$/THF) and it was shown that a small spike (67 ppm) in water results in markedly different deposition morphology and poor electrochemical performance (81% cycling efficiency).[64] As opposed to obtaining the plate-like morphology when using APC electrolyte, cauliflower-type morphology was observed. While no *in situ* experiments were performed using this contaminated electrolyte, this study shows how small system perturbations can result in vastly different morphologies.

The preliminary experiments performed by Aurbach and coworkers made great use of *in situ/ in operando* techniques. However, there was obvious variation between experiments, notably in differences in electrolytes used and absence of long cycle data concerning electrolyte stability and if any morphological changes occurred were not described. In addition, no further studies were performed using more advanced electrolytes, such as $PhMgCl/AlCl_3$ in THF or the recently described simple salt electrolyte 0.4 M $Mg(TFSI)_2$ in glyme/diglyme (1:1 v/v).[65]

2.4.2. Cathode Materials for MIBs

One important factor to realize high energy density Mg-ion battery is to develop a novel type of cathode with an extremely large theoretical capacity. Nowadays, various cathode materials such as Chevrel phase $M_xMo_6T_8$ (M = metal, T = S, Se), and transition metal oxides (V_2O_5, RuO_2, MnO_2, Co_3O_4), have been successfully used to achieve the reversible insertion and extraction of Mg^+.[66-70] Among these choices of cathode, MoS_2 as a common used layered transition metal sulfide and $Mg_xM_ySiO_4$ (M = Mn, Fe, Co, x + y = 1) similar to the most attractive Li-ion battery cathode material $LiFePO_4$, are the most promising ones due to their high theoretical capacity and feasible synthesis.

In addition, anatase TiO_2, as a typical lithium intercalation electrode, has attracted considerable interest during the past decade.[71, 72] The use of TiO_2 (anatase) as an electrode material in lithium ion batteries and electrochromic devices is based on its ability to accommodate charge in the form of small foreign ions, such as Li^+ and H^+ in an intercalation process. Magnesium ions which are supposed to be the same size as Li ions have the chance to diffuse in and out of anatase TiO_2 at room temperature.

2.4.3. Challenges of Development for MIBs

Despite these attractive attributes of Mg batteries, there are still several obstacles that thwart the development and application of the whole electrochemical system. One major obstacle that prohibits Mg batteries from practical use is the narrow voltage range of the anodically stable electrolyte. Most conventional electrolyte may not be applicable for Mg-ion batteries due to the high polarizing ability of the divalent Mg^{2+} cation. In 2000, It was Aurbach et al that first discovered the reversible deposition and dissolution of magnesium in 0.25 M $Mg(AlCl_2EtBu)_2$/THF electrolyte, a Grignard reagent, with excellent columbic efficiency (~ 100%).[73] Although this electrolyte is limited to up to 2 V operation voltage (vs. Mg), it is still the most stable one and widely used in the research of magnesium ion battery. However, to attain a specific higher energy density of Mg-ion batteries, researchers have to concentrate on the development of electrolyte solutions' anodic stability (> 3 V class).

Unlike the more established and understood field of lithium batteries, magnesium electrochemistry is relatively new. Further studies are required to elucidate the mechanism of solid state diffusion of Mg^{2+} ions that is vastly different than that of Li^+ ions. Understanding such mechanism and the phase stability during the electrochemical process is important for the development and optimization of magnesium batteries.

This chapter in part, is a reprint of the material "Understanding and Controlling Anionic Electrochemical Activity in High-Capacity Oxides for Next Generation Li-Ion Batteries" as it appears in the Chemistry of Materials, Qiu, B.; Zhang, M.; Xia, Y.; Liu, Z.; Meng, Y. S., 2017, 29, 908. The dissertation author was the co-primary investigator and co-first author of this paper.

Chapter 3. Advanced Characterization Tools

3.1. Operando Synchrotron X-ray Diffraction (SXRD) for Microstrain Analysis

Lab XRD source for in situ test requires almost one hour to collect data with relatively high quality for refinement. So that it can not be used to monitor fast structure change during lithium interaction/deintercalation under high current density. Additionally, lab diffractometer has a Cu Kα radiation source (lambda=1.54Å) with a maximum resolution of 0.03° 2Θ. Accurate refinement using a laboratory diffractometer source is therefore not possible. Use of the synchrotron X-ray beamline will allow us obtain diffraction patterns with higher resolution and sensitivity for quantitatively analyzing the structural changes for the cathode sample upon cycling.

High-energy synchrotron X-ray with a beam size of 0.2mm×0.2mm was selected for this work to obtain 2D diffraction patterns in the transmission geometry. The diffraction data was collected with a large area detector, ensuring considerable diffraction intensity in a very short data collection time. With these advantages, the beamline will allow for in situ collection of higher resolution, energy, sensitivity and more accurate (no texture) XRD patterns upon cycling than on the laboratory diffractometer. More detailed information related to the structure change and evolution for the cathode sample will be explored in the following chapters.

The miscrostrain was analyzed by examining line broadening observed in the synchrotron SXRD patterns, which were collected at the Advanced Photon Source at Argonne National Laboratory. The data for LRLO was measured *in situ* with temperature control. Williamson−Hall analysis of all peaks that exhibit the best linear fitting was carried out for a quantification of microstrain changes during initial charging process.[74] The instrumental broadening was corrected based on the standard sample CeO_2 using the following equation:

$$FW(S)^D = FWHM^D - FW(I)^D \qquad \text{(eq 3.1)}$$

where *FWHM* is measured full width at half maximum of each peak; *FW*(s) and *FW*(I) are the calculated full-widths for the sample and instrument, respectively; D is the deconvolution parameter which is set to be 1.5 for all the analysis. The sample broadening is ascribed to particle size and microstrain based on the Williamson–Hall method by the following equation:

$$FW(S) \times \cos(\theta) = \frac{K \times \lambda}{Size} + 4 \times Strain \times \sin(\theta) \qquad \text{(eq 3.2)}$$

where *K* is the crystallite shape factor and was assumed to be 0.9; θ is the diffraction angle; and λ is the x-ray wavelength of the source. The microstrain is extracted from the slope of the plot of *FW*(s) cos(θ) versus 4 sin(θ).

For the Li-rich layered oxide sample, the superstructure peak was analyzed in the data used for the Williamson-Hall analysis. The superstructure peak height was determined as the peak intensity after background subtraction and normalization.

3.2. Transmission X-ray Microscope (TXM)

Full-field TXM imaging has been used to elucidate the nano and micron scale structure of a variety of battery samples. A monochromatic beam is focused by a reflective capillary condenser onto the sample, which is mounted on translation and rotation stages to allow alignment and tomography (see Figure 3.1).[75] The x-ray photons not absorbed either are transmitted through the sample or scattered from the sample focused by the zone plate then form an image at the imaging plane. TXM can also be coupled with scanning probe microscopy using finely focused X-ray beams in both the soft X-ray and hard X-ray regions. Hard X-ray

fluorescence microprobe, or scanning transmission X-ray microscopy (STXM) is effective for trace element imaging.
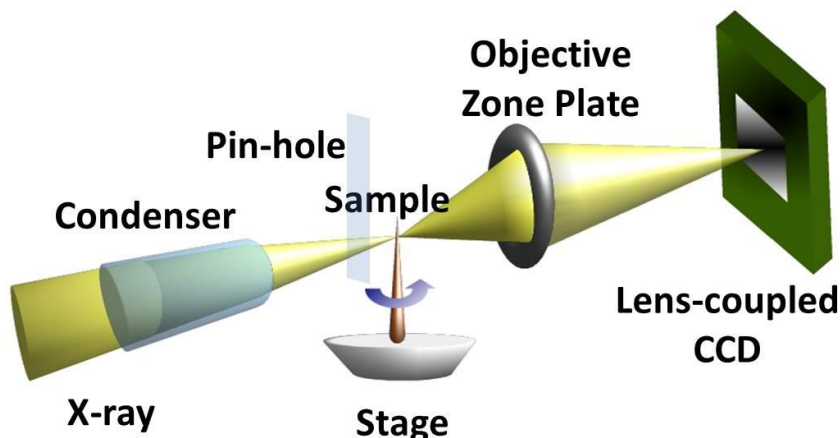
Figure 3.1. Schematic representation of TXM setup.[75]

TXM technique applied for battery material characterization has the following advantages:

(1) Non-destructive tomographic technique with in situ capability;

(2) Large reconstruction volume ~40*40*40 μm^3;

(3) High resolution: Sub-50 nm;

(4) Broad X-ray energy range (6 keV-12 keV) which is suitable for Ni, Mn, and Co K-edge absorption.

For my research, Nano-tomography measurements were carried out using the full-field TXM located at the beamline X8C, National Synchrotron Light Source, Brookhaven National Laboratory (BNL).[76] 3D reconstruction was performed by a standard filtered back projection reconstruction algorithm.[77] Tomography measurements with incident x-ray energies of 8400 eV were carried out in absorption contrast mode to obtain optimized image contrast for following

imaging segmentation. Each tomographic data set was collected with 1001 projections over the angular range of $180\,^\circ$ with a field of view of 40×40 μm^2 (the 2k $\times$ 2k CCD camera binned 2×2 pixels). Image reference correction, averaging, magnification correction, and auto alignment were performed prior to the tomographic reconstruction.[78]

3.3. Scanning Transmission Electron Microscopy (STEM)-Electron Energy Loss Spectroscopy (EELS)

A typical STEM is a conventional transmission electron microscope equipped with additional scanning coils which raster the focused electron beam into a narrow spot probe over the sample (see Figure 3.2). The small atomic scale probe is formed by focusing the electron beam with an energy of 300 keV through a series of condenser lenses. By taking advantage of the various scattering processes that occur between the incoming electrons and atoms in the material, STEM imaging with sensitivities to different structural and chemical information can be simultaneously applied using multiple annular detectors as shown in Figure 3.2.[79]

The high-angle annular dark-field (HAADF) detector configuration optimizes the electron detection, which provides an image exhibiting a contrast that is proportional to the atomic number of the atoms.[80] Conversely, an annular bright- field (ABF) detector provides an image contrast inversely proportional to atomic number, which is ideal for imaging light elements such as oxygen.[81] Exceptional care must be taken to exclude beam damage influence. Under a strong beam exposure, neurtal O atoms are created on the surface of layered oxides via Knotek−Feibelman mechanism and finally injected into the vacuum, leaving oxygen vacancies as well.
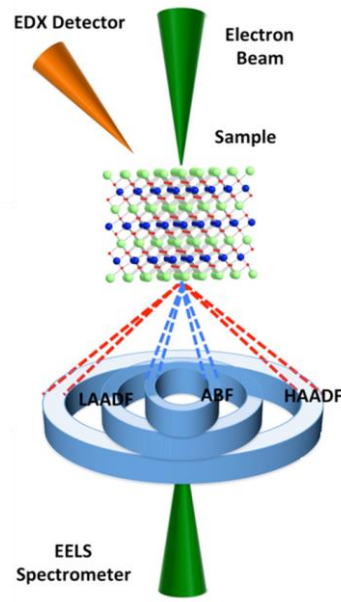
Figure 3.2. Schematic representation of the working mechanism of STEM-EELS.[79]

In addition to these imaging techniques, electron energy-loss spectroscopy (EELS) can be used to probe the electronic structures of materials along with elemental analysis.[82, 83] As the electron beam passes through the sample, some electrons in the beam lose energy via inelastic scattering interactions with electrons in the sample. In EELS, the energy lost by the electrons in the beam is measured using an electron spectrometer, allowing features such as plasmons, and elemental ionization edges to be identified. EELS has been introduced to recent research of transition metal layered oxides because of its unique capability to provide local electronic structure of oxygen atom, giving information about oxidation state, charge transfer, bonding, etc. The knowledge gained from the EELS studies on oxygen electrochemical activity will further guide us to surpass the limits, such as poor rate capability, and voltage degradation during cycling in transition metal layered oxides for next generation lithium-ion batteries.

Chapter 4. Modified Co-precipitation Synthesis of Meso-structure Controlled Li-rich Layered Oxides for Minimizing Voltage Degradation

4.1. Introduction

lithium- and manganese- enriched oxides, which are the solid solutions between layered Li[Li$_{1/3}$Mn$_{2/3}$]O$_2$ (commonly designated as Li$_2$MnO$_3$) and LiMO$_2$ (M = Ni, Co, Mn) have been extensively studied as cathode materials for rechargeable lithium ion batteries. These layered lithium-rich compositions such as Li$_{1.2}$Ni$_{0.2}$Mn$_{0.6}$O$_2$ and Li$_{1.2}$Ni$_{0.13}$Co$_{0.13}$Mn$_{0.54}$O$_2$ can deliver reversible discharge capacities as high as 280-300 mAh g^{-1} when cycled between 2-4.8 V (vs. Li$^+$/Li^0). However, there are many issues still unclear, and numerous scientific challenges of these materials that must be overcome to realize their utilization in commercial lithium-ion batteries. The first drawback is the irreversible voltage degradation process that limits cycle life. This degradation has been extensively investigated in the hopes of identifying methods to mitigate these losses.

As summarized in the previous review, different synthetic routes have a distinct effect upon the long term cycling performances of this material because of differences in morphology and particle size.[51] While there has been an exploration of solid-state and sol-gel synthesis methods, the most adopted has been the co-precipitation method.[84, 85] Co-precipitation synthesis, the most popular approach to synthesize Li-rich layered oxides, has many advantages: accurate stoichiometric proportions of transition metal precipitation; lower synthesis temperature compared with solid-state method; smaller primary particle size for better rate performance.[86-88] Depending on the addition of chelating agent, two different types of samples can be obtained: (1) samples with dispersive particles (without meso-structure control) synthesized by the co-precipitation method without chelating agent; (2) large spherical morphology secondary particles comprised of nanosized primary particles when ammonium hydroxide is introduced in the co-

precipitation method as a chelating agent.[89, 90] With the ammonium hydroxide chelating agent, the average secondary particle size grows up to 20 μm, which is beneficial for high tap density.[91] The large secondary particle size, however, may introduce several kinetic limitations during initial activation at first charging.[92] And it was observed recently cracking of the large size secondary particles occurred during the initial charging process and could not fully recover after the discharging process, leading to capacity and voltage degradation over extended cycling.[93] Chen et al. also found internal cracks within these large size particles even before any electrochemical cycling, which causes cycling degradation.[94] Based on the above considerations, it would be meaningful to achieve homogenous meso-structure controlled precursors of Li-rich layered oxides, with smaller secondary particle size and improved meso-structure robustness.

In the present study, we introduce a modified co-precipitation (MCP) method for preparing meso-structure controlled Li-rich layered oxide materials as high energy density cathodes for lithium ion batteries. This method is chelating agent free (without ammonia addition), which is environment-friendly. More importantly, the obtained material $Li_{1.2}Ni_{0.2}Mn_{0.6}O_2$ has a unique meso-structure: (1) spherical secondary particles with uniform dispersion; (2) the secondary particles are dense, and have a markedly reduced average diameter of approximately 3 μm; (3) these secondary spherical particles consist of primary particles with particle size approximately 150 nm. In this design, uniform distributed small secondary particles not only have decreased interface contact area with electrolyte, but also possess increased structure mechanical stability. Both features have positive effects on minimizing the voltage decay and capacity loss during long term cycling of lithium-rich layered oxides.

4.2. Experimental

4.2.1. Modified Co-precipitation Synthesis

As illustrated in Figure 4.1, an appropriate amount of Li_2CO_3 (the molar ratio of carbonate ions to transitional metal ions is 1:1) was dissolved in 60 mL deionized water, and then added dropwise into 10 ml of a mixed solution of $Ni(NO_3)_2$ and $Mn(NO_3)_2$ (Ni:Mn = 1:3 in molar ratio) under stirring. To prevent hydroxide precursor generation, pH value during co-precipitation process was carefully controlled. The resulting slurry was transferred to a 100 mL Teflonlined stainless steel autoclave, and then aged at 80°C for 12 h. The resulting $(Ni_{0.25}Mn_{0.75})CO_3$ precursor was washed several times with deionized water, and then dried in a vacuum oven at 80°C over night. Thereafter, the $(Ni_{0.25}Mn_{0.75})CO_3$ powder was mixed with a stoichiometric amount of Li_2CO_3, and was calcined at 500°C for 5 h in a 50 ml porcelain crucible, and then heated up to 900°C and kept at this temperature for 6 h followed by quenching in the air. Note that the heating rate was maintained at 5°C min^{-1}. Another sample with the same composition was also synthesized by a conventional co-precipitation (CCP) method without meso-structure control. This CCP method without ammonia addition was adopted as a control experiment to exclude the influence of ammonium hydroxide on the electrochemical performance. And the main difference between the two samples is meso-structure, which will be discussed in detail.
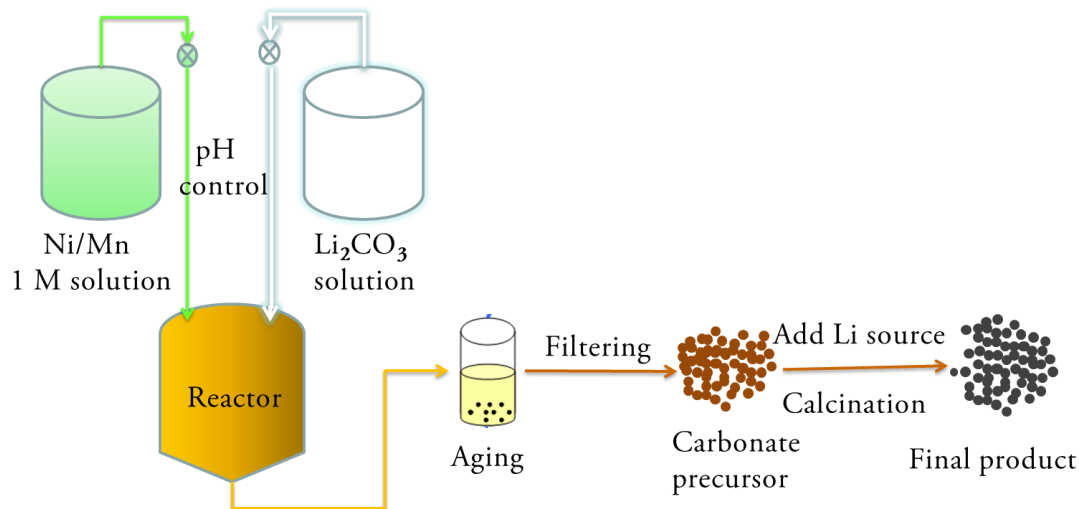
Figure 4.1. Schematic of the MCP synthesis process for meso-structure controlled Li-rich layered oxides.

4.2.2. Materials Characterizations

The crystal structure of materials was identified by X-ray diffraction (XRD), acquired using a Bruker D8 advance diffractometer with a Bragg−Brentano θ-2θ geometry and a Cu Kα source (λ = 1.54 Å). Rietveld refinement was performed using FullProf software. The particle morphology and size distribution of the synthesized powders were determined using an FEI XL30 ultrahigh-resolution scanning electron microscope (UHR SEM) system. All images were collected under an accelerating voltage of 10 kV. Nitrogen physisorption was used to determine surface areas by incorporating the Brunauer−Emmett−Teller (BET) method. ICP-OES was performed using a PerkinElmer 3700 optical emission plasma spectrometer.

4.2.3. Electrochemical Measurements

All electrochemical measurements were performed on CR2016-type coin cells with metallic lithium as the counter and reference anode. The cathode electrodes consisted of 80 wt. % active materials, 10 wt. % acetylene black, 10 wt. % polyvinylidence fluoride (PVDF) and

a little 1-methyl-2-pyrrolidone (NMP) solvent to form a slurry, and then the slurry was coated on an Al foil and dried in a vacuum oven at 80°C over night. 1 M $LiPF_6$ solution in a mixture of ethylene carbonate (EC)/dimethyl carbonate (DMC) (EC/DMC, volume ratio 3:7) was used as the electrolyte and Celgard C480 membrane as separator. Initial galvanstatic charge/discharge test was carried out at 0.05 C (1 C = 250 mAh g^{-1}) in the voltage range of 2.0-4.8 V. In the cyclic performance test, the cell was charged and discharged at 0.1 C or 1.0 C, respectively. Electrochemical impedance measurement was performed on the Solartron 1287 electrochemical interface. And the measurement was carried out in the frequency range of 0.01-100,000 Hz using a signal with an amplitude of 5 mV.

4.3. Results and Discussion

4.3.1. Crystal Structure and Morphology Characterization

The XRD pattern of the precursor powder synthesized by our MCP method is shown in Figure 4.2. All the diffraction lines of the precursor can be indexed to a hexagonal structure of corresponding to $MnCO_3$ (JCPDS No. 44-1472) or $NiCO_3$ (JCPDS No. 12-0771), indicating that a single phase is obtained. The diffraction peaks are quite broad due to the homogenous mixed nano-scale particles as illustrated in Figure 4.3. From the ICP result, the formula of the carbonate precursor can be expressed as $(Ni_{0.25}Mn_{0.75})CO_3$.
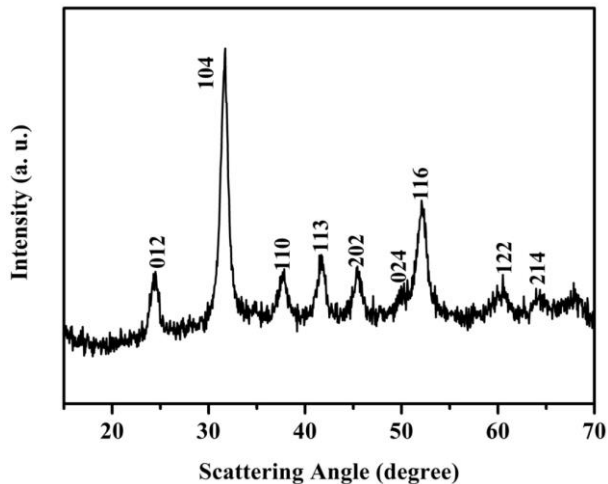
Figure 4.2. XRD pattern of the precursor powder $(Ni_{0.25}Mn_{0.75})CO_3$ synthesized by the MCP method.
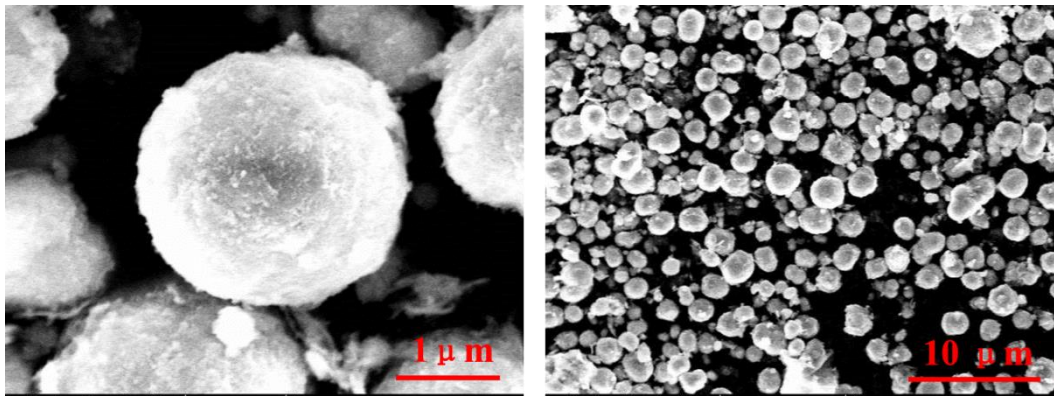
Figure 4.3. SEM images of the precursor powder $(Ni_{0.25}Mn_{0.75})CO_3$ synthesized by the MCP method.

Despite undergoing different synthesis routes, the final bulk crystal structure of products synthesized by the MCP and CCP method is quite similar to one another. Figure 4.4 shows the XRD pattern of $Li_{1.2}Ni_{0.2}Mn_{0.6}O_2$ sample synthesized by both methods. All XRD peaks in both patterns can be indexed as a hexagonal α-$NaFeO_2$ structure (space group: R-3m, NO. 166), except for a few broad peaks between 20° and 25°. The diffraction peaks between 20° and 25°

are known to be caused by the super lattice ordering of Li and Mn in the transition metal layers for the layered Li-rich oxides, which indicate the existence of Li_2MnO_3 component. Figure 4.4 shows that no difference between products synthesized by the MCP and CCP method can be detected.
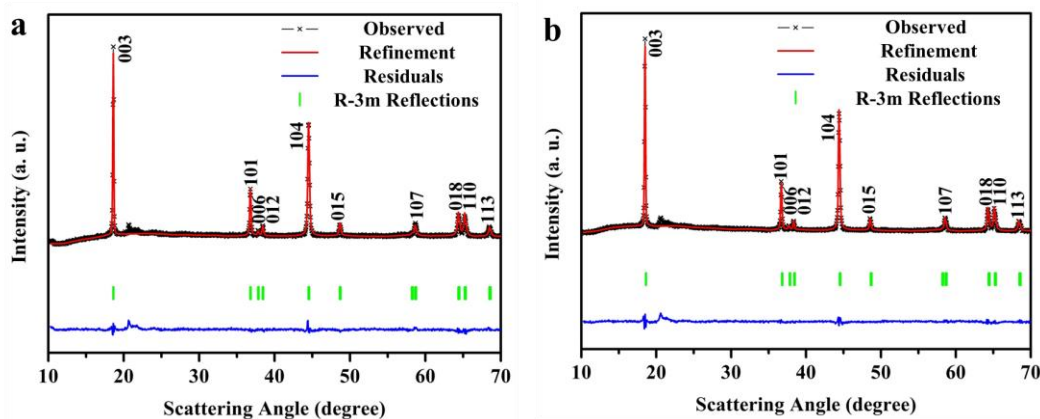
Figure 4.4. XRD spectra and Rietveld refinement of meso-structure controlled Li-rich layered oxide $Li_{1.2}Ni_{0.2}Mn_{0.6}O_2$ synthesized by the MCP method (a) and synthesized by the CCP method without meso-structure control (b).

Rietveld refinement was then taken on both samples based on the structural model R-3m. Since XRD were fit to space group R-3m, the region between 20°−25° was excluded in order to reduce the Rietveld R-factor. The results of the refinement are listed in Table 4.1. The a- and c-lattice parameters differences for both samples are determined to be within 0.1% of one another. The refined Li/Ni mixing (number of Ni^{2+} on the Li^+ site) are exactly the same, 3.4% for both products. It confirms the qualitative interpretation of the similarity in crystallinity and bulk structure of the samples synthesized by the MCP and CCP method.

Table 4.1. Rietveld fit parameters of Li-rich layered oxide $Li_{1.2}Ni_{0.2}Mn_{0.6}O_2$ synthesized by the MCP and CCP method.

Material	$a=b$ (Å)	c (Å)	z (O)	n Ni in Li layer	R_{wp} (%)	R_B (%)
MCP method	2.856(3)	14.241(8)	0.258(6)	0.034(3)	2.65	5.15
CCP method	2.854(7)	14.234(6)	0.257(6)	0.034(3)	2.39	4.20

Despite their similar crystal structures, the samples prepared by different methods adopt significantly different morphologies. Figure 4.5a and b show SEM images for the $Li_{1.2}Ni_{0.2}Mn_{0.6}O_2$ powder synthesized by the MCP method. As can be seen, the obtained product has spherical meso-structure with particle sizes in the range of 2-3 μm. These micro-spherical particles are composed of primary particles with diameters of about 150 nm on average. While, the sample synthesized by the CCP method consists of dispersive primary particles without well formed secondary particles, which brings about the increase of the specific surface area of the material. Table 4.2 shows that meso-structure controlled material has a surface area twice as small (2.00 m^2 g^{-1}) as material produced from the CCP method without meso-structure control (3.79 m^2 g^{-1}). Table 4.2 also shows experimentally determined stoichiometries of each material. They are the same as one another, and to the theoretically desired ratio of $Li_{1.2}Ni_{0.2}Mn_{0.6}O_2$. XRD, Rietveld refinement, and ICP results suggest the crystallinity and stoichiometry of the materials synthesized by different methods are very similar. However, the sample synthesized by the MCP method has a uniform spherical meso-structure and two-fold smaller surface area compared with the sample without meso-structure control synthesized by the CCP method.
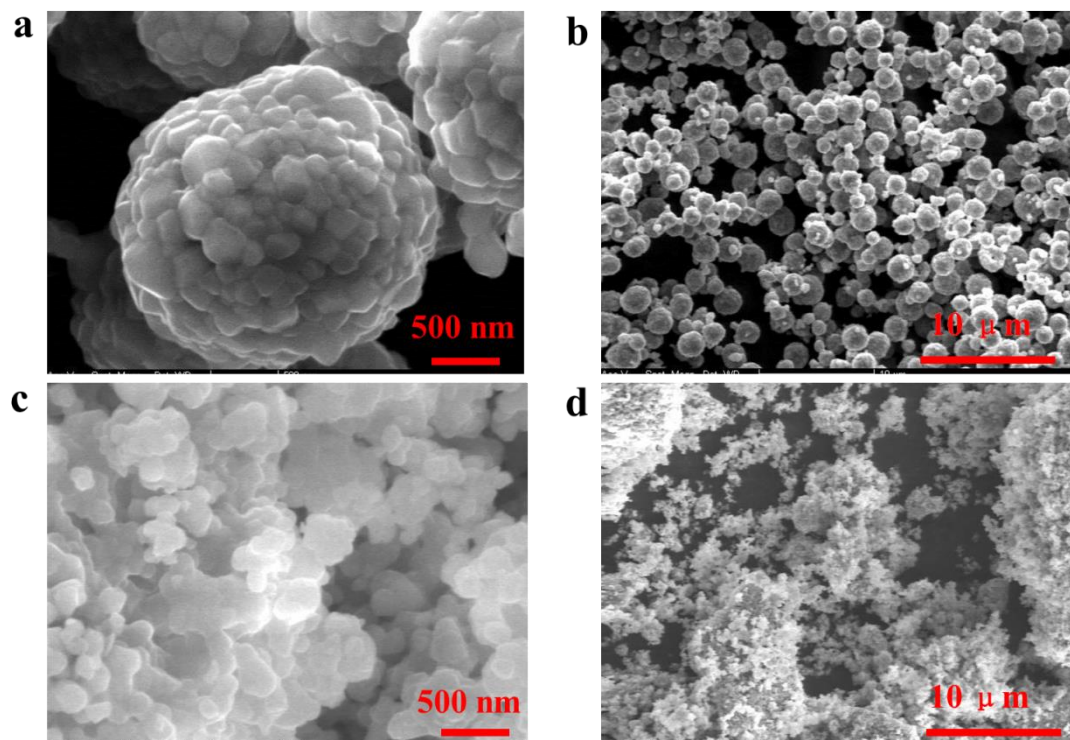
Figure 4.5. SEM images of Li-rich layered oxide $Li_{1.2}Ni_{0.2}Mn_{0.6}O_2$ synthesized by the MCP (a, b) and CCP (c, d) method.

Table 4.2. Surface area and stoichiometry of Li-rich layered oxide $Li_{1.2}Ni_{0.2}Mn_{0.6}O_2$ synthesized by the MCP and CCP method.

Material	surface area (m^2 g^{-1})	stoichiometry	
		Mn:Ni	Li:(Mn+Ni)
Theoretical		3:1	1.20:0.8
MCP method	2.00	2.98:1	1.21:0.8
CCP method	3.79	3.02:1	1.20:0.8

4.3.2. Electrochemical Performance Comparison

Figure 4.6 shows the first-cycle voltage profile of $Li_{1.2}Ni_{0.2}Mn_{0.6}O_2$ cathode synthesized by the MCP method in the voltage range of 2-4.8 V under gravimetric current density of 12.5 mA g^{-1}. The charge potential consists of a slope region and a long plateau. The slope region (<4.4 V) is attributed to the extraction of Li^+ ions from the lithium layer.[95] After this process, the Ni^{2+} is oxidized to Ni^{4+}. The subsequent long plateau is caused by a concomitant loss of oxygen from the material lattice.[96] The meso-structure controlled sample shows a high discharge capacity of 250 mAh g^{-1} at 0.05 C rate for the first cycle.
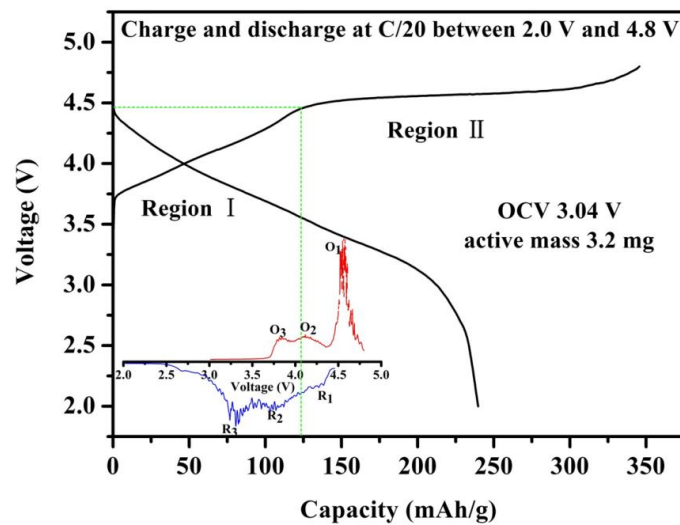
Figure 4.6. First cycle electrochemical profiles of $Li_{1.2}Ni_{0.2}Mn_{0.6}O_2$ synthesized by the MCP method; inset represents dQ/dV (y-axis) of this profile.

Figure 4.7a and b demonstrate changes in capacity and voltage during 80 cycles under a current density of 25 mA g^{-1} of both samples. To highlight the capacity loss and voltage degradation in different voltage regime, Figure 4.7c and d also show differential capacity, dQ/dV, for both samples. It is clear from this figure that all the capacity fade during discharge occurs

above 3.6 V. While the first two dQ/dV peaks, near 4.25 and 3.75 V, do not shift appreciably—reflecting the fact that there is almost no voltage degradation above 3.6 V. Voltage degradation is present mainly in the low voltage regime. Clearly, compared with the sample without meso-structure control, the meso-structure control sample not only shows a large discharge capacity (220 mAh g^{-1}) at the first cycle, but also it exhibits almost the same capacity and voltage curve after 80 cycles. At higher rate like 1.0 C, the meso-structure controlled material still exhibits better cycling performance as shown in Figure 4.8. The increasing capacity over cycles is due to the initial activation process, which is common for the meso-structure controlled sample.[97] It should be noted unlike the 20 μm size large secondary particles commonly obtained from the co-precipitation method with ammonia addition, our 3 μm size spherical particles have less kinetic limitations, which allows the material to cycle at higher current. No obvious capacity fading and voltage degradation is found for the meso-structure controlled sample even after 150 cycles.
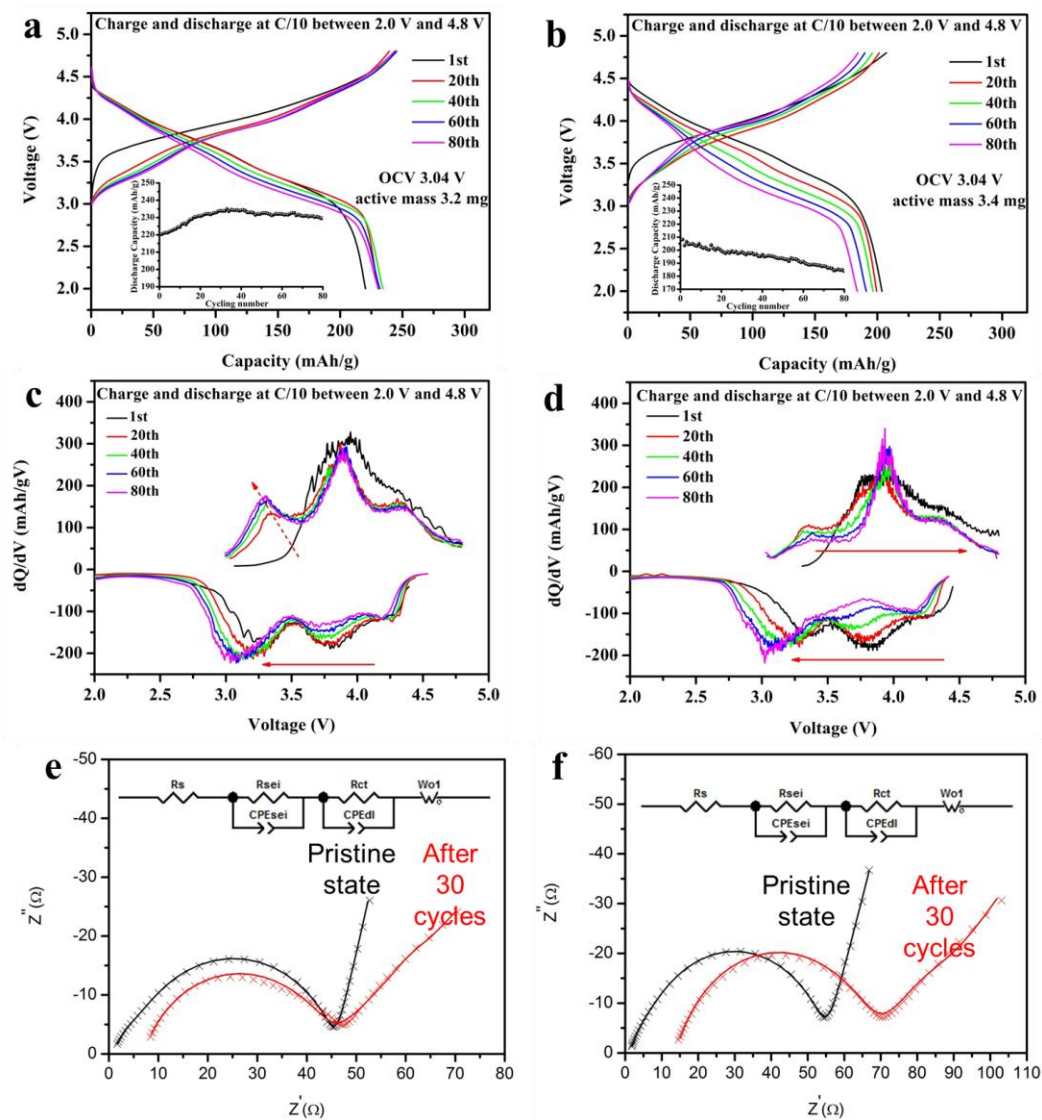
Figure 4.7. First 80 electrochemical profiles (a, b), corresponding dQ/dV plots (c, d), and Nyquist fitting plots (e, f) of Li-rich layered oxide $Li_{1.2}Ni_{0.2}Mn_{0.6}O_2$ synthesized by the MCP (a, c, e) and CCP (b, d, f) method.
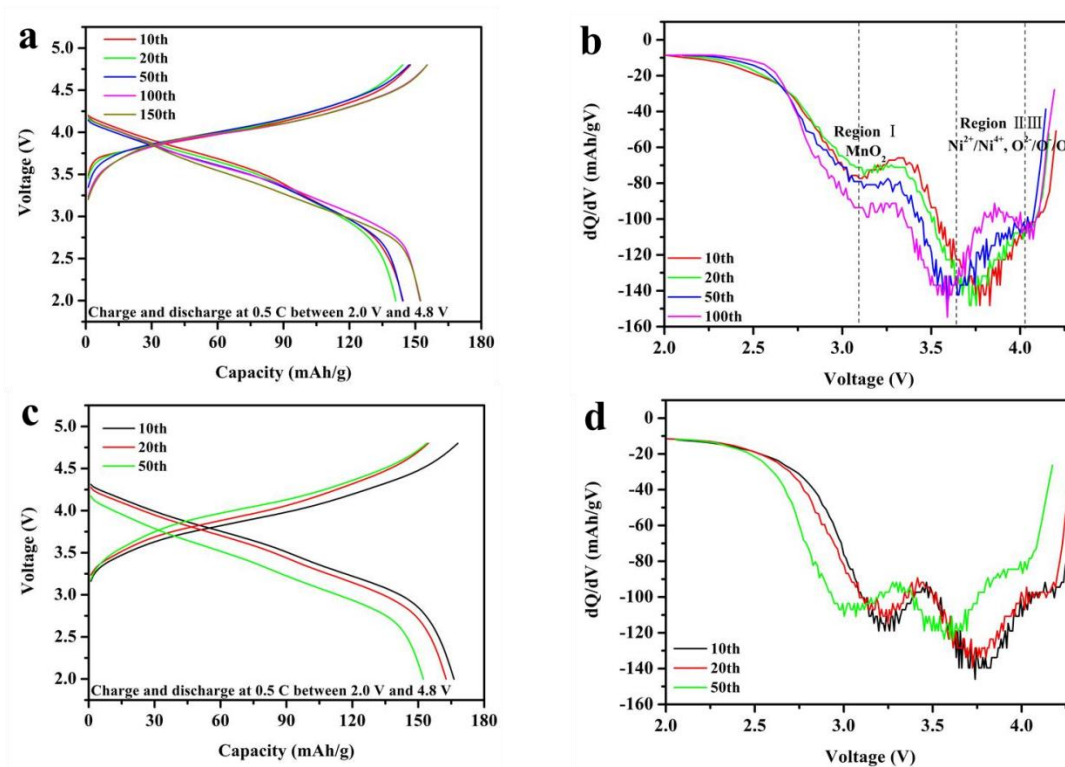
Figure 4.8. Electrochemical cycling profiles and corresponding dQ/dV plots of Li-rich material $Li_{1.2}Ni_{0.2}Mn_{0.6}O_2$ synthesized by the MCP (a, b) and CCP (c, d) method.

The improved cycling performance of the sample synthesized by the MCP method can be discussed in two aspects: (1) the meso-structure controlled sample has almost two-fold smaller surface area compared with the sample without meso-structure control (Table 4.2), which will introduce less side reactions between released oxygen and the electrolyte species. A thinner solid electrolyte interface layer is thus expected to form on the meso-structure controlled particles surface, that enables a minimized capacity and voltage fading during cycling process; Figure 4.7e and f show the Nyquist plots of the cells prepared using the sample with and without meso-structure control before and after 30 cycles at 0.1 C rate, as well as the corresponding equivalent circuit to fit the plots. R_s is the electrolyte resistance, R_{sei} and R_{ct} are the resistance for the solid electrolyte interface (SEI) and the charge transfer resistance, respectively. It turns out all the

above resistance of the meso-structure controlled sample does not increase obviously during the cycling process. The R_{sei} and R_{ct} values for the meso-structure controlled sample even decrease from 3.8 to 3.5 Ω and from 40.6 to 39.5 Ω, respectively (see Table 4.3). This also well explains the increasing capacity over cycles of the meso-structure controlled sample during the galvanostatic test. (2) uniform distributed small secondary particles (~3 μm) possess increased structure mechanical stability so that no cracks can easily occur within the secondary particles, which will introduce less stress to the whole system.

Table 4.3. Impedance parameters of Li-rich layered oxide $Li_{1.2}Ni_{0.2}Mn_{0.6}O_2$ with and without meso-structure control before and after 30 cycles at 0.1 C rate.

Sample	State	R_s (Ω)	R_{sei}(Ω)	R_{ct} (Ω)	σ
MCP method	Pristine	1.2	3.8	40.6	40.4
	30 cycles	6.9	3.5	39.5	113.7
CCP method	Pristine	1.5	4.2	48.9	66.8
	30 cycles	13.8	5.4	53.2	158.2

4.3.3. 3D TXM Analysis

In order to evaluate the designed meso-structure mechanical stability upon cycling, TXM measurements were performed on both pristine and cycled electrodes for the sample synthesized by the MCP method. The total imaging volumes is collected based on a field of view of 40 × 40 μm^2 with angular range of 180°. The data analysis was conducted after cropping a central volume of ~21,000 μm^3 from the total reconstruction. As shown in Figure 4.9a and b, The meso-structure controlled material still maintains spherical shape with ~3 μm in diameter after 100 cycles at 0.1 C rate. For comparison, large size secondary particles synthesized by the co-precipitation method with ammonia addition can easily have internal cracks. Fragmentation of primary particles due to

progressive internal cracking were observed after only 50 cycles for the large size secondary particles (see Figure 4.9c and d).[98] Cracks which can be resulted from the high stress concentrations on the rough surfaces has been taken to be an important cycling performance degradation factor.[98] Different from the secondary particles with 10~20 μm, no serious cracks appear within the secondary particles synthesized through the MCP method even after longer term cycling as revealed by 2D TXM images of the electrodes (Figure 4.9a and b). More internal pores are indeed present in the spherical secondary particles, which may indicate less agglomeration of primary particles during electrochemical cycling.
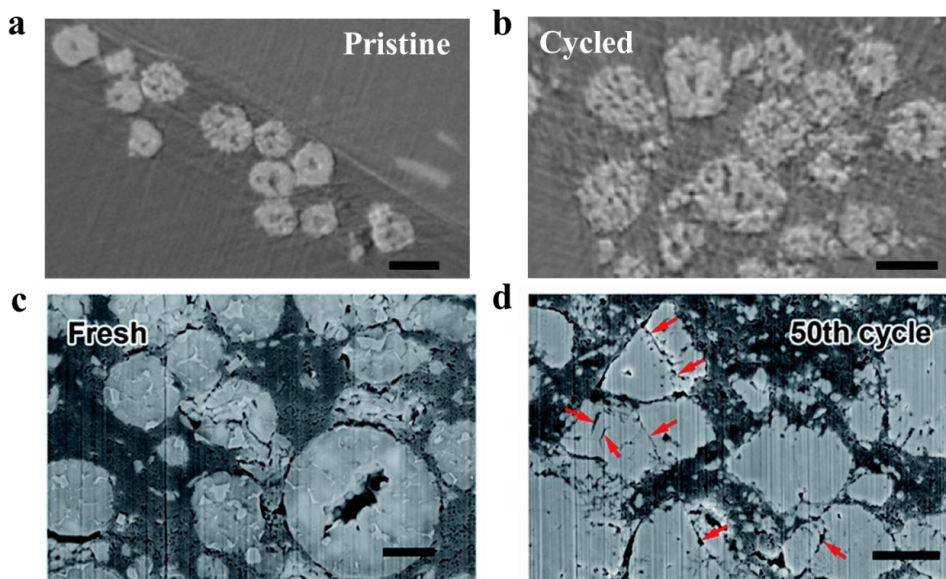
Figure 4.9. (a, b) 2D representative reconstructed slice of Li-rich layered oxide $Li_{1.2}Ni_{0.2}Mn_{0.6}O_2$ synthesized by the MCP method for the pristine electrode and cycled electrode, and (c, d) cross-sectional SEM images of Li-rich layered oxide electrodes with large secondary particles at various cycling stages reprinted with permission from previous results published by Song et al.

To carefully examine the meso-structure changes, the 3D reconstruction of a representative secondary particle is shown in Figure 4.10 for both pristine and cycled electrodes of the sample synthesized by the MCP method. Similar to the observation in the larger scale, no morphological changes are discernible after cycling except for pores or "channel-like" structure

formation within the secondary particles as indicated by the arrows in the sliced 2D images. Specific surface area density was then calculated from the 3D images as described elsewhere.[99] Analysis of the specific surface area of all the particles within the total reconstruction volume is given in Table 4.4. After 100 cycles, the specific surface area is increased from 4.5 to 6.31 μm^{-1} due to the channel formation that results in less agglomeration of the primary particles. The enhanced interfacial area could improve battery performance by decreasing Li diffusion distances, which results in the increasing capacity over initial cycles and partially explain the activation process. Nevertheless, upon long cycling, the increased interfacial area will lead to more cathode electrolyte side reactions, causing impedance increase.
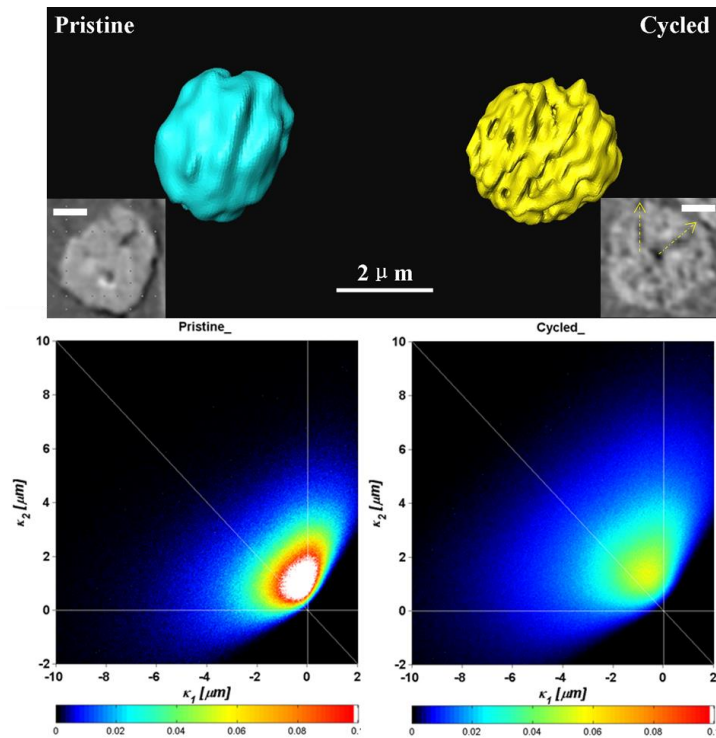
Figure 4.10. TXM reconstruction (upper panel) and curvature distribution maps (lower panel) of Li-rich layered oxide $Li_{1.2}Ni_{0.2}Mn_{0.6}O_2$ synthesized by the MCP method for the pristine electrode and cycled electrode. Inset of upper panel is 2D slice of the TXM reconstructed particles and the scale bar is 1 μm.

Table 4.4. Microstructural parameters calculated from the 3D reconstructed pristine and cycled electrodes of Li-rich layered oxide $Li_{1.2}Ni_{0.2}Mn_{0.6}O_2$ synthesized by the MCP method.

Sample	Total Reconstruction volume (μm^3)	LNMO Volume (μm^3)	Total Surface Area (μm^2)	Specific Surface Area (μm^{-1})
Pristine	21104	686.2	3100	4.5
Cycled	22613	1460.9	9221.2	6.31

"Interfacial Shape Distribution (ISD)" maps, also known as curvature distribution maps, are also generated in Figure 4.10. The principal curvature calculations were carried out using commercial package (Avizo, v.7, VSG) with"Parallel Surface Method" developed by Jinnai et al.[100] In this method, a parallel surface is formed by translating the interface along its normal by an equal distance. The area of the parallel surface depends on the parallel displacement and the interfacial curvatures. The interfacial curvatures were thus deduced from the surface area by variation of parallel displacement. Generally, particles surface with larger curvature feature will develop much higher stress during cycling than in a smooth surface.[101] This high stress will lead to fracture and pulverization of the particles, which finally causes voltage and capacity degradation during long term cycling. The ISD map shown in Figure 4.10 is a probability density map with a given of minimum and maximum principal curvatures, κ_1 and κ_2, respectively. The curvature of the particles surface is slightly increased after cycling indicating a less smooth surface, which could be due to the formation of channels. Representing the convex and concave features, the distributions of the two principal curvatures of the particles, which are based on a statistical evaluation of all particles, for the pristine and cycled electrodes are shown in Table 4.5. It confirms that geometric characteristics do not change significantly after cycling in terms of the

number of convex, saddle, concave features. These results once more manifest the stable meso-structure of the sample synthesized through the MCP method. The overall spherical meso-structure is well preserved without the formation of rough surface with high stress or cracks inside the secondary particles, which minimizes the voltage decay and capacity loss during electrochemical cycling for Li-rich layered oxide materials.

Table 4.5. Quantitative analysis of curvature distributions from the 3D reconstructed pristine and cycled electrodes of Li-rich layered oxide $Li_{1.2}Ni_{0.2}Mn_{0.6}O_2$ synthesized by the MCP method.

Sample	Convex (%)	Saddle (%)	Concave (%)
Pristine	24.3	66.1	9.6
Cycled	20	70.3	9.7

4.4. Conclusion

The meso-structure controlled Li-rich layered oxide material $Li_{1.2}Ni_{0.2}Mn_{0.6}O_2$ has been successfully synthesized through a modified co-precipitation method without ammonia addition. The obtained material has spherical secondary particles with an average diameter of approximately 3 μm. These secondary spherical particles consist of primary particles with particle size approximately 150 nm. No obvious capacity fading and voltage degradation is observed for the morphology controlled sample even after 150 cycles. Insight is provided into how the cycling performances are affected by the unique meso-structure design. Compared with the sample without meso-structure control, the meso-structure controlled sample has a much smaller surface area, which will introduce less side reactions between released oxygen and the electrolyte species. More importantly, unlike large size secondary particles which can easily have

internal cracks, the designed meso-structure still maintains spherical shape with ~3 μm in diameter during cycling. Consequently, the voltage decay and capacity loss during long term cycling have been minimized for the meso-structure controlled Li-rich layered oxide materials synthesized through the modified co-precipitation method. Long cycling duration of these materials still needs to be optimized based on the local structure transformation to fully suppress the voltage decay and capacity fading.

This chapter in full, is currently being prepared for submission for publication "Modified Co-precipitation Synthesis of Meso-structure Controlled Li-rich Layered Oxides for Minimizing Voltage Degradation", Zhang, M.; Liu, H. D.; Liu, Z.; Fang, C.; Meng, Y. S. The dissertation author was the primary investigator and first author of this paper. All of the experiment parts were performed by the author except for the TXM measurement.

Chapter 5. Gas-solid Interfacial Modification of Oxygen Activity in Layered Oxide Cathodes for LIBs

5.1. Introduction

The functionality of many transition metal oxides can be significantly altered by oxygen vacancies on the surface. Oxygen vacancies can behave as charge carriers for solid-oxide fuel cells, as well as significant adsorption sites and as active sites for electro-photocatalysts.[102, 103] In Li-ion cathode materials, these vacancies play a vital role in determining the material's electron and ion transport properties.[104-106] The influence of oxygen vacancies at the surface on electrochemical performance was completely different in various types of Li-ion cathode materials.[107-109] Li-rich layered oxides, either as a solid solution, or as nano-composites of layered Li_2MnO_3 and $Li(TM)O_2$ (TM=Ni, Co, Mn), draw significant attention as the next-generation cathode materials for high-energy-density Li-ion batteries in electric vehicles (EVs).[110] Over the past twenty years, the discharge capacity at room temperature of these cathode materials was improved from 200 mAh g^{-1} given in the first report to over 320 mAh g^{-1} today as summarized by Hy and co-workers, even higher at elevated temperatures.[51, 111] While the research has continued to push the limits of the available capacity of the materials throughout the years, debates on the origins of the ultrahigh capacity beyond the redox of transition metal have intensified recently.

Numerous studies exemplify the contributions of bulk and surface oxygen on high charge-discharge capacity in Li-rich layered oxides, although this hypothesis has not been fully verified.[112-116] Tarascon and co-workers concluded the extra-high capacity is mainly attributed to the reversible anionic redox processes (O^{2-}/O_2^{2-} or O^{2-}/O_2^{n-}, where $3 > n > 1$) within the bulk of Li-rich layered oxides.[115] Delmas and co-workers proposed that surface oxygen is oxidized to O_2 gas, and irreversibly lost from the structure, leaving some oxygen vacancies on the surface or in

the sub-surface layers.[113, 114] Our previous work illustrates that oxygen vacancies generated during the high-potential electrochemical process can facilitate the migration and surface structural transformation of transition metals, finally leading to their potential degradation during extended cycles.[58, 60]

To reduce oxygen gas generation and utilize reversible oxygen redox activity during charging and discharging, oxygen vacancies have been proposed to form on the surface of the as-synthesized Li-rich layered oxides before electrochemical process. The influence of the surface oxygen vacancies on the oxygen gas generation is discussed as follows: during the operation at high potential, the electrochemical activation of Li_2MnO_3 component is involved with the activity of lattice oxygen in Li-rich layered oxides. In this process, this will lead to generating some oxygen vacancies and oxygen gas simultaneously, especially on the surface. The formation of oxygen vacancies can be simply represented by:

$$O_O \rightarrow \frac{1}{2}O_2 + V_{\ddot{O}} + 2e^{'}$$

(5.1)
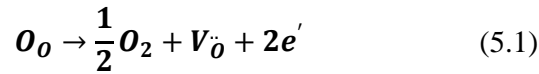
Assume that these defects are noninteracting, the law of mass action would be in its simplest form with concentrations instead of activities. In this case, the equilibrium constant K for this reaction is:

$$K = [V_{\ddot{O}}][e^{'}]^2 P_{O_2}^{1/2}$$

(5.2)

Where the brackets [ ] denote concentrations. Equation (5.1) shows that the concentrations of oxygen vacancies and electrons are related:

$$[e^{'}] = 2[V_O^{''}]$$

(5.3)

Hence

$$K = 4[V_{\ddot{O}}]^3 P_{O_2}^{1/2} \qquad\qquad (5.4)$$

Therefore, the oxygen partial pressure of P_{O_2} is given by:

$$P_{O_2} = \frac{K}{16[V_{\ddot{O}}]^6} \qquad\qquad (5.5)$$

The oxygen partial pressure is found to be sensitive to the concentration of oxygen vacancies in the lattice, especially on the particle surface. Based on the above results, the oxygen partial pressure will be less for the sample with surface oxygen vacancies than that of the sample without any oxygen vacancies. Accordingly, this means that the presence of oxygen vacancies on the surface will suppress the generation of oxygen gas. The creation of surface oxygen vacancies was previously attempted utilizing a reducing atmosphere and leaching with acid accompanied by heat treatment.[117-120] However, the bulk structure reported in previous work easily transforms from a pure layered phase to spinel- and/or rock-salt phases that significantly damages the rate capability and cycling stability.[121-123]

Motivated by the considerations above, we propose, for the first time, a strategy based on a gas-solid interface reaction (GSIR) between Li-rich layered oxides and carbon dioxide gas to create oxygen vacancies on the particles' surface. The schematic of GSIR process between Li-rich layered oxides and carbon dioxide is displayed in Figure 5.1a, and the procedure is detailed in the Methods section. Oxygen vacancies in the surface regions up to 20 nm thick are created on the particles without affecting structural integrity. After the surface modification, the target material $Li[Li_{0.144}Ni_{0.136}Co_{0.136}Mn_{0.544}]O_2$ exhibits discharge capacity as high as 300 mAh g^{-1} with no obvious voltage degradation after 100 cycles at a current density of 25 mA g^{-1}. As confirmed by both theoretical calculations and experimental characterizations, these greatly improved electrochemical performances are ascribed to the full utilization of oxygen activity

through the creation of oxygen vacancies on the surface of the as-synthesized Li-rich layered oxides.
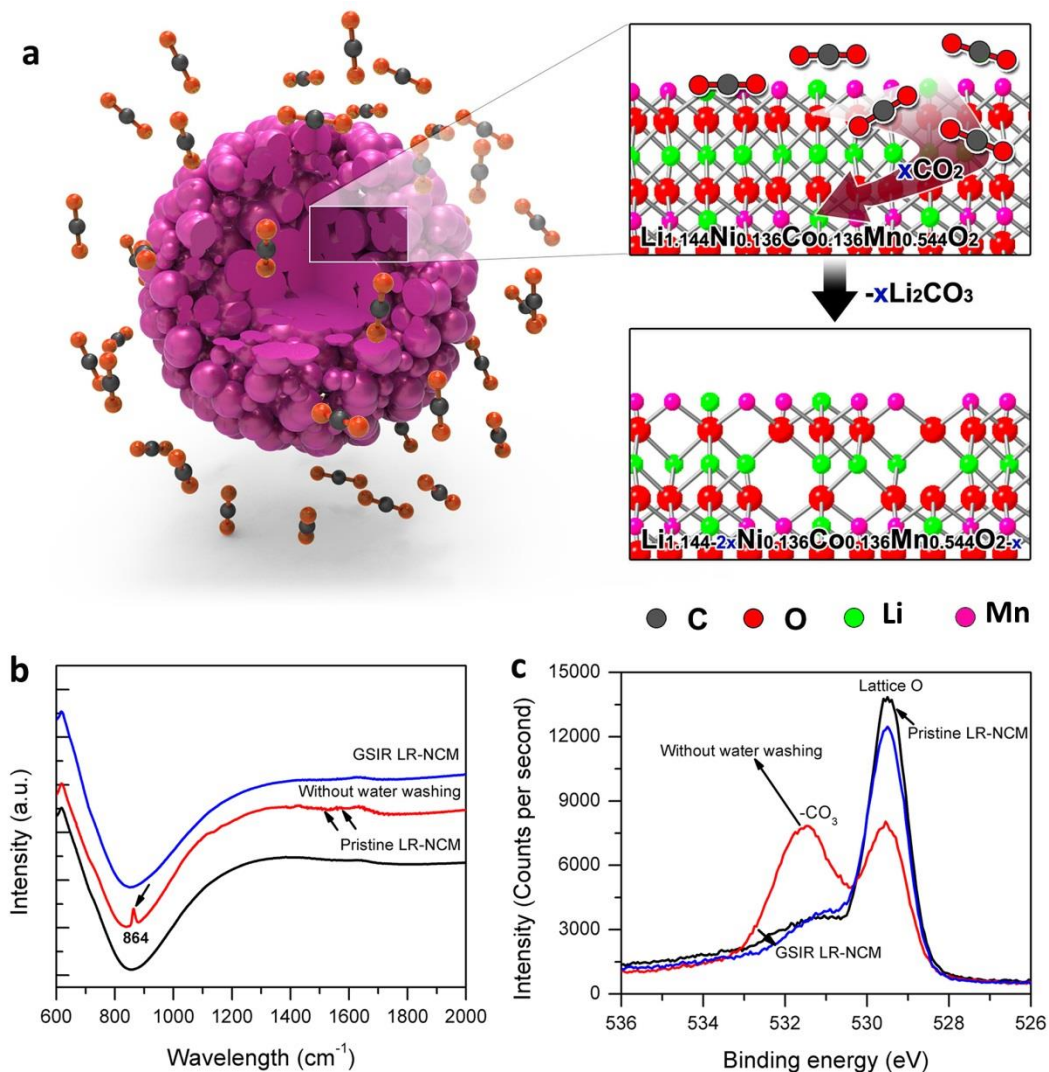
Figure 5.1. Gas-Solid Interface Reaction (GSIR). a. Schematic of gas-solid interface reaction between Li-rich layered oxides and carbon dioxide. b. Fourier transformed infrared Spectrum (FTIR). c. X-ray photoelectron spectroscopy (XPS) spectra of the O 1s.

5.2. Experimental

5.2.1. Gas-solid Interfacial Reaction (GSIR) Process

The synthesis procedures of $Li[Li_{1.144}Ni_{0.136}Co_{0.136}Mn_{0.544}]O_2$ were detailed as below: we pumped an aqueous solution containing $NiSO_4 \cdot 6H_2O$, $CoSO_4 \cdot 7H_2O$, and $MnSO_4 \cdot 4H_2O$ with a concentration of 2.0 mol L^{-1} into a continuously stirred tank reactor (CSTR, capacity of 50 L); at the same time, a 2.0 mol L^{-1} Na_2CO_3 solution, and a 0.2 mol L^{-1} NH_4OH solution were added separately into the reactor. The co-precipitation temperature was held at 60 ℃, and the pH value was fixed to 7.8. The resulting $(Ni_{1/6}Co_{1/6}Mn_{4/6})CO_3$ powders were washed several times with distilled water to remove residual Na^+, and dried in a vacuum oven at 80 ℃ for over 20h. The resulting precipitates were mixed with Li_2CO_3 and the exact molar ratio between them was 0.7. The mixed powders firstly were pre-treated at 500 ℃ for 5 h in the air and then calcinated at 850 ℃ for 15 h in the air. Then, they were cooled to room temperature in the furnace. The as-obtained sample was labeled pristine LR-NCM.

The GSIR process of the pristine LR-NCM sample with CO_2 was carried out as follows: a set amount of LR-NCM cathode materials and a given amount of NH_4HCO_3, which is as the source of CO_2 after decomposition at certain temperatures, were placed in an enclosed reactor in an argon-filled glove box ($O_2 < 0.1$ ppm) with a total volume of 100 mL, and heated at 200 ℃ for 10 h. The optimal molar ratio between carbon dioxide and Li-rich layered oxides was about 1:5. It is important that the pristine LR-NCM cathode materials and the NH_4HCO_3 must be separated at the beginning for ensuring a homogeneous gas-solid interface reaction. To remove the reaction products on the surface of the LR-NCM, the sample obtained was washed with water several times and dried at 120 ℃ for 12h. The as-obtained product was termed the GSIR LR-NCM.

5.2.2. Materials Characterizations

A field-emission scanning electron microscopy (FESEM) image was acquired on a Hitachi S-4800. A Fourier transform infrared spectroscopy (FTIR) analysis was performed on a pellet made of active materials and KBr powder, using an FTIR spectrometer (Nicolet, 6700 series, USA). X-ray photoelectron spectroscopy (XPS) measurements were collected using an AXIS Ultra DLD spectrometer with Al Kα (1253.6 eV) radiation, to investigate the changes in the compositions on the cathode surface. The compositions of the pristine, and GSIR LR-NCM sample were confirmed quantitatively by inductive coupled plasma-Atomic Emission Spectrometry (ICP-AES) with an emission spectrometer (Optima 2100 DV, Perkin-Elmer). The tap density of the pristine LR-NCM sample was measured and calculated by tap density instrument (FSZ-4, Ruike).

The time of flight (TOF) powder neutron diffraction (ND) data were collected on the VULCAN beamline at the Spallation Neutron Sources (SNS) in the Oak Ridge National Laboratory (ORNL).[124] Around 0.6 g of powder was packed into a vanadium sample can. An incident beam (5mm by 12mm) of 0.7- to 3.5-Å bandwidth allowing a 0.5~2.5 Å d-spacing in the diffracted patterns in the $\pm 90°$ 2θ detector banks was selected, using the double-disk choppers at a speed of 30 Hz. A high- resolution mode was employed with Δd/d ~0.25%. The SNS was at a nominal 1100KW. Powder-neutron-diffraction data were collected at a high-resolution mode for 3 h and reduced by the VDRIVE software. Full-pattern Rietveld refinement was performed using the GSAS programs with the EXPGUI interface.[125]

Transmission electron microscopy (TEM) images and electron energy-loss spectroscopy (EELS) spectra were carried out using the JEM-ARM200CF scanning/transmission electron microscope at Brookhaven National Laboratory. The instrument is equipped with a cold field-

emission source, two aberration-correctors, and a high-resolution dual electron energy-loss spectrometer (Quantum GIF). The optimal energy-resolution was ~0.35eV, as judged by the full-width at half-maximum of the zero-loss peak. Spectra were recorded either using a convergent-beam in scanning TEM (STEM) mode, or parallel-beam in TEM mode, for diffraction, imaging and spectroscopy. The refinement Mn L_3, and L_2 energy, and L_3/L_2 intensity ratio were based on Pearson method.[126]

Synchrotron X-ray diffraction data (SXRD) were collected using beamline BL14B1 at the Shanghai Synchrotron Radiation Facility (SSRF). These data were recorded in the 2θ range between 10° and 85°, using a fixed wavelength of 1.2398 Å. The structural composite study was carried out by Rietveld refinement analysis, using the GSAS program. For X-ray absorption fine structure spectroscopy (XAFS) studies, we conducted measurements at beamline BL14W1 of the SSRF. The incident beam was mono-chromatized using a Si (111) fixed-exit, double-crystal monochromator. Foils of nickel, manganese, and cobalt were used for energy calibration with zero energy (E_0), defined according to Kraft et al.[127] Spectra were acquired in transmission mode, utilizing gas-ionization chambers as detectors. Data on X-ray absorption near edge structure (XANES) was extracted with established methods using the ATHENA software package.

The negative electrodes were prepared by casting the slurry with a mixture of 80 wt.% the pristine or GSIR LR-NCM, 10 wt.% acetylene black, and 10 wt.% polyvinylidene fluoride binder on an aluminum foil. Electrode discs of 13mm diameter were punched from the negative electrode, pressed at 8 Mpa per disc, and dried at 80 ℃ for 12 h in vacuum to remove any residual NMP and traces of water. The prepared electrodes then were assembled in an Ar-filled glove box (H_2O < 0.1 ppm and O_2 < 0.1 ppm). Metallic Li was used as the counter electrode, and Celgard 2502 as a separator. The electrolyte solution was 1M $LiPF_6$ in a 3: 7 (volume ratio)

mixture of ethylene carbonate (EC)-dimethyl carbonate (DMC, Zhangjiagang Guotai-Huarong New Chemical Materials Co., Ltd.). The cells were galvanostatically charged and discharged on a LAND-CT2001A battery-test system. Unless otherwise specified, the cells typically cycled between 2.0 V and 4.8 V *vs.* Li^+/Li^0, and the temperature for testing was about 28 ℃. Electrochemical impedance-spectroscopy (EIS) measurements were conducted on an Autolab83710 impedance analyzer with AC voltage amplitude of 5 mV, and frequency range of 0.01 Hz - 100,000 Hz. The metallic Li served as both the counter and reference electrodes during the EIS measurements.

Operando differential electrochemical mass spectrometry (DEMS) analysis was carried out to detect the gases generated during the initial charge-discharge process. The DEMS cell was assembled in an Ar-filled glove box. 1 M $LiPF_6$ in 1:1 EC: DMC was used as the electrolyte, and a glass-fiber filter (Whatman GF/D) was used as a separator. Electrodes were prepared by casting a slurry with a composition of 80 wt. % active materials, 10 wt. % Super C65 (Timcal), and 10 wt.% PVDF (Kynar FLEX 761A, Arkema Group) on to an aluminum current-collector foil. Electrode tapes then were punched into 22-mm diameter discs, and dried at 120 ℃ in an under vacuum oven for 24 h. The electrodes were assembled into Swagelok-type cells, using metallic Li as both the counter and the reference. Thereafter, the cell was connected to the mass spectrometer. The cell was purged continuously with gaseous Ar which flowed from the cell into the mass spectrometer carrying the evolved gases for MS analysis. *Operando* DEMS cells were conducted on a VSP electrochemical workstation (Biologic, France). The mass signals were recorded as a function of time and the cell voltage. The time resolution of ion-current intensity is optimized by selectively scanning the *m/z* 32 and 44 signals. In line with previous studies, only O_2 and CO_2 were evolved during the initial cycling of Li-rich layered-oxide electrodes.[128, 129]

5.2.3. Computation Methodology

First-principles calculations were performed in the spin-polarized GGA+U approximations to the Density Functional Theory (DFT). The core electron states were represented by the projector augmented-wave method as implemented in the Vienna ab-initio simulation package (VASP).[130-133] We used the Perdew-Burke-Ernzerhof exchange correlation, and a plane-wave representation for the wave function with a cutoff energy of 450 eV.[134] The Brillouin zone was sampled with a dense k-points mesh by Gamma packing. Our supercell, composed of 24 formula units of $Li[Ni_{1/4}Li_{1/6}Mn_{7/12}]O_2$, used in our previous work was employed again to obtain the site's stability and activation barrier. The Hubbard U correction was introduced to describe the effect of localized d electrons of the transition-metal ions. The applied effective U value given to Mn ions is 5 eV, and that to Ni ions is 5.96 eV.[135] In this calculation, a concentration of Li20/28 was applied, in which the GSIR LR-NCM exhibits a difference in electrochemical performance compared with pristine LR-NCM. The Nudged Elastic Band (NEB) method was used to find the minimum energy path and the energy barrier for Li diffusion inside the materials.

5.3. Results and Discussion

5.3.1. Characterizations of Oxygen Vacancies after GSIR Process

Li-rich layered oxide $Li[Li_{0.144}Ni_{0.136}Co_{0.136}Mn_{0.544}]O_2$ (denoted as LR-NCM) was prepared by a co-precipitation method (see Methods section). After the GSIR process is completed, the general morphology remains the same as in the pristine LR-NCM. Both synchrotron X-ray diffraction (SXRD) refinements, and transition metal K-edge X-ray absorption near-edge structure (XANES) show no major difference for the pristine and GSIR LR-NCM samples (Figures. 5.2 and 5.3). These results preliminarily imply that the GSIR

process does not heavily influence the average crystal structures and bulk electronic environments of the LR-NCM sample.
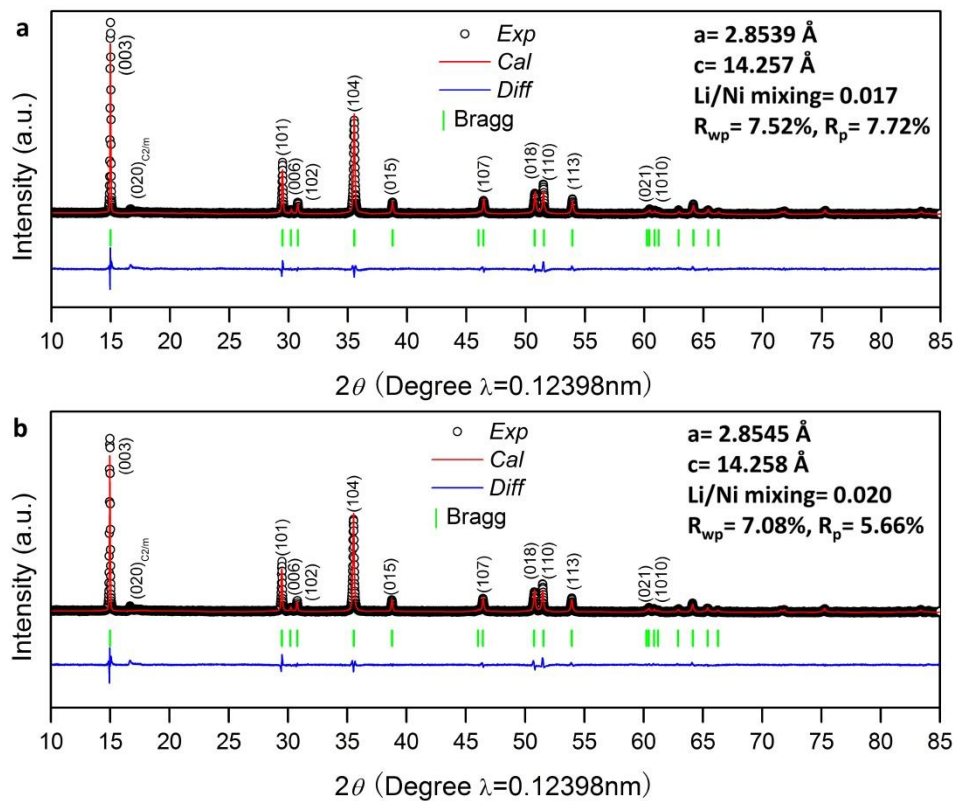
Figure 5.2. Structural characterization of the pristine and GSIR LR-NCM. Synchrotron X-ray diffraction (SXRD) patterns for the pristine (a) and GSIR LR-NCM (b).
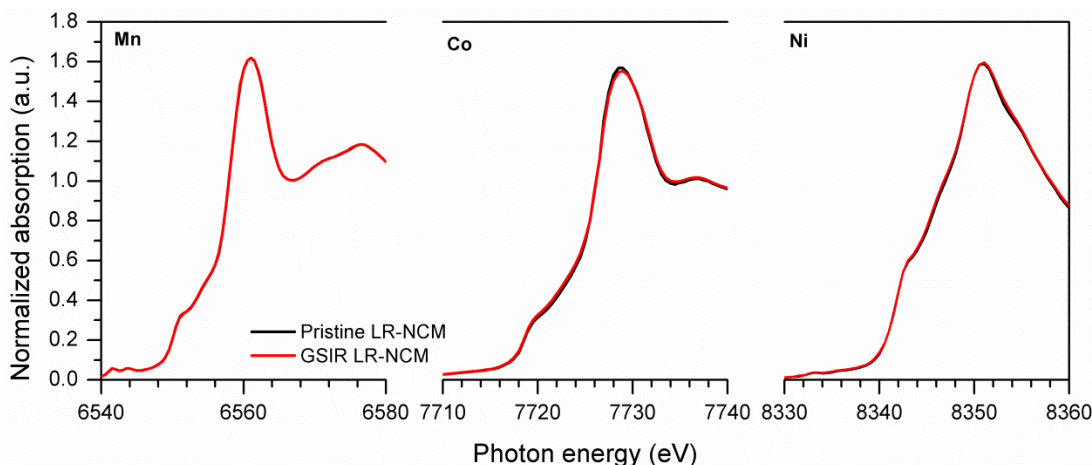
Figure 5.3. Structural characterization of the pristine and GSIR LR-NCM. Normalized K-edge X-ray absorption near edge structure (XANES) spectra for the pristine and GSIR LR-NCM.

To investigate the GSIR reaction mechanism of the formation of surface oxygen vacancies, we applied Fourier transformed infrared spectroscopy (FTIR) and X-ray photoelectron spectroscopy (XPS) to three samples (Figure 5.1b-c). The FTIR results (Figure 5.1b) indicate that carbonate formed on their surfaces after the GSIR. The lithium concentration of the GSIR LR-NCM is slightly lower (6.4 %) than that of the pristine LR-NCM, as was determined by inductive coupled plasma-atomic emission spectrometry (ICP-AES). On the other hand, in the oxygen 1s XPS spectra (Figure 5.1c), the intensity of the binding energy at 529.5 eV representing TM-O covalency for the GSIR LR-NCM after washing is much lower than that of the pristine LR-NCM. In contrast, the intensity of the binding energy at 531.5 eV representing the carbonate group (-CO$_3$) for the GSIR LR-NCM without washing is much larger.[136, 137] Both changes indicate some lattice oxygen was extracted by CO$_2$, forming oxygen vacancies on the sub-surfaces.

The amount of oxygen vacancies in the GSIR sample was determined by neutron diffraction (ND), a technique with high sensitivity for detecting light elements, such as Li and

O.[138] Figure 5.4a-b demonstrate the as-collected time-of-flight (TOF) ND patterns with *Rietveld* refinement for both samples (patterns refined with a solid solution of *R-3m* symmetry; the normalized TOF ND patterns are shown in Figure 5.5). The lattice parameters of the pristine layer are a = 2.8445(2) Å, and c = 14.2113(9) Å. The oxygen occupancy of the pristine LR-NCM is 99.97 ±1.10%. In comparison, the lattice parameters of the GSIR LR-NCM are a = 2.8526(8) Å and c = 14.2503(7) Å, which are slightly larger than those of the pristine LR-NCM. The oxygen occupancy is reduced to 96.21 ±1.20% after surface modification. The amount of Ni^{2+} in the Li layer, and the occupancy of Li in the Li layer are also slightly larger than that of in the pristine LR-NCM. In addition, the data also were analyzed using the two-phase model that is a combination of $LiTMO_2$ (*R-3m*) phase, and Li_2MnO_3 (*C/2m*) phase. The results show that no oxygen vacancies (V_O) were observed in the pristine LR-NCM sample, while the GSIR LR-NCM sample exhibited 7.20±3.3% V_O on the 4i site and 3.8±3.0% V_O on the 8j site in Li_2MnO_3 phase, and, 2.96±1.86% V_O in the overall composition. Both models are consistent with the observed oxygen vacancies in the GSIR LR-NCM. The lower oxygen occupancy in the GSIR LR-NCM reveals that the oxygen vacancies were successfully created after applying the GSIR process.
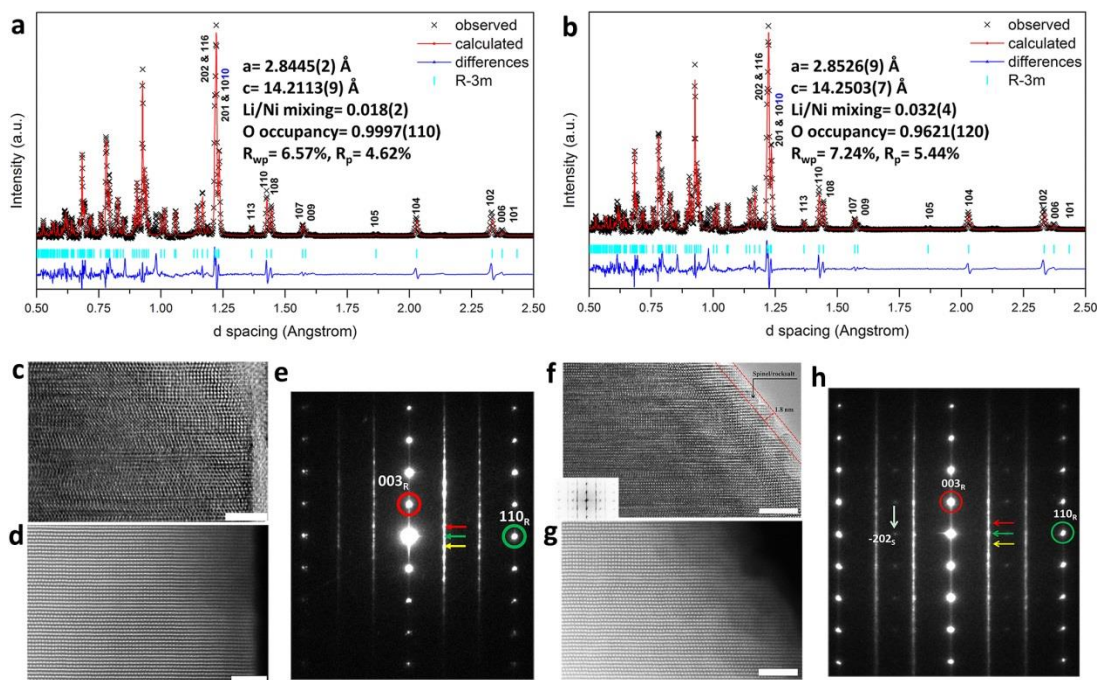
Figure 5.4. Structural characterizations of the pristine and GSIR LR-NCM. a-b. Time of flight neutron diffraction (ND) patterns for the pristine and GSIR LR-NCM. c. High-resolution transmission electron microscopy (HRTEM) image and d. high-angle annular dark field - scanning TEM (HAADF-STEM) image for the pristine LR-NCM; e. electron diffraction (ED) pattern for the pristine LR-NCM. f. HRTEM image with fast Fourier transform (FFT) about the surface and g. HAADF-STEM image for the GSIR LR-NCM; h. ED for the GSIR LR-NCM.
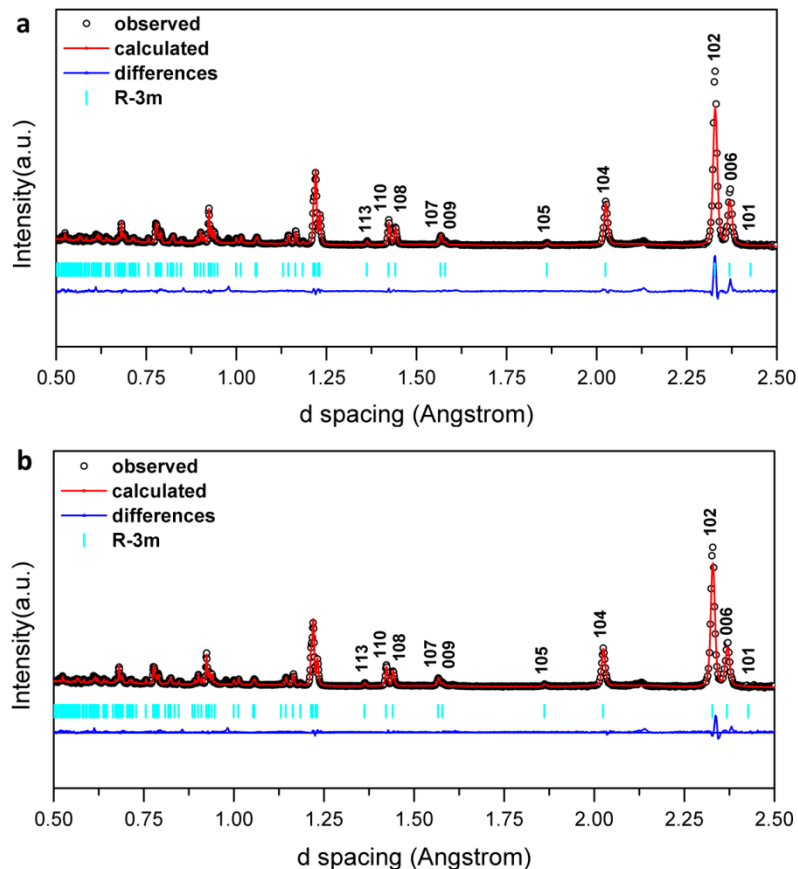
Figure 5.5. Normalized neutron diffraction (ND) patterns for the pristine and GSIR LR-NCM. a. Pristine LR-NCM; b. GSIR LR-NCM.

High-resolution transmission electron microscopy (HRTEM) (Figure 5.4c and f) was employed to further illustrate the changes between the pristine and GSIR LR-NCM. A clean surface with Li and TM layers extending to the very edge of atomic planes was observed in the pristine LR-NCM (Figure 5.4c). Meanwhile, a non-uniform surface (varying in thickness from 10 nm to 20 nm) was detected on the GSIR LR-NCM sample. In addition, high-angle annular-dark-field scanning-TEM (HAADF-STEM) images (Figure 5.4d and g) for the pristine and GSIR LR-NCM were compared to demonstrate the lack of any obvious structural change. Although electron diffraction (ED) from some particles showed spinel/rock-salt-like phase in the GSIR LR-NCM compared to the pristine LR-NCM sample (Figure 5.4e and h), it should be noted this

phase transformation only occurs on the surface of GSIR LR-NCM within several atomic layers, as indicated in Figure 5.4f, while the oxygen vacancy presence are 10-20 nm deep. These results are consistent with our SXRD and ND refinements, which verify that the GSIR process does not significantly alter the bulk structure.

Electron energy loss spectroscopy (EELS) mapping was applied to compare relative surface composition changes for the pristine and GSIR LR-NCM sample (Figure 5.6a and b). Oxygen reduction at mixed color images is well demonstrated on the edge of GSIR LR-NCM in comparison with the pristine LR-NCM. To study the electronic states of oxygen and transition metal from the particle, EELS was collected at different positions from bulk to surface of the GSIR LR-NCM (represented by colors in Figure 5.6c and d). The spectra of the O K-edge main peaks in Figure 5.6e are normalized with the Mn L_3 peak. Interestingly, we observed reduced O pre-peak intensities from the surface in the GSIR LR-NCM sample. The weak pre-peak intensities can be even seen at 20 nm for the GSIR LR-NCM sample, although the difference is small. The reduced ratio of the O-K edge pre-peak intensities to the main peak could result from a change in the local environment of oxygen, especially from the formation of oxygen vacancies. The relative distribution of chemical composition is plotted in Figure 5.6f. The content of O on average is 55% in the first 10 nm surface layer compared to the bulk value of 65%. The Mn $L_{3,2}$ white lines provide information on Mn valence (oxidation); The Mn $L_{3,\,2}$ white lines for the GSIR LR-NCM sample display a significant energy shift, and their L_3/L_2 intensity ratio remains low until 20 nm away from the surface of the GSIR LR-NCM sample (Figure 5.6g), indicating a lower Mn valence on the particles' surface. When oxygen vacancies are created on the particles' surface, the valence of Mn is reduced simultaneously with the extraction of Li to compensate for the changes in charge. Therefore, as confirmed by both the ND and STEM/EELS results, oxygen

vacancies have been successfully introduced on the 10-20 nm of the surface without a noticeable interruption in the bulk-structure through this GSIR approach.
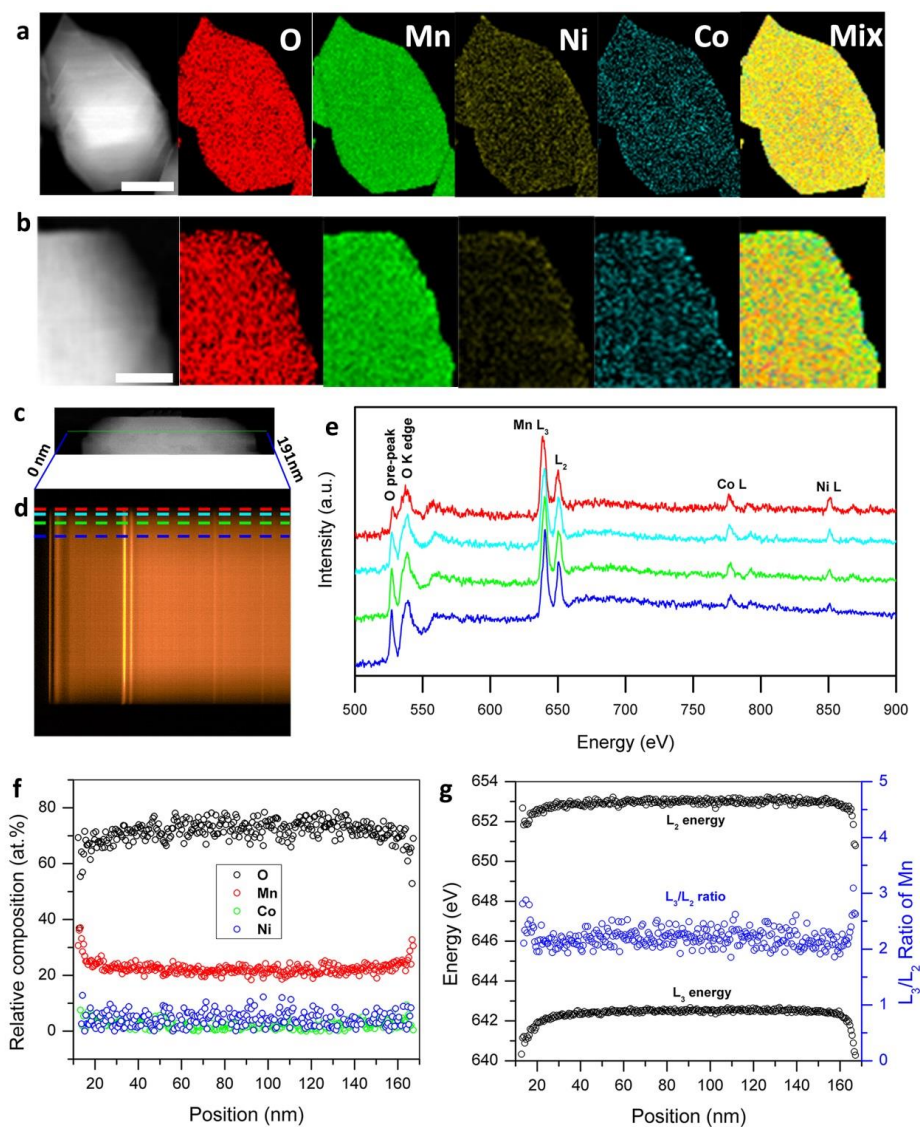
Figure 5.6. Relative surface composition changes for the pristine and GSIR LR-NCM. a. EELS spectrum images for the pristine LR-NCM. The scale bar is 50 nm; b. the GSIR LR-NCM. The scale bar is 25 nm; c. STEM image of a particle of the GSIR LR-NCM. d. EELS spectrum image from the vertical green line (0 - 191 nm) in the left STEM image (c). e. EELS spectrum profiles from the surface to the interior as marked by the horizontal dash lines with the same color in (d). f. Relative atomic composition of O (black), Mn (red), Co (blue), and Ni (green) as a function of position calculated based on integrated EELS peak intensity in (e). g. Mn L_3, and L_2 energy (top and bottom) from refinement, and L_3/L_2 intensity ratio.

5.3.2. Electrochemical Properties

CR2032 coin-cells with metallic Li as the counter electrode were assembled to investigate the electrochemical performance of the pristine and GSIR LR-NCM samples. Similar to other Li-rich layered oxides, both of them (see Figure 5.7a) exhibit a long plateau region at ~ 4.5 V *vs.* Li^+/Li^0, which usually is ascribed to the electrochemical activation of the Li_2MnO_3 component during the initial charge process, although an electrolyte/electrode side reaction is expected in this region. Interestingly, the value of the initial discharge capacity for the GSIR LR-NCM can reach as high as 301 mAh g^{-1}, compared to that of 276 mAh g^{-1} for the pristine LR-NCM. The initial coulombic efficiency also increases from 83.8% to 93.2%. The corresponding differential capacity *vs.* voltage (*dQ/dV*) curves are plotted in Figure 5.7b. A lower shift in the oxidation peak after the GSIR process is due to the decrease in electrochemical impedance (see Figure 5.8 and Table 5.1). In addition, the decline of the oxidation peak around 4.5 V *vs.* Li^+/Li^0 observed in the enlarged *dQ/dV* curves (inset in Figure 5.7b) indicate that the GSIR process has pre-activated the Li_2MnO_3 component responsible for the 4.5 V plateau. The rate capability and cycling stability further highlight the advantages of our GSIR LR-NCM sample (see Figure 5.7c). At all tested rates, the GSIR LR-NCM exhibits a higher capacity than does the pristine LR-NCM. The unique characteristic at different rates for the GSIR LR-NCM is that the additional discharge capacity results only from the lower potential region (<3.5 V vs. Li^+/Li^0). It is remarkable that the GSIR LR-NCM delivers a higher discharge-capacity of 298 mAh g^{-1} when it returns to the 0.1 C-rate, compared to that of 288 mAh g^{-1} for the pristine LR-NCM. More importantly, the charge-discharge plots at subsequent cycles for the GSIR LR-NCM demonstrate a slight degradation in potential after 100 cycles, even for a discharge capacity as high as 300 mAh g^{-1}.

To evaluate the stability of the GSIR LR-NCM, a more challenging measurement was selected (see Figure 5.7d and e). Cells based on the GSIR LR-NCM show a higher initial

capacity of 306 mAh g^{-1} (0.5 C-rate), and 280.9 mAh g^{-1} (1.0 C-rate), compared with that of 287 mAh g^{-1} (0.5 C-rate) and 269 mAh g^{-1} (1.0 C-rate) for the pristine LR-NCM at the elevated temperature of 55 ℃. The initial charge-discharge curves (see Figure 5.9a and b) are similar to the results at room temperature (see Figure 5.7a). In addition, the cells based on the pristine LR-NCM displays only 223 mAh g^{-1} (at 0.5 C-rate) and 179 mAh g^{-1} (at 1.0 C-rate) after 100 cycles and 150 cycles, respectively, whereas the GSIR LR-NCM shows an excellent capacity of about 290 mAh g^{-1} (at 0.5 C-rate), and 262 mAh g^{-1} (at 1.0 C-rate) during the same cycling period. Moreover, the charge-discharge plots of subsequent cycles (see Figure 5.9) for the GSIR LR-NCM exhibit much slower potential degradation profiles at different rates than do those of the pristine LR-NCM (see Figure 5.9). This difference clearly signifies that surface oxygen vacancies introduction in Li-rich layered oxides without severe structure destruction has a dramatic effect on improving electrochemical performance.
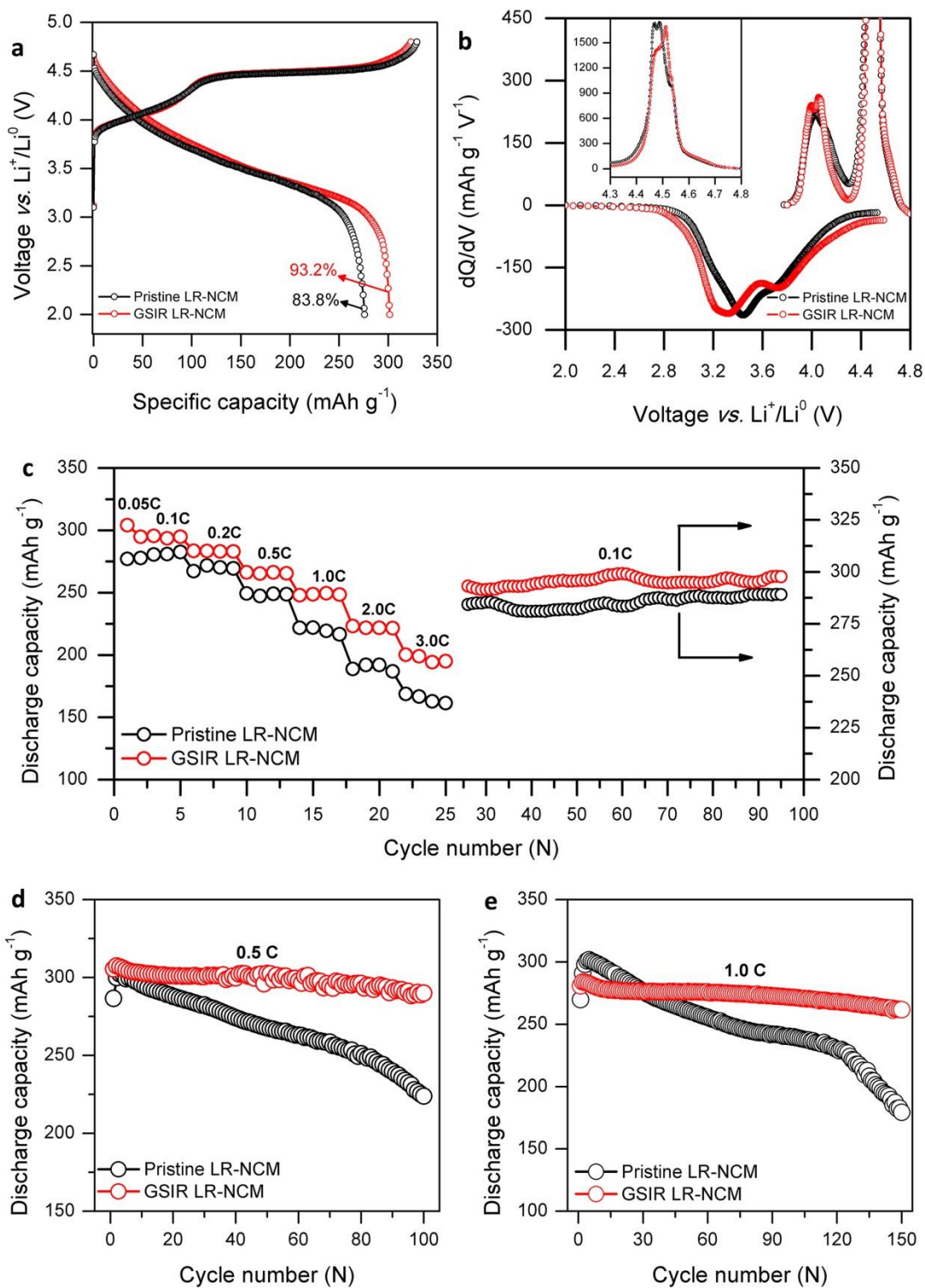
Figure 5.7. Charge-discharge characteristics of the pristine and GSIR LR-NCM.
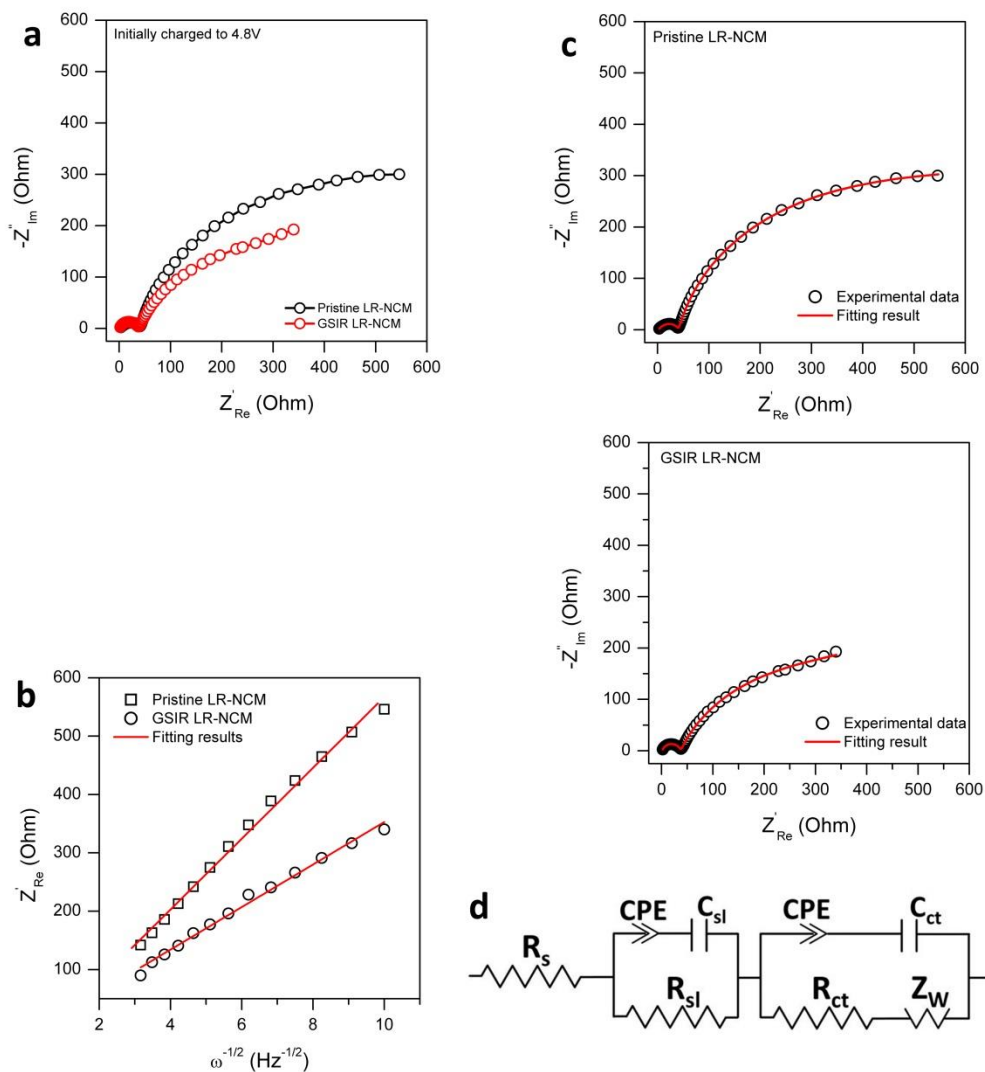
Figure 5.8. Changes of cell impedance for the pristine and GSIR LR-NCM. a. Nyquist plots of the cells with the pristine and GSIR LR-NCM after initially charged to 4.8 V at 0.05 C-rate and rested at 3h; b. The profiles of Z'_{Re} vs. $\omega^{-1/2}$ from 0.1 Hz to 0.01 Hz after initially charged to 4.8 V; c. Typical Nyquist and fitting plots for the pristine and GSIR LR-NCM using the equivalent circuit; d. the equivalent circuit.

Table 5.1. Impedance parameters of the pristine and GSIR LR-NCM after initially charged to 4.8 V.

	R_e (Ω)	R_{sl} (Ω)	R_{ct} (Ω)	σ
Pristine LR-NCM electrode	1.288	37.72	769.2	60.98
GSIR LR-NCM electrode	1.137	36.44	411.7	36.44
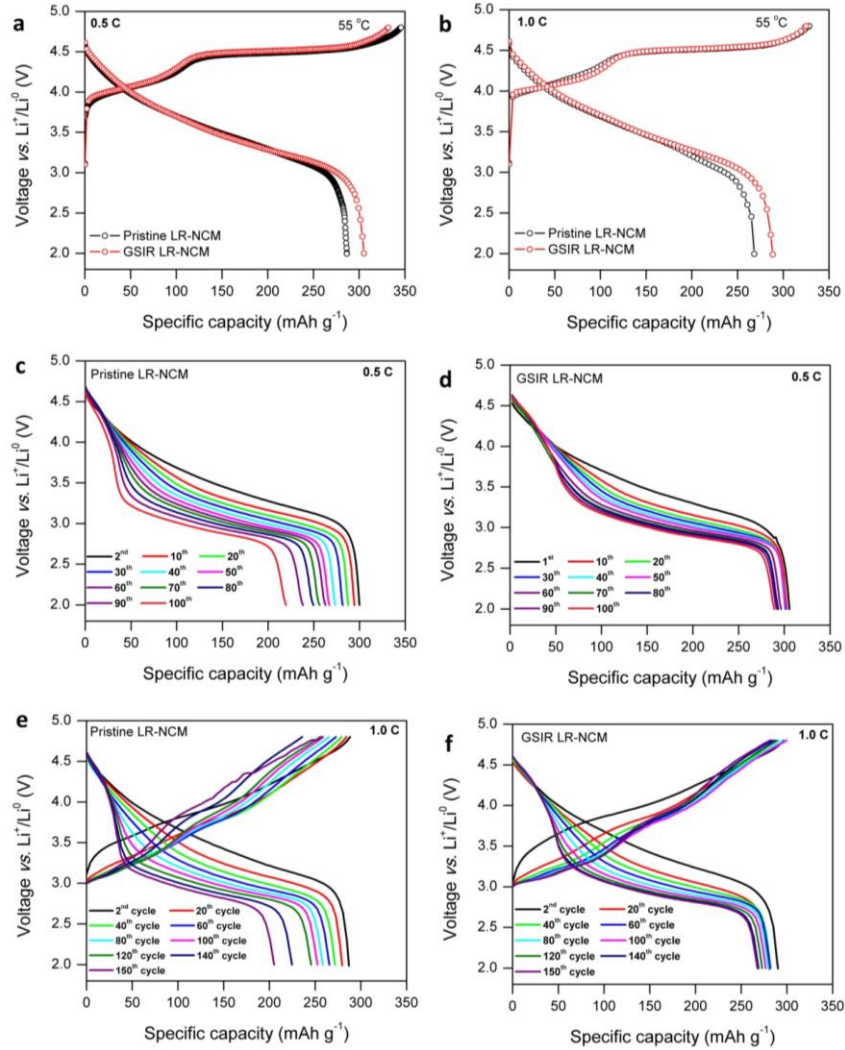
Figure 5.9. Charge-discharge curves of the pristine and GSIR LR-NCM at elevated temperature of 55 ℃.

5.3.3. Discussion of Oxygen Activity Influence on Electrochemical Properties

The influence of surface oxygen vacancies introduced by the GSIR process on the electrochemical performance can be discussed in two aspects: (1) The generation of highly reactive oxygen radicals on the particles' surface during the electrochemical process, which determines the electrochemical resistance at the electrode/electrolyte interface; (2) the participation of the oxygen reaction in the form of O^{2-}/O^- or O_2^{2-} in the bulk of the material, which are the dominant factors in compensating for extra electrons on the superior capacity of Li-rich layered oxides.

Firstly, *operando* differential electrochemical mass spectrometry (DEMS) experiments were conducted to evaluate the gas evolution during the initial charge-discharge process (see Figure 5.10), which is largely related to the activity of oxygen on the particles' surface. Irrespective of the cycling profile, as shown in Figure 5.10b, O_2 is detected near 4.5-4.6 V *vs.* Li^+/Li^0 for both the pristine and GSIR LR-NCM; however, the O_2 gas released from the GSIR LR-NCM electrode is much less than that of the pristine electrode. It is suggested that the formation of oxygen vacancies through GSIR could greatly suppress the evolution of O_2 gas. According to the equation $P_{O_2} = K[V_O^{\cdot\cdot}]^{-6}/16$, less O_2 gas will be released due to the reduced partial pressure of oxygen on the surface of the GSIR LR-NCM electrode after creation of oxygen vacancies. At the same time, the released CO_2 gas for the GSIR LR-NCM (see Figure 5.10c), which is usually considered as the source of decomposition of the electrolyte at high potentials, is slightly smaller than that of the pristine LR-NCM. Therefore, the oxygen vacancies on the surface could hinder the generation of highly reactive oxygen radicals during the electrochemical process.

70
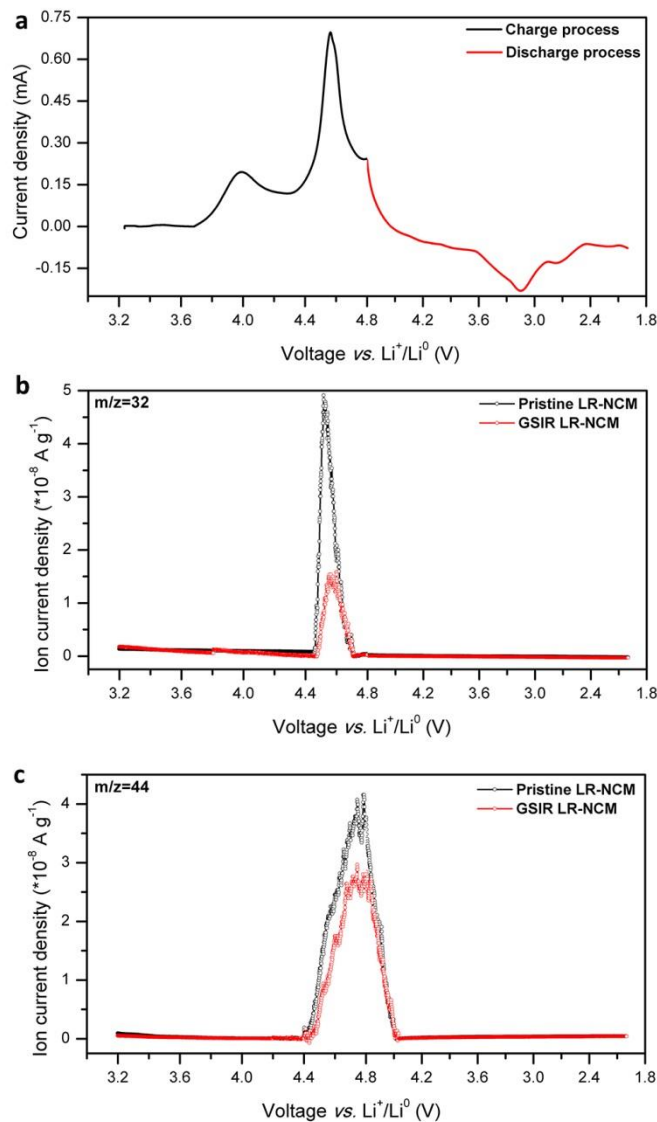
Figure 5.10. Operando differential electrochemical mass spectrometry (DEMS) at elevated temperature. a. Initial cyclic voltammetry (CV) curve of the pristine and GSIR LR-NCM electrode; b. Oxygen gas profile of the initial charge-discharge process for the pristine and GSIR LR-NCM electrode; c. Carbon dioxide gas profile of the initial charge-discharge process as the above electrodes.

Secondly, the GSIR LR-NCM sample exhibits almost the same capacity in the plateau region as in the pristine one with much less oxygen-redox participation on the surface. To compensate for ionic changes during the charge process, more oxygen reactions in the form of

71

O^{2-}/O^- or O^{2-} (instead of the O^{2-}/O_2 redox couple) are triggered in the bulk of the GSIR LR-NCM. The influence of the activities of bulk oxygen in the diffusivity of lithium ions was investigated by first-principles calculations. For simplicity, the super cell was defined as $Li_{28}Ni_6Mn_{14}O_{48}$, which was adopted as a computational model in previous work. A specific $Li_{20/28}$ concentration was chosen to simulate the last stage of discharge (below ~3.2 V), in which the GSIR LR-NCM demonstrates the biggest difference electrochemical performance compared to the pristine LR-NCM. This stage also generally is acknowledged as a rate-determining step of the whole discharge process in Li-rich layered oxides. In this stage, the Li ion migrates from the octahedral site of the Li layer into the octahedral site of the adjacent transition metal layer through an empty tetrahedral site in the former (as shown in Figure 5.11a). When no oxygen vacancy is introduced, the Li tetrahedron site, which is face-sharing with the TM layer Li, is the most stable. There is a high chance of trapping the Li ion in the tetrahedral site (the so-called "Li-Li dumbbell") without diffusing into the adjacent octahedral site in the transition metal layer. These dumbbells finally block the pathways of lithium diffusion, thereby decreasing ionic conductivity. In contrast, when oxygen vacancies are introduced, the under-coordinated site would no longer be stable, and the migration barrier is either zero, or around 170-210 meV, which is quite small. The trapped Li ion will have a higher probability of escaping from the tetrahedral sites, so continuing its diffusion process.
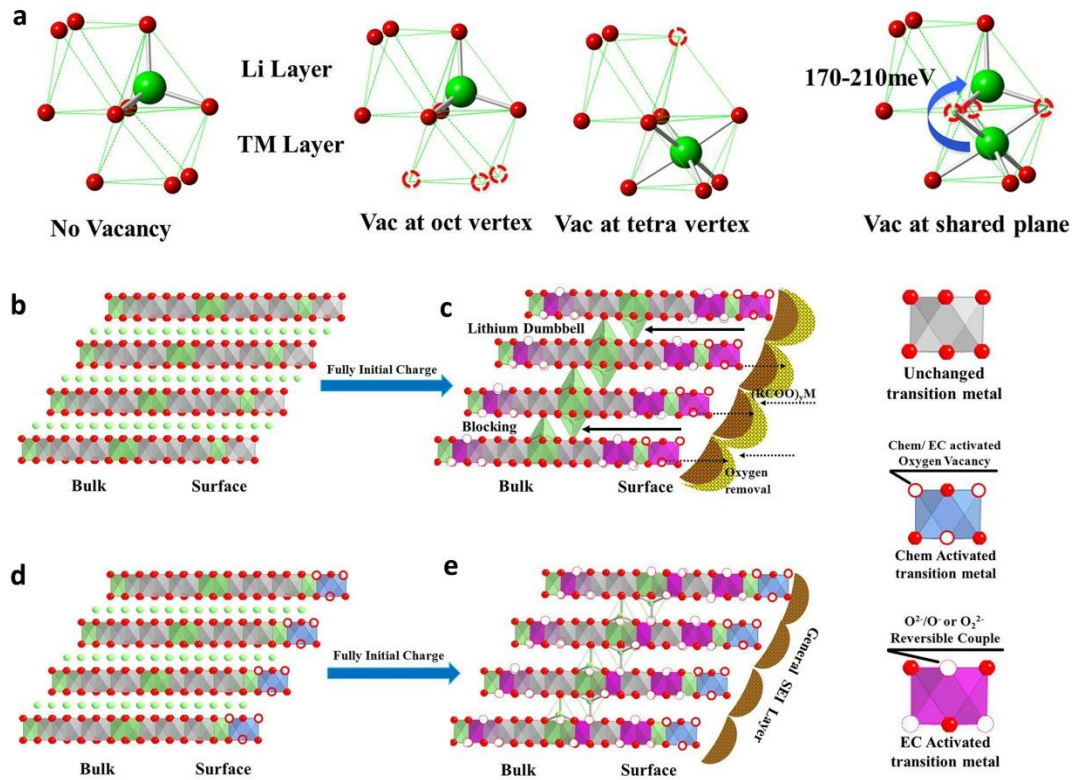
Figure 5.11. Reaction mechanisms during charging and discharging. a. Calculated site stability and activation barrier under conditions of no vacancy, vacancy at octahedron (Oct) vertex, vacancy (Vac) at tetrahedron (Tetra) vertex, and vacancy (Vac) at shared plane. b-c. The pristine LR-NCM before charging and after fully initial charge; d-e. The GSIR LR-NCM before charging and after fully initial charge. Green: Li; Red: O.

Overall, Figure 5.11b-e summarizes the proposed reaction mechanism for pristine- and GSIR-LR-NCM during charging and discharging. Before charging, uniform oxygen and lithium vacancies were created on the particle surface of the GSIR LR-NCM, accompanied by the pre-activation of certain amount of the Li_2MnO_3 component. The sloped region (<4.4 V) of the charging curve is attributed to the extraction of Li^+ ions from the lithium layer. No difference is expected between the pristine material and surface-modified material during this process. During the charging plateau region, more lithium ions can be extracted from the Li_2MnO_3 component, together with the oxidation of lattice oxygen. The pre-activated surface layer of the GSIR sample

with oxygen vacancies reduces the partial pressure of oxygen on the surface, and then prevents gaseous oxygen from evolving during plateau charging. A thinner SEI layer thus is expected to form on the particles' surface of the GSIR LR-NCM due to less side reactions between released oxygen and the electrolyte species, thereby decreasing the electrochemical resistance at the electrode/electrolyte interface, as supported by our EIS results. At the same time, the more reversible oxygen redox-reaction is triggered in the bulk of the GSIR LR-NCM during the high potential charging process. These oxygen vacancies can activate the Li trapped in the tetrahedral sites to provide a favorable environment for Li ion diffusion during the rate-determining step (the last stage of discharging). Higher levels of Li ion diffusivity in the bulk, together with smaller resistance to charge-transfer and larger numbers of activated Mn^{4+}/Mn^{3+} couples lead to higher capacity and better rate- capability of the GSIR LR-NCM. Furthermore, minimal structure changes enable the superior cycling stability after GSIR modification.

5.4. Conclusion

In summary, a novel surface modification route (gas-solid reactivation) has been applied to lithium-rich oxide material. The modified material is able to deliver discharge capacity as high as 306 mAh g^{-1} at room temperature with no obvious voltage degradation profiles after 100 cycles. Multiple characterization methods have been combined to illustrate the functioning mechanism of the gas-solid reactivation. The fundamental contribution of the novel surface modification is the uniform creation of lithium and oxygen vacancies on the surface of particles before electrochemical cycling. Consequently, more Mn^{4+}/Mn^{3+} redox couples in Li_2MnO_3 component are pre-activated; less oxygen gas is released from the material and less oxygen vacancies are created in the bulk during the charging process; limited electrode/electrolyte corrosion and bulk material structure transformation are formed in the battery system. All of

these factors together enable the modified material achieve the electrochemical improvement in both the rate capability and continuous cycle stability. We believe this facile, scalable, and lost cost approach can also be applied to stimulate extensive research on the detail mechanism of the gas-solid interface reactivation process as well as advancing industrial applications.

This chapter in full, is a reprint of the material "Gas–solid Interfacial Modification of Oxygen Activity in Layered Oxide Cathodes for Lithium-ion Batteries" as it appears in the Nature Communications, Qiu, B.; Zhang, M.; Wu, L.; Wang, J.; Xia, Y.; Qian, D.; Liu, H. D.; Hy, S.; Chen, Y.; An, K.; Zhu, Y.; Liu, Z.; Meng, Y. S., 2016, 7, 12108. The dissertation author was the co-primary investigator and co-first author of this paper. All of the tests were performed and analyzed by the author except for the neutron diffraction and STEM-EELS data. Both Qiu and the author designed and analyzed, and wrote the results.

Chapter 6. Structural and Voltage Recovery Driven by Defects Elimination in Li-rich Layered Oxide Cathode

6.1. Introduction

In the last decades, rechargeable lithium-ion batteries (LIBs) have commercially dominated the portable electronics market.[139] Moreover, LIBs are becoming the most promising choices for powering electric vehicles. The energy density and cycling life of state-of-the-art LIBs have to be further improved to meet the performance requirements for transportation applications.[140] However, the relatively low capacity of cathode has become one of the major bottlenecks to achieve higher energy density in LIBs.[141] In principle, the capacity of classical layered transition metal (TM) oxides, the primary commercial cathode materials, is limited to cationic redox activity.[142] Anionic redox has thus emerged as a new paradigm for designing novel cathodes for next generation LIBs. It is recently found and confirmed oxygen redox in lithium-rich layered oxides with composition $xLi_2MnO_3 \cdot (1-x)LiTMO_2$, which enables this group of materials exhibit reversible capacities exceeding 280 mAh g^{-1}.[143]

In order to activate oxygen redox, batteries with lithium-rich layered oxide cathode have to be charged over 4.6 V *vs.* Li^+/Li^0. The activation unfortunately results in irreversible structure transformation in terms of defects formation including lithium and oxygen vacancies, lithium tetrahedron, TM migration, edge dislocations, stacking fault, and local strain.[144-146] Large voltage hysteresis in the initial cycle is one manifestation of the structural irreversible transformation.[147] At the same time, a continuous average voltage decay of batteries also occurs, which is closely correlated to the unceasing defects generation during the extended cycles.[148] Voltage decay that is rooted in structural failure plagues their implementation in practical batteries.

Structural irreversible transformation induced by defects during the initial cycle and its influence on their electrochemical performance have been investigated from different aspects: Oxygen vacancies were found to form near the material surfaces by scanning transmission electron microscopy (STEM) and electron energy loss spectroscopy (EELS); These oxygen vacancies facilitate migration of TM with broken TM-O bonds from the under-coordinated octahedral site of TM layers to the fully-coordinated tetrahedral/octahedral sites in the Li layer;[149] Moreover, lithium local environment changes by formation of lithium "dumbbells" which was predicted by computation to involve tetrahedral sites Li of the lithium layers; The above migrations finally lead to the defect-spinel structure creation on the particle surface; Dislocation network or stacking sequence change was also directly observed in nanoparticles of lithium-rich layered oxide material by Bragg coherent X-ray diffractive imaging (BCDI).[150] All of these inhomogeneities and defects have been correlated with voltage decay through different models and mechanisms.[151]

Modification methods including surface modification, foreign elements doping, etc., have been proposed in the literatures to mitigate the defects formation and maintain the structure ordering.[152, 153] Despite their improvement, the intrinsic voltage fading is still inevitable and remains a challenge that will require considerable effort to overcome.[154] In order to tackle this issue, three key questions need to be answered: (1) is the structure after defects generation energetically stable or metastable? (2) If it's metastable, under what circumstance, defects can be at least partially eliminated so that structure is recovered to a stable state? (3) If the structure can be recovered, will the original working voltage be restored?

In this work, we demonstrate a path to recover the layer structure and working voltage through high-temperature annealing. The treatment at high temperature recovers the local Li-

excess environments around oxygen, oxygen stacking sequence, and eliminates microstrain associated with different defects. As a result, the voltage profile once more shows plateau region during charge and the average discharge voltage is restored of the cycled cathode after heat treatment. Both theoretical calculations and experimental characterizations illustrate the mechanisms underlying the heating induced recovery. The structure metastability and defects removal are decisive in structure and voltage recovery of lithium-rich layered oxide cathode.

6.2. Experimental

6.2.1. Heat Treatment of Cycled Li-rich Layered Cathode

The detailed information was carried out as the same with our previous report. Stoichiometric amounts (4:1:1) of $NiSO_4$ $6H_2O$, $CoSO_4$ $7H_2O$, and $MnSO_4$ $4H_2O$ were dissolved into the water to form a solution with the concentration of 2.0 mol L^{-1}. Then a mixed solution of 2.0 mol L^{-1} Na_2CO_3 solution, and 0.2 mol L^{-1} NH_4OH solution were pumped into a continuously stirred tank reactor (CSTR, capacity of 250 L), separately. The temperature of reactor was kept at 60 ℃, and the pH value of solution was controlled at 7.8. The resulting precipitates were $(Ni_{1/6}Co_{1/6}Mn_{4/6})CO_3$ powders. To remove residual Na^+, they were washed several times with distilled water. Then they were dried in a vacuum oven at 80 ℃ for over 12h. Some amounts of Li_2CO_3 with the molar ratio about 0.7 were mixed with the resulting powders. The mixed powders firstly were treated at 500 ℃ for 5 h in the air, and calcinated at 850 ℃ for 15 h in the air, and cooled to room temperature in the furnace.

18650-typed batteries (18 mm in diameter and 65 mm in height) were assembled as the similar with our previous report.[155] Nominally, it was designed of the capacity of the batteries with 1400 mAh. Li-rich layered $Li[Li_{0.144}Ni_{0.136}Co_{0.136}Mn_{0.544}]O_2$ oxide as cathode, $Li_4Ti_5O_{12}@C$

(BTR, Shenzhen) as anode, and polyethylene as separator were used to fabricate the batteries. The positive electrodes contained 94.5 *wt.* % LR-NCM, 3.0 *wt.* % conductive carbon, and 2.5 *wt.* % PVDF. The mass loading on each side of the electrode was about 10 mg cm^{-2}. The negative electrode contained 90.5 wt. % $Li_4Ti_5O_{12}$@C, 5.0 *wt.* % conductive graphite, and 4.5 *wt.* % PVDF. The mass loading on each side of the electrode was about 16 mg cm^{-2}. Some electrolyte was then injected in an argon filled glove box. LAND-CT2001B battery test systems were used to test the initial charge-discharge and cycle performance of batteries. For the initial charge-discharge process, the experimental batteries in this study were directly charged and discharged under the voltage range from 0.5 V to 3.25 V at 0.1 C. To measure the cycling performance, we used the constant-current constant-voltage (CC-CV) protocol. The detailed procedures were as below: all the batteries were charged and discharged under the voltage of 1.0-3.25 V *vs.* $Li_4Ti_5O_{12}$ at 140 mA (0.1 C), where the batteries were charged with a constant current of 140 mA (0.1 C), followed by holding the voltage at 3.25 V until the current dropped to 70 mA (0.05 C). The fully discharged batteries at 1st, 50th and 100th cycle at 0.1 C-rate were dissembled in a glove box to further measure *in situ* synchrotron X-ray diffraction and *ex situ* neutron diffraction, and electrochemical performance to confirm the structural changes.

6.2.2. Structural Characterizations

Thermogravimetric analysis and differential thermal analysis (DTA, Pyris Diamond, Perkin-Elmer) from room temperature to 400 ℃ at a rate of 2 ℃ min^{-1} was conducted to calculate the weight loss and the phase transitions of the cycled samples under air or nitrogen stream, respectively. A field-emission scanning electron microscopy (FESEM) image was measured on a Hitachi S-4800.

The cycled batteries were transferred to a glove box for disassembly. The cathodes were washed in DMC solvent in the glove box, and the mixed cathode powders (including the binder and conductive carbon) were obtained by scratching away the electrode from the current collector. They were loaded into 1.0 mm diameter corundum capillaries. The capillary then was mounted on the thermal stage of beamline 14B1, at Shanghai Synchrotron Radiation Facility (SSRF). The wavelength used at the 14B1 was 0.6887 Å (18 keV). The detailed information about beamline BL14B1 can be found in their previous literature.[156] To track the structural changes accompanied with the temperature changes, SXRD spectra continuously were recorded as a set of circles on a two-dimensional image plate detector in the transmission mode during heating from room temperature to 400 ℃ (i.e., heating rate = 5 ℃ min^{-1}). The total recording time for one spectrum was approximately 30s.

The cycled powder samples annealed with different temperatures were carried out by the time of flight (TOF) *ex situ* neutron diffraction (ND). The data were collected on the VULCAN beamline at the Spallation Neutron Sources (SNS) in the Oak Ridge National Laboratory (ORNL). The sample was packed into a vanadium can, respectively. An incident beam (5mm by 12mm) was employed with 0.7- to 3.5-Å bandwidth, which allowed a 0.5~2.5 Å d-spacing in the diffracted patterns in the ±90° 2θ detector banks. The double-disk choppers at a speed of 30 Hz were selected. A high- resolution mode was applied with Δd/d ~0.25%. The SNS was at a nominal 1100KW. Powder-neutron-diffraction data were collected at a high-resolution mode for 3 h and reduced by the VDRIVE software. The GSAS programs with the EXPGUI interface was used to perform full-pattern Rietveld refinement.

For *ex-situ* TEM heating experiment, the LR-NCM particles, collected from the electrode after the initial cycle, were dispersed in an organic solvent and dropped onto a carbon-support-

film-coated copper mesh TEM grid. After the initial TEM investigation, the experimented grid was heated at 300 ℃ for 1 h in an air oven with heating rate of 10 ℃/min. After the heating, the grid was cooled down slowly in the oven. The same particles observed during the initial TEM experiment were investigated again by TEM for the comparison. The electron diffraction patterns were obtained from JEOL-ARM 200CF (at Brookhaven National Laboratory) and JEOL-2100F (at Seoul National University) TEM microscope with an acceleration voltage of 200 kV.

6.2.3. Electrochemical Testing

The working electrodes were prepared by a mixture of the pristine or cycled samples, conductive carbon, and polyvinylidene fluoride (PVDF) binder on an aluminum foil; note that the final ratio of the mixtures for the cycled samples was about 80: 10: 10. The final electrode discs was 13 mm in diameter. To remove the residual N-methyl-2-pyrrolidone (NMP) and traces of water, they were dried at 80 ℃ for 12 h in vacuum. Lithium metal was used as the counter and reference electrode. Celgard 2502 was used as the separator, and ethylene carbonate (EC)-dimethyl carbonate (DMC, Zhangjiagang Guotai-Huarong New Chemical Materials Co., Ltd.) with the volume ratio of 3:7 dissolved with 1M $LiPF_6$ was applied as electrolyte solution. The cells were then assembled in an Ar-filled glove box (H_2O < 0.1ppm, and O_2 < 0.1ppm). A LAND-CT2001A battery test system was used to galvanostatically charge and discharge. All the tests were measured at room temperature. The fully discharged cells at the initial cycle were dissembled in a glove box to further measure differential thermal analysis, *in situ* synchrotron X-ray diffraction and *ex situ* transmission electron microscopy for evaluating the thermal properties and structural changes.

81

6.3. Results and Discussion

6.3.1. Investigation of Structural Metastability

The synthesis process of lithium-rich layered oxides $Li[Li_{0.144}Ni_{0.136}Co_{0.136}Mn_{0.544}]O_2$ (denoted as LR-NCM) is described in the Methods Section. Their morphology, and phase purity were examined by scanning electron microscopy (SEM, Figure 6.1a-c), synchrotron X-ray and neutron diffraction (SXRD and ND, Figure 6.1d and e), respectively. All the results are well consistent with our previous report. The typical capacity-voltage profiles of LR-NCM oxide at a current density of 12.5 mA g^{-1} (approximately C/20 rate) are presented in Figure 6.3a. Electrochemical data provides information on the structural energetic and local environment changes with respect to lithium extraction/insertion. It shows the feasibility to remove nearly 95 percent of Li (corresponding to a capacity of 337 mAh g^{-1}) in the structure via a slope and plateau region during the first charge. While only 89 percent of extracted Li (corresponding to a capacity of 299 mAh g^{-1}) could be reinserted by an S-type discharge curve. Compared with the charge, the smaller capacity and lower voltage in the discharge indicates the structure is not fully reversible during the initial cycle and transformed to a higher energy state. It has been well acknowledged that point defects (oxygen vacancies, tetrahedral site lithium, TM in lithium layer, etc.), line defects (dislocations), two-dimensional defects (stacking fault), volume defects (microstrain) form during the initial cycle and lead to irreversible structure transformation. As a consequence, superlattice peak intensity which represents structure long-range ordering in SXRD patterns reduces significantly after the initial cycle (see Figure 6.2). And it should be noted electrode surface impedance development is not a dominating factor accounting for the hysteresis since the second charge average voltage also decreases instead of increasing to compensate the Ohm drop (see Figure 6.3a).
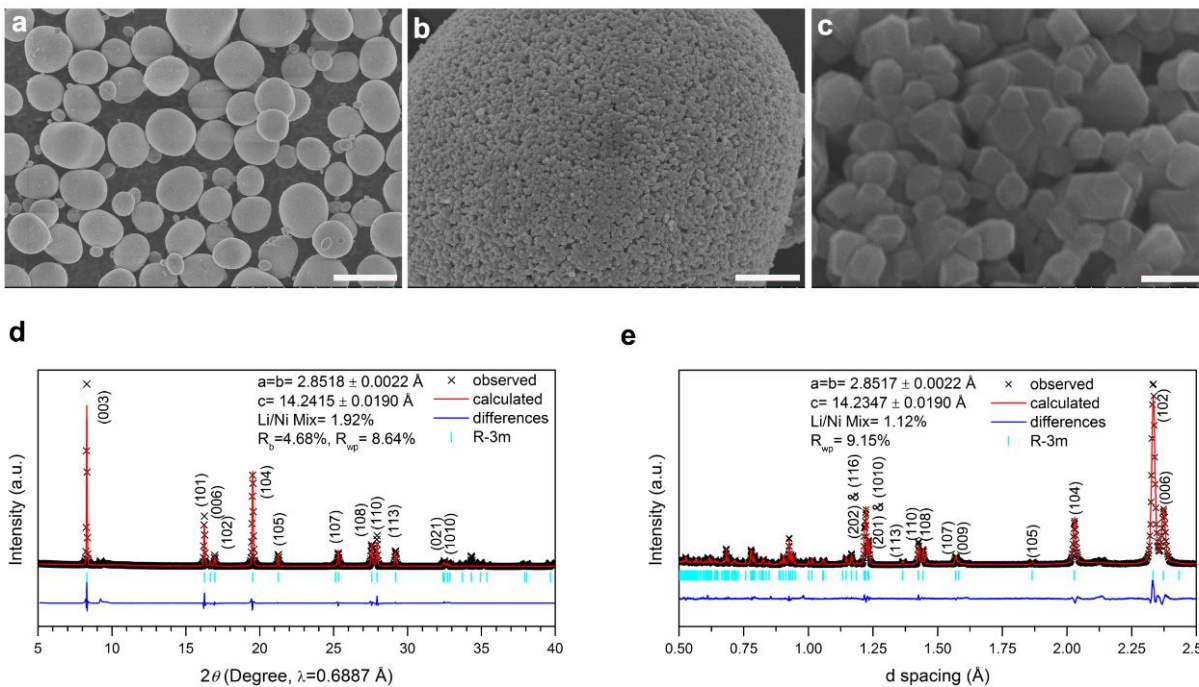
Figure 6.1. Morphology and structure characterizations of the pristine material.
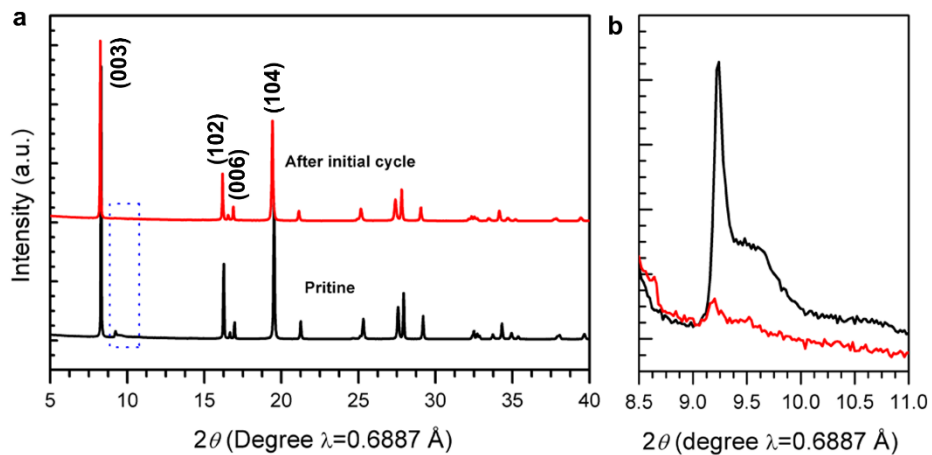
Figure 6.2. Structural characterizations before and after initial cycle.
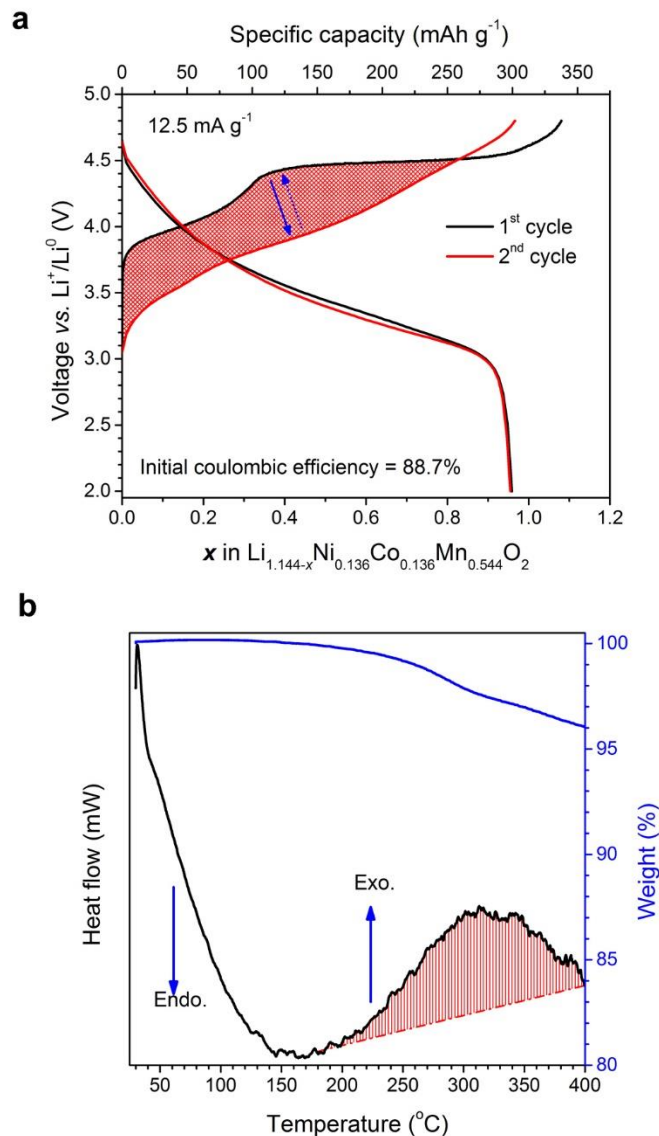
Figure 6.3. Characterization of structural metastability of the initially cycled sample. a. First and second charge-discharge profiles of Li-rich layered Li[Li$_{0.144}$Ni$_{0.136}$Co$_{0.136}$Mn$_{0.544}$]O$_2$ oxides obtained from a 2032-type coin cells at 0.05 C-rate; b. Thermogravimetric analysis and differential thermal analysis (DTA) curves after initial cycle in the air atmosphere.

In general, high concentration defects in the crystal structure will result in thermal instability.[157] To directly investigate whether the cycled material is in a thermodynamically unfavorable state, thermogravimetric (TG) and differential thermal analysis (DTA) were performed on the initially cycled sample (see Figure 6.3b) under air atmosphere. The maximum

temperature in DTA measurement was set to be 400 ℃ to prevent phase transformation from layer-type to spinel or rocksalt-type.[158] Two main reaction regions were found in the whole temperature range: (1) the endothermic process from 30 to 150 ℃ which is corresponding to the decomposition/volatilization of organic compounds or $LiPF_6$ salt formed/left on the electrode surface during the initial cycle; (2) the exothermic process from 150 to 400 ℃ which can be ascribed to the material structure transformation accompanied with the defects elimination. The process in detail will be covered in the Discussion Section. We would like to point out different gas flow in the measurement, air or nitrogen, makes no difference to this transformation (see Figure 6.4a). The weight loss in this process may be primarily attributed to the binder and byproducts decomposition or oxygen loss on the particle surface in the cycled electrode (see Figure 6.4b-c).[158] Considerable heat release was detected in this exothermic process, which implies the material transforms to a lower energy state driven by a temperature higher than 200 ℃ (the onset temperature of the exothermic peak). In other words, the cycled material before heat treatment is in a thermodynamically metastable state.
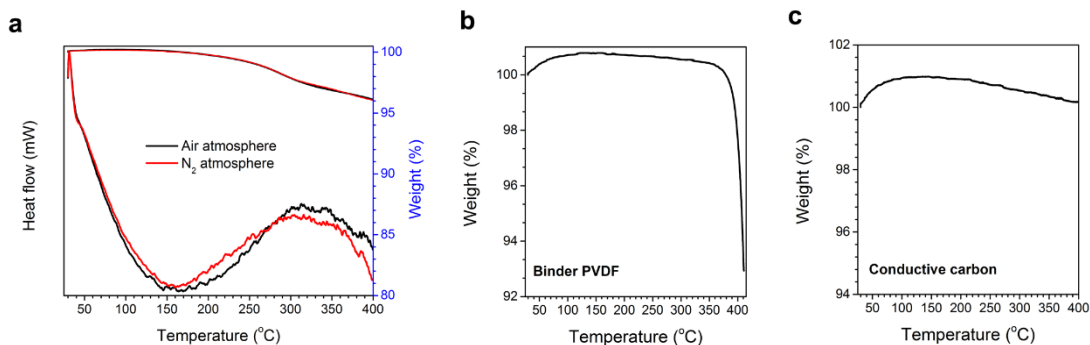
Figure 6.4. Thermal characterization of the initially cycled sample in different atmospheres.

To assess the effect of structure transformation after heat treatment, 18650-type cylindrical full cells were fabricated with LR-NCM cathode and zero-strain spinel $Li_4Ti_5O_{12}$

(LTO) anode. The detailed fabrication procedures are provided in the Methods Section. The initial charge-discharge curve for the full cell (see Figure 6.5a) is almost identical to the profile of the Li half cell in Figure 6.3a. After the initial formation, the full cell was dissembled in the argon-filled glove box. The LR-NCM cathodes were washed, dried, scripted off from the current collector, and annealed in the box furnace at a temperature higher than 150 ℃. Figure 6.5b shows the charge-discharge curves for the cycled LR-NCM material after annealing with different temperature in the voltage range of 4.6-2.0 V. Surprisingly, the plateau region in the charge at approximately 4.5 V $vs.$ Li^+/Li^0 gradually appear with an increase of annealing temperature. The plateau due to the excess Li in TM layer originates from the particular Li–O–Li configuration. As confirmed by $in\ operando$ ND for this group material, very few Li can be intercalated back into the TM layer after being charged at high voltage, which results in the disappearance of the oxygen redox plateau after the initial cycle.[159] The reappearance of the plateau implies Li ions reinsert into TM layer during the annealing process. No obvious reduction peaks changes were found in the differential capacity $vs.$ voltage (dQ/dV) plots (inset in Figure 6.5b), which indicates the original layered phase is preserved after annealing. Although the average discharge voltage shows a similar decay trend at the subsequent cycles (see Figure 6.5c), the starting discharge voltage has an increase from 3.575 V to 3.667 V after annealing. The charge-discharge curves for different samples are presented in Figure 6.6a-d.
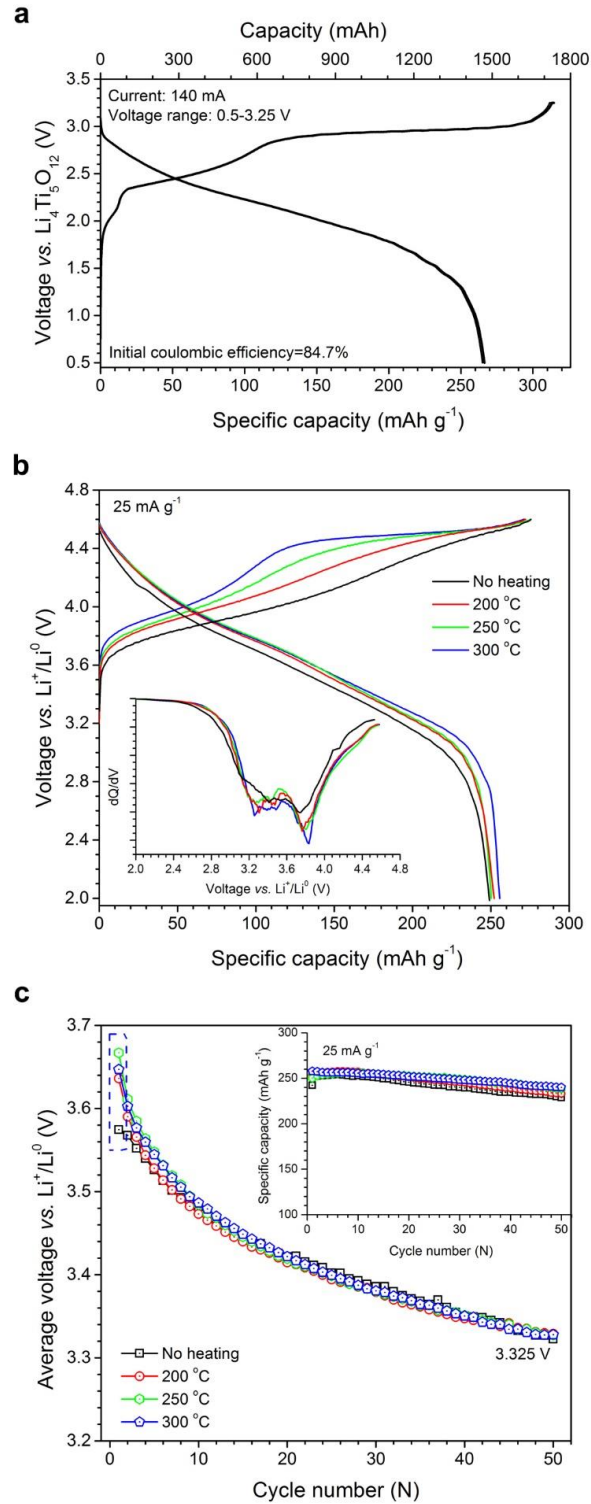
Figure 6.5. Electrochemical measurements to illustrate the structural recovery.
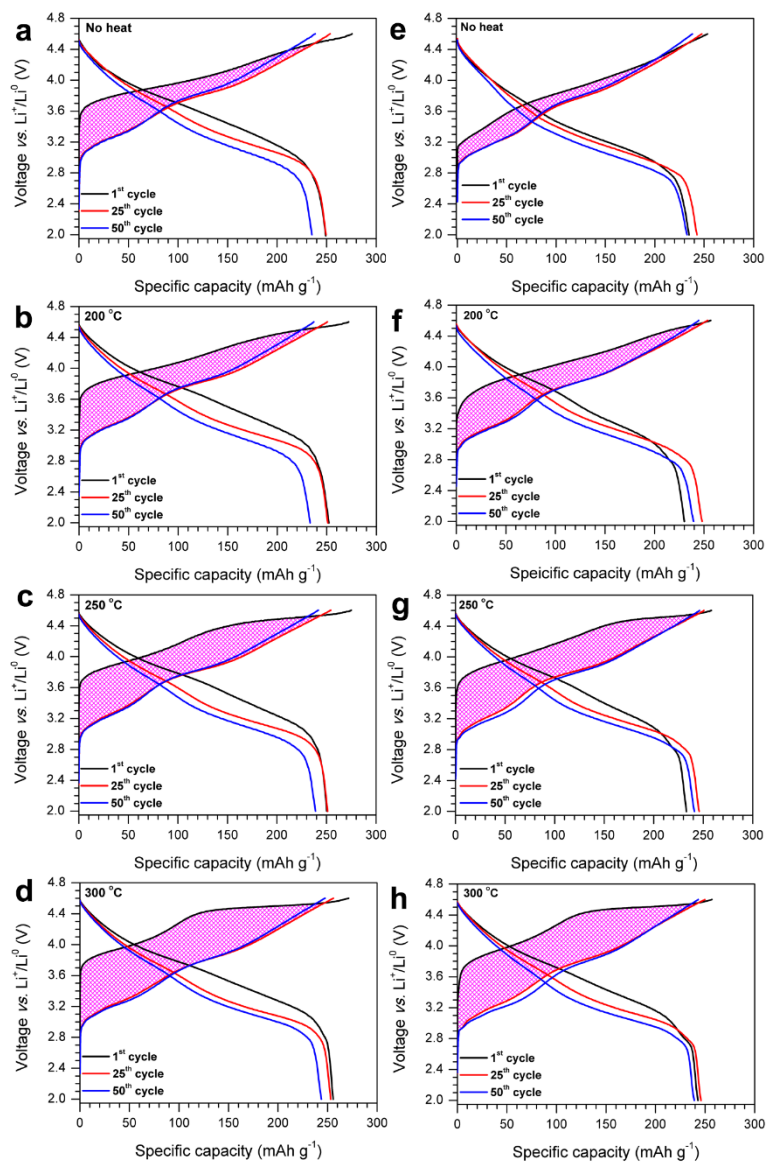
Figure 6.6. Charge-discharge curves at different temperatures. a-d. Charge-charge curves of the samples after the initial formation of LR-NCM/LTO@ full cells annealed with different temperatures. e-h. Charge-charge curves of the samples after 50 cycles of LR-NCM/LTO@ full cells annealed with different temperatures.

6.3.2. Structural Recovery

To investigate the influence of heat treatment on lithium and oxygen migration, ND was conducted on the samples annealed with different temperature. The as-collected time-of-flight (TOF) ND patterns with 'Rietveld' refinement for different samples (patterns refined with a solid solution of 'R-3m' symmetry) are shown in Figure 6.7. The lattice parameters of the LR-NCM sample after initial cycle are $a = 2.8630(1)$ Å, and $c = 14.3497(9)$ Å. In comparison, both a and c lattice parameters are reduced after annealing under different temperature. This trend counteracts common effect of material thermal expansion, which indicates structure transformation occurs with lattice contraction. Lithium occupancy in TM layer and oxygen occupancy are also shown in Figure 6.8a and b. After initial cycle, lithium from the TM layer is largely irreversible with only 32% of lithium reinsertion. Oxygen vacancies are also observed in the cycled sample, which results in a large fraction of under-coordinated TM ions. These unstable TM ions can potentially migrate to the fully coordinated octahedral sites nearby. Irreversible lithium insertion together with TM ions migration dramatically alters the cation ordering in the TM layer and thus leads to the structure disorder. Interestingly, for the cycled sample after heat treatment, it is found Li occupancy in the TM layer increases with the raise of temperature, which is a strong indication of structure ordering recovery. The elimination of lithium vacancies in the TM layer also recovers local Li-excess environments around oxygen, which is crucial for charge voltage plateau reappearance. On the other hand, the number of oxygen vacancies has no obvious change within the error range during the heat treatment. This result does not exclude the possibility of oxygen vacancies local migration which can facilitate lithium reinsertion to TM layer.
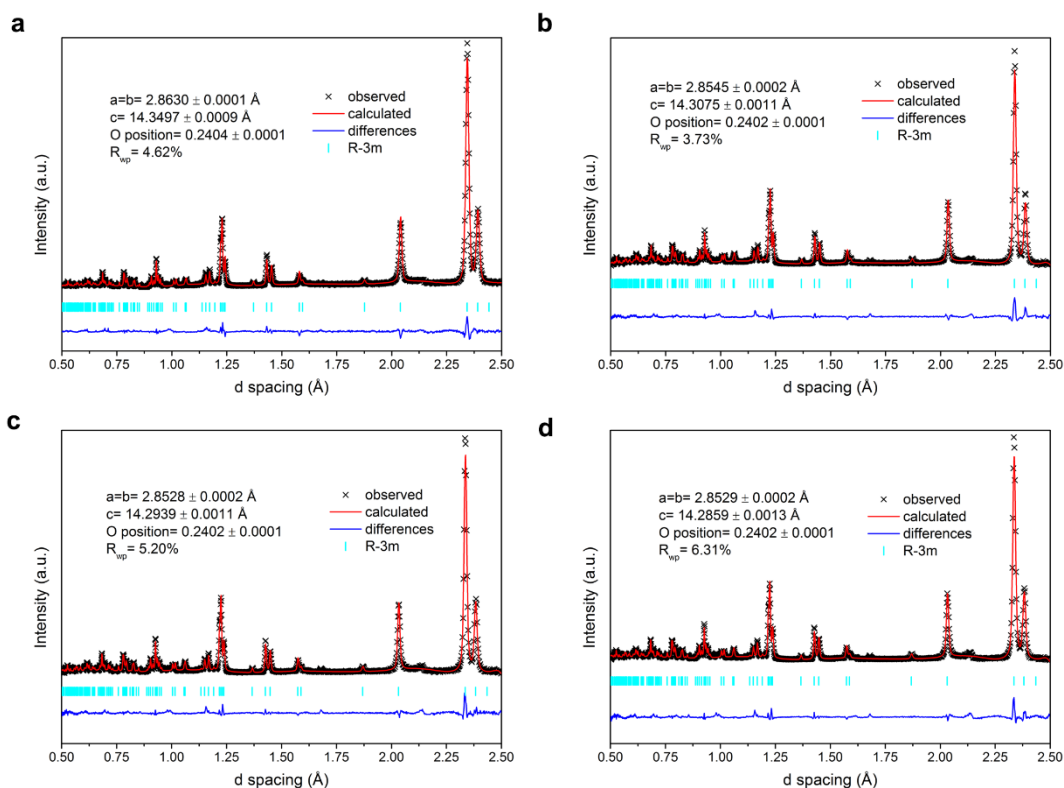
Figure 6.7. Refined neutron diffraction of the initially cycled sample annealed with different temperatures.

Detail bulk structural changes after heat treatment were characterized by (S)TEM. As shown in Figure 6.9, stacking faults were observed for the pristine sample, also seen by Bareno *et al*.[160] Fairly intense diffraction streaks arising from the stacking faults were also recorded in electron diffraction (ED) patterns in Figure 6.8c. After the initial cycle, atomic displacements in and across transition-metal layers are more serious so that atomic resolution imaging can be hardly achieved (see Figure 6.9). Correspondingly, the diffraction streaks in ED pattern are more diffused, which indicates less ordering in the layers stacking direction. After heat treatment at 300 ℃ for one hour, the bulk structure still maintains the layer phase although the surface is transformed to a spinel-type structure (see Figure 6.9). More importantly, the streaks intensity in

90

ED pattern increases. To show the changes clearly for the three samples, the diffraction streaks intensity were quantified from line-scanning with position presented by red arrows in Figure 6.8c. The peaks are more noticeable after the heat treatment compared with the sample after initial cycle (see Figure 6.8d). This observation can be well explained by the ED simulation result using Single Crystal for LR-NCM material with different concentration of stacking faults (see Figure 6.10). We assumed stacking faults were allowed only in between the −O−TM−O−Li− slabs and could never be generated inside the slabs. The ED analysis implies the stacking faults generated in the bulk structure during the electrochemical cycling can be partially eliminated by the heat treatment. The structure ordering along the layers stacking direction is partially restored, which is closely correlated with the intensity changes of superlattice peaks in XRD patterns.
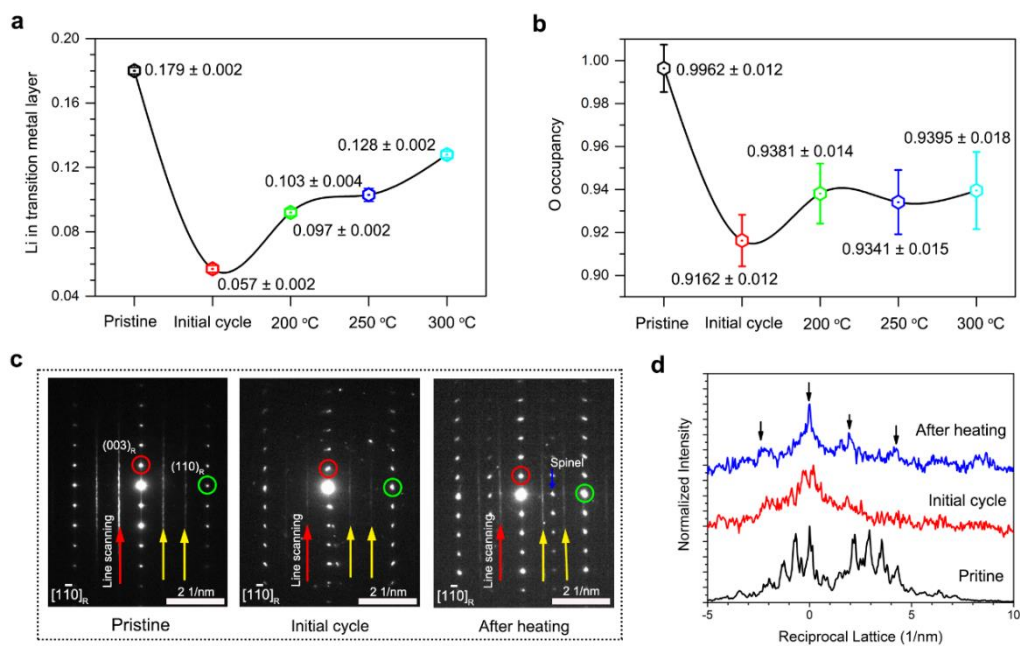
Figure 6.8. Characterizations of structural recovery of the initially cycled sample.
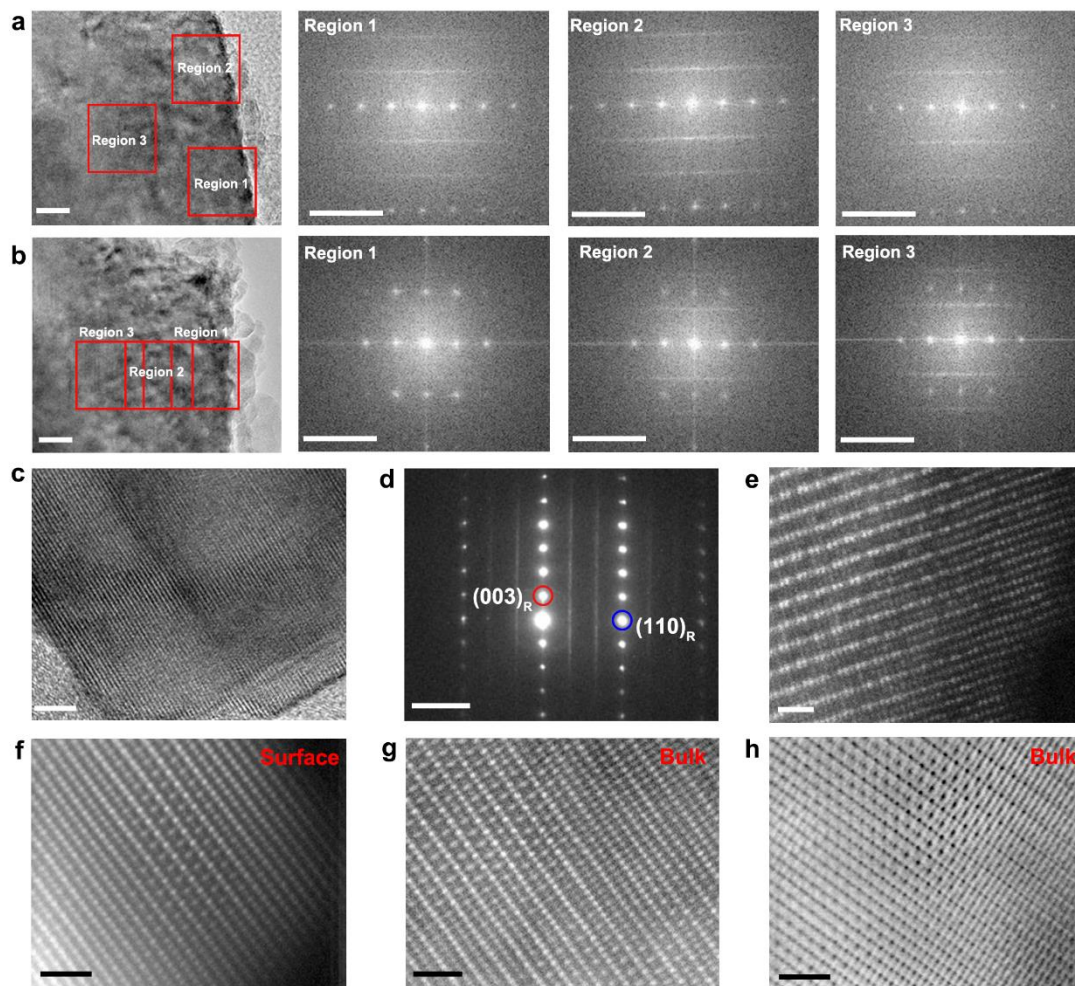
Figure 6.9. a. Bright transmission electron microscopy (TEM) image and fast Fourier transformation (FFT) images with different regions for the initially cycled sample. b. Bright TEM image and fast Fourier transformation (FFT) images with different regions for the initially cycled sample heated at 300 °C. c. HRTEM image at the surface for the initially cycled sample. d. Electron diffraction for the initially cycled sample. e. HAADF-STEM image within the bulk for the initially cycled sample. f. HAADF-STEM image at the surface for the initially cycled sample heated at 300 °C. g. HAADF-STEM images within the bulk for the initially cycled sample heated at 300 °C. h. ABF-STEM image within the bulk for the initially cycled sample heated at 300 °C.
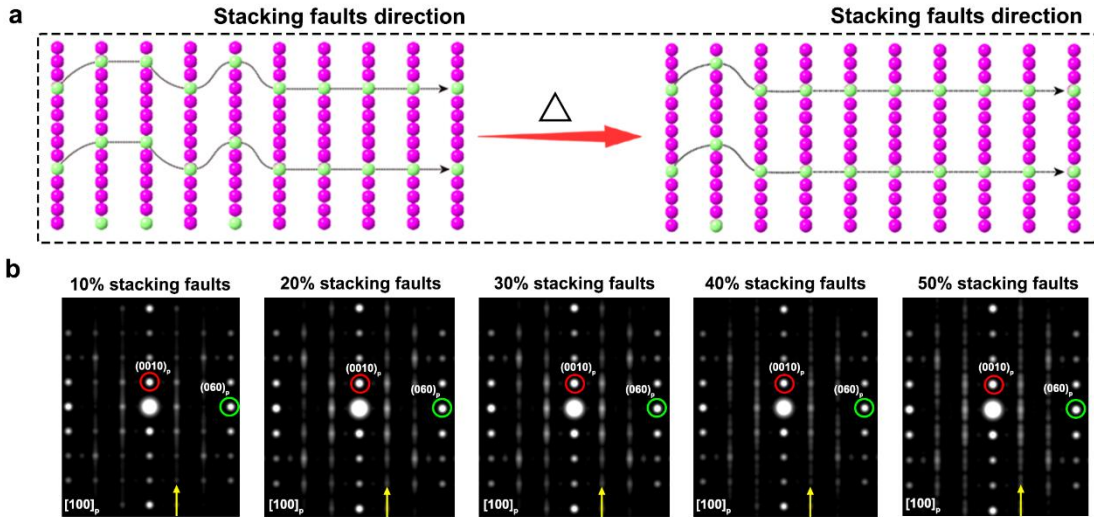
Figure 6.10. Simulations of different degree of stacking faults. a. Models of different degree of stacking fault for Li-rich layered oxide after electrochemical cycling and heat treatment. b. Simulated electron diffraction for Li-rich layered oxide with different degree of stacking faults.

Temperature-controlled *in situ* SXRD was then applied to reveal the superlattice peak changes during the heat treatment for the cycled sample. Figure 6.11a shows SXRD patterns of the initially cycled sample collected in the temperature range between 25 and 400 °C in the absence of the electrolyte, where no phase transition was noted. As expected, the intensity of the superlattice peak at $2\theta = 9.3^{o}$ gradually reappears with the raise of temperature (see Figure 6.11b). The reappearance of the superlattice peak can be ascribed to the lithium ion reinsertion to the TM layer and elimination of stacking faults driven by heat treatment, as revealed by ND and TEM/ED results. The bulk structure is reordered due to the removal of these defects. Full width at half maximum (FWHM) of (003) peak which represents the disordering degree in and across the layers has an obvious decrease with the temperature increasing (see Figure 6.11c). All the characterization results demonstrate the metastable structure of the cycled material is almost restored to the original pristine state with a lower energy after heat treatment.
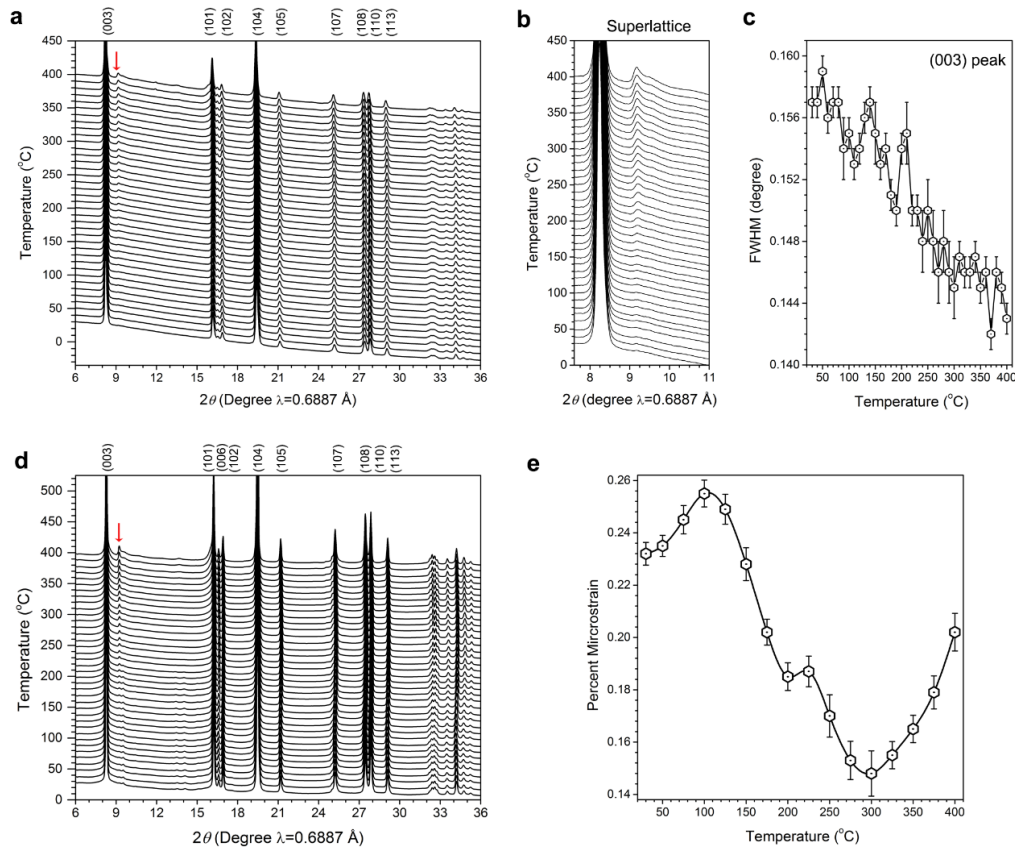
Figure 6.11. Characterizations of structural recovery of the cycled sample. a. *In situ* time-resolved synchrotron X-ray diffraction (TD-SXRD) of the samples after initial cycle. b. Enlarged TD-SXRD patterns related to the in-plane superlattice ordering of lithium and transition metals are shown in the *2θ* ranges of 7.5-11°. c. Changes of full width at half maximum (FWHM) calculated by the intensity of (003) peak in (a) during the heating process. d. *In situ* TD-SXRD of the samples after 50 cycles. e. Changes of percent microstrain calculated by the whole patterns in (d) during the heating process.

In order to verify the heat treatment method to recover the structure that is also effective for the material after extended cycles, *in situ* SXRD was also performed for the samples after 50 cycles in the same temperature range (see Figure 6.11d). The same phenomenon is confirmed based on the reappearance of the superlattice peak. After long cycles, different types of defects continuously form in the bulk structure, which results in high concentration of strain residue in the material. Evidence for microstrain changes during the heat treatment can be extracted by

94

examining line broadening observed in the SXRD patterns through the Williamson–Hall method.[161] As shown in Figure 6.11e, the microstrain gradually increases when the cycled samples heated from room temperature to 125 ℃ due to the thermal expansion. After the heating temperature is higher than 150 ℃, the microstrain suddenly decreases and reaches to its minimum value at a temperature around 300 ℃. The strain release is originated from the defects elimination. And the temperature region for the strain release corresponds well to the exothermic region in the DTA test, which once more manifests heat treatment is an effective method to drive the structure downhill to a more stable state by defects removal.

6.3.3.   Voltage Recovery

Structural recovery sheds light on voltage recovery for the sample after long term cycling. Figure 6.12a shows the cycling performance and average voltage of the LR-NCM/LTO full cell for 50 cycles. No obvious capacity fade is found indicating no decrease of available lithium extraction/insertion sites. At the same time, the average voltage has a continuous decrease during the 50 cycles, which results from different lithium sites local environment due to irreversible structure transformation. Figure 6.12b shows the charge-discharge curves for the cycled LR-NCM material after annealing with different temperature in the voltage range of 2.0-4.6 V *vs.* Li^+/Li^0. With the raise of annealing temperature, not only the charge plateau region reappears, but also the reduction peak in the *dQ/dV* plots (inset in Figure 6.12b) has an obvious shift towards higher voltage. The average discharge voltage thus has a great increase from 3.370 V to 3.628 V (see Figure 6.12c). The discharge capacity has a slight improvement at the beginning and shows a better retention at the subsequent cycles. As shown in Figure 6.12d, the first electrochemical cycle after heat treatment is almost identical no matter the electrode is cycled once or 50 times previously (see Figure 6.13). The difference for the discharge curve can result

from spinel-type phase formation on the surface. Compared with the sample without heat treatment, although the average discharge voltage retention is similar for the subsequent cycles, the actual discharge voltage is much higher at every single cycle. That is to say, voltage decay is inevitable in the electrochemical cycling process for LR-NCM material and heat treatment provides a possible path to recover the voltage after long-term cycling.
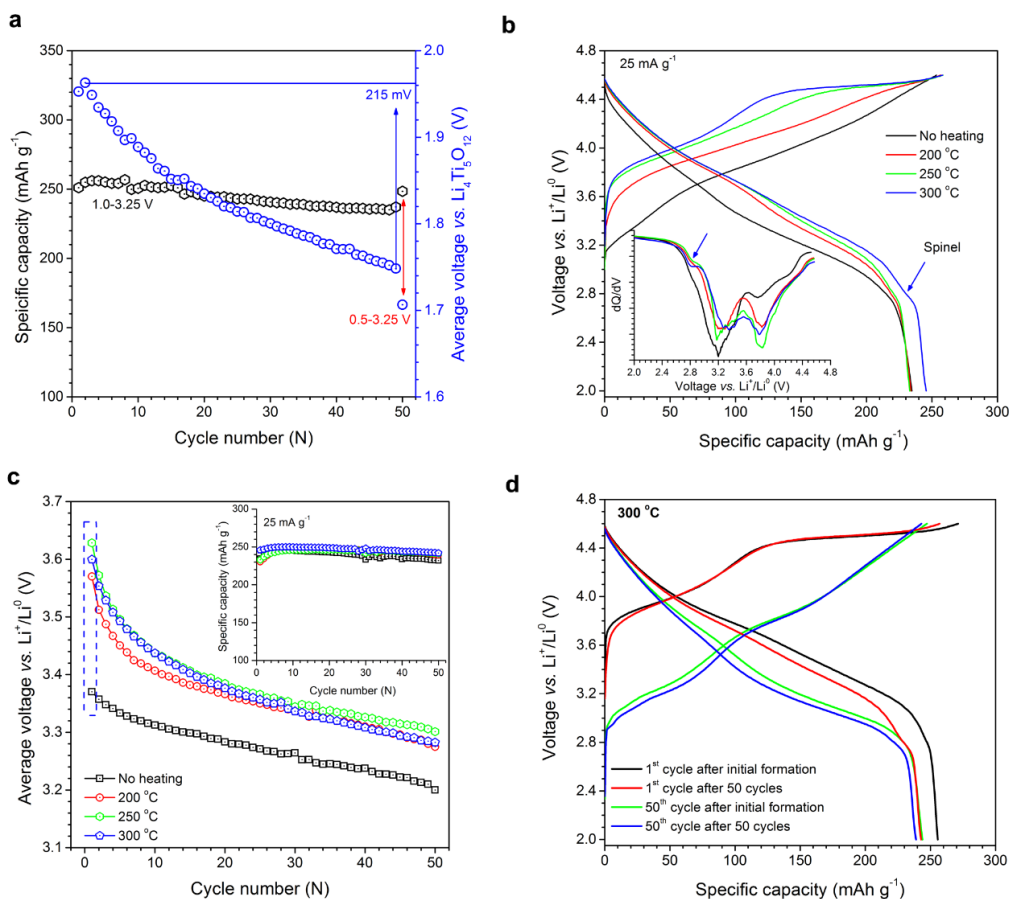
Figure 6.12. Characterizations of voltage recovery of the long cycled sample. a. Cycling performance and average voltage of 18650-typed LR-NCM/LTO@C full batteries, where the cell was cycled under the voltage range of 1.0-3.25 V *vs.* LTO at 0.1 C at room temperature. b. Initial charge-discharge curves with metal Li as anodes under the voltage rang of 2.0-4.6V *vs.* Li^+/Li^0 annealing with different temperatures with the full cells after 50 cycles based on (a). c. Discharge average voltage annealing with different temperatures after 50 cycles of the full cells based on (a). d. The 1st and 50th charge-discharge curves of the samples heated at 300 °C after initial formation and 50 cycles with 18650-typed LR-NCM/LTO@C full batteries, respectively.

96
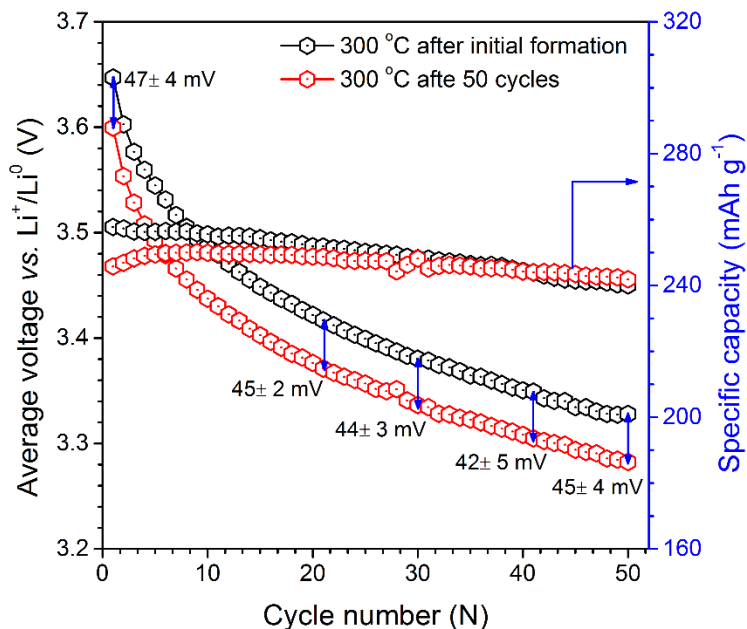
Figure 6.13. Comparisons with electrochemical performance at different cycles. Cycling performance and average voltage for the samples heated at 300 °C after initial formation and 50 cycles with 18650-typed LR-NCM/LTO@C full batteries, respectively.

6.3.4. Discussion of Voltage Recovery Driven by Defects Elimination

The data presented above demonstrates different types of defects are generated in the structure of LR-NCM material during electrochemical cycling. And the cycled material is in a relatively higher energy state which can be considered as metastable. These phenomena are a general characteristic of this group of material and are independent of both synthesis and composition. At this point, we are still left with one important issue that is the correlation among defects generation, structure metastability, and voltage decay. The influence of defects generation on the structure metastability and voltage decay can be discussed in two aspects.

Firstly, the energy of the system increases with the addition of the lithium vacancies in TM layer, given that total lithium concentration in the structure keeps constant. First-principles calculations were applied to estimate the system energy using a supercell with composition

97

$Li_{14}Ni_3Mn_7O_{24}$. In this model, there are two ''excess'' Li ions located in the TM layer. A specific $Li_{12/14}$ concentration was chosen to simulate the cycled state, in which around 1/7 of Li ions are absent in the structure. Three different configurations were tested with zero, one, or two Li vacancies in TM layer. Compared with no vacancies in TM layer, the Gibbs free energy per unit cell increases by ~1 eV when locating both vacancies in TM layer. As confirmed by our previous results, Li ions can easily relax to the tetrahedral site during electrochemical cycling, gradually blocking the pathways of lithium diffusion into the adjacent octahedral site in TM layer. Therefore, the system Gibbs free energy rises up along the electrochemical process as indicated by the black arrows in Figure 6.14a.

Secondly, the energy of the system increases with oxygen stacking sequence changes from ABCABC (O3 notation introduced by Delmas *et al.*[162]) to ABAB (O1 notation). According to Radin *et al.*, transformations between O3 and O1 are easily accomplished via gliding of the MO_2 layers.[163] It is also recently proposed the stacking sequence perturbation mechanism through dislocation network formation. The influence of the oxygen stacking sequence on the system energy in LR-NCM material was investigated by first-principles calculations. For simplicity, a supercell model composed of three-formula units of $Li_{12}Mn_6O_{18}$ was used for LR-NCM structure with different oxygen stacking sequence O3 and O1 (see Figure 6.14c). The Gibbs free energy for O1 stacking is higher than that of O3 stacking for all tested delithiation compositions (see Figure 6.15), confirming O3 stacking is the stable structure without face sharing sites between Li and TM octahedra. Both lithium vacancies in TM layer and stacking sequence fault raise the system energy, creating metastable state of the cycled material. This energy difference is greater at high lithium concentration simply because more coulombic repulsion between Li-Li and Li-TM cations. Note that the slope of the Gibbs free energy as a

function of lithium concentration is a rough estimate for the average voltage. This results in a smaller average voltage for the structure with more defects. It is also confirmed the percent microstrain gradually increases during the extended cycles (see Figure 6.14d), which is arouse by continuous defects generation during the electrochemical cycle. Therefore, voltage decay during cycling process is significantly dominated by defects formation in the structure.
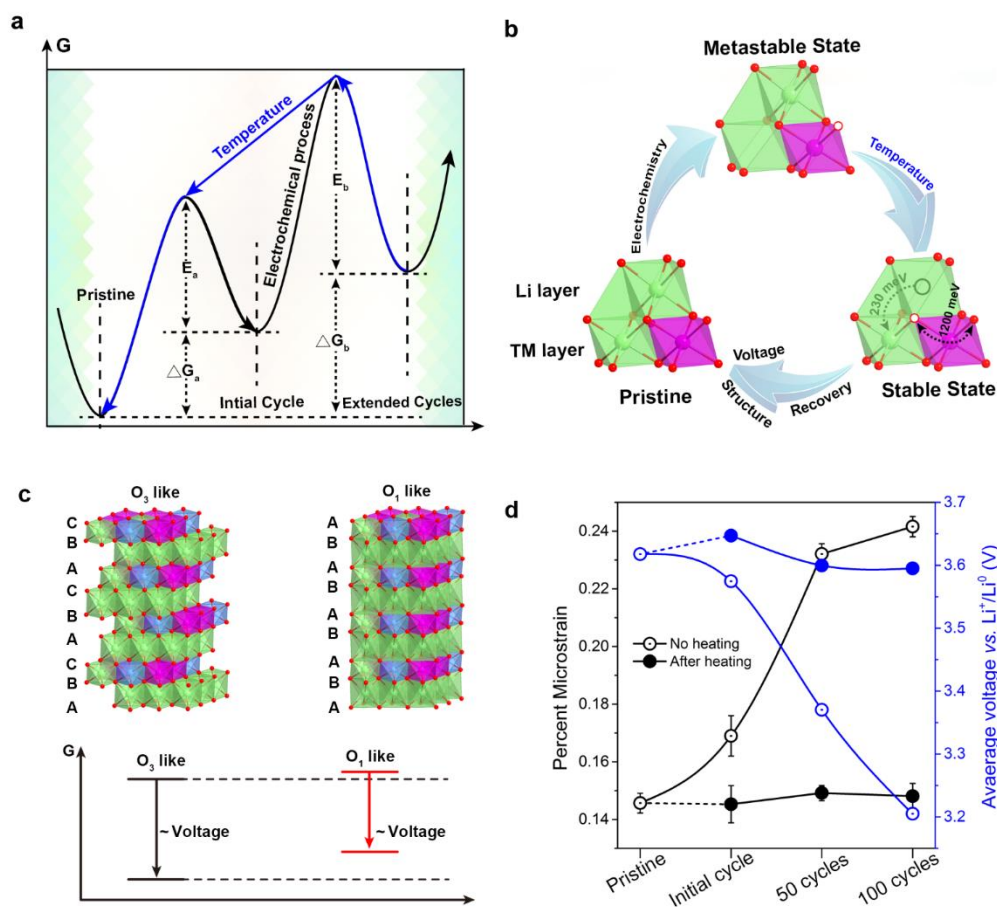
Figure 6.14. Correlations between structural and voltage recovery and defects ordering.
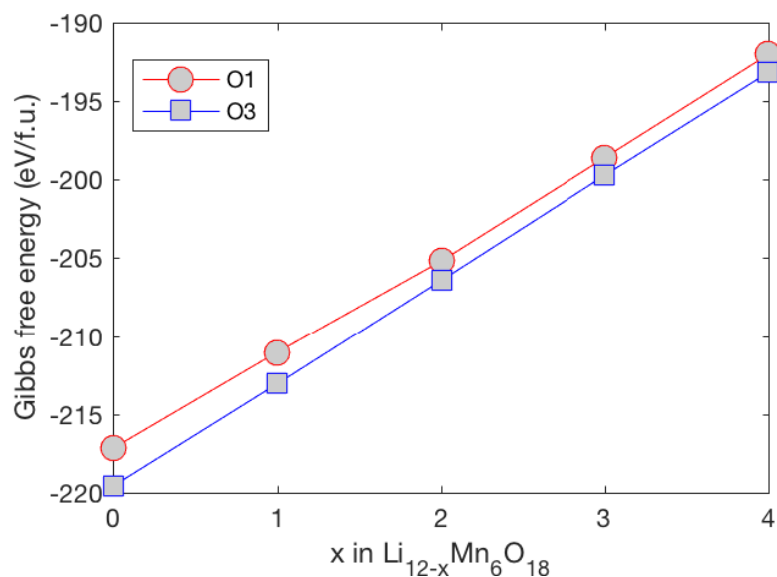
Figure 6.15. The Gibbs free energy for each delithiation composition of the supercell with O3 and O1 stacking.

The cycled state is considered as metastable state not only because of the relatively higher energy, but also the large energy barrier towards the stable state (as labeled by E_a and E_b in Figure 6.14a) that system cannot easily overcome by automatic relaxation process. For example, in the calculation model $Li_{14}Ni_3Mn_7O_{24}$ for metastable state (cycled state), oxygen vacant site is not directly coordinated to the lithium vacancy in TM layer for the structure with the lowest Gibbs free energy (see Figure 6.14b). As confirmed by our previous calculations, Li tetrahedron site, which is face-sharing with the Li vacancy in TM layer, is most stable. Li ion will be trapped in the tetrahedral site without diffusing into the adjacent octahedral site in TM layer. If the oxygen vacancy can migrate to the shared plane between the tetrahedral site and the octahedral site, the under-coordinated tetrahedral site is no longer stable, and the migration barrier is only around 230 meV. To verify the possibility of this oxygen local migration, nudged elastic band (NEB) method was used to find the vacancy migration barrier.[164] Five images between the initial and the final states were taken in the simulation. The calculated oxygen local

100

diffusion barrier is as high as 1200 meV, which makes the oxygen vacancy migration process nearly impossible to occur at room temperature. According to Boltzman relationship, the rate of hops in the migration paths were obtained by:

$$v = v_0 \exp(\frac{-E_b}{k_B T})$$ (eq 6.1)

Where v_0 is an attempt frequency. For the considered migration process, 1200 meV migration barrier at 300 ℃ is equivalent to 600 meV at room temperature, which can be activated under high temperature annealing. This high temperature activation process is universal in solid oxide fuel cell in which the oxygen conductor has a typical migration barrier around 1000 meV.[165]

Heat treatment thus serves as a driving force to enable the system metastable state cross over the energy barrier to relax to the most stable state indicated by the blue arrows in Figure 6.14a. The energy reduction from the metastable state to stable state is released as heat detected in DTA measurement. In addition, high temperature annealing is also considered as effective way to alter the physical properties of a material by dislocations reduction, local strain release.[166] The percent microstrain for the LR-NCM samples after different cycles with heat treatment was also analyzed from SXRD pattern. As predicted, the microstrain is reduced to almost the same minimum value after heat treatment no matter how long the samples have been cycled (see Figure 6.14d). Therefore, the discharge average voltage is recovered with the decrease of microstrain.

6.4. Conclusion

Here, we reveal Li-rich layered oxide structural metastability and reversibility on the cycled materials through differential thermal analysis, *in situ* synchrotron X-ray diffraction, and *ex situ* transmission electron microscopy as well as neutron diffraction on heating. It is proposed that the unique metastable and reversible structures after transformation are essentially correlated with the degree of stacking faults and the ordering of superlattice structure accompanying with Li ions migration into and oxygen vacancies mobility in the transition metal layer. The finding provides new insights that the voltage fade in lithium-rich layered oxides is reversible and searches for new methods to suppress the voltage decay for high-energy-density Li-ion batteries.

This chapter in full, is currently being prepared for submission for publication "Structural and Voltage Recovery Driven by Defects Elimination in Li-rich Layered Oxide Cathode", Qiu, B.; Zhang, M.; Liu, H. D.; Wynn, T. A.; Xia, Y.; Liu, Z.; Meng, Y. S. The dissertation author was the co-primary investigator and co-first author of this paper. All of the experiment parts were performed and analyzed by the author except for the neutron diffraction and electrochemical measurement. Both Qiu and the author designed and analyzed, and wrote the results.

Chapter 7. Investigation of Anatase-TiO$_2$ as an Efficient Electrode Material for MIBs

7.1. Introduction

The advent of lithium-ion electrochemical has ushered in an era of high energy density rechargeable batteries, with applications ranging from portable electronics to electric vehicles.[167-169] However, several challenges have stymied the implementation of ultra-high capacity and energy dense lithium-ion batteries. These issues are largely associated with the use of a lithium-metal anode, which under extensive cycling conditions and current densities promotes the formation of dendritic lithium deposits. Lithium metal dendrites produce electrochemically "dead" lithium, thereby resulting in poor cycling efficiency.[170] In addition, dendritic lithium has been implicated in the cell shorting and thermal runaway. To mitigate such problems, alternative energy storage systems have been heavily pursued, with efforts largely focused on the development of sodium-ion and magnesium-ion electrochemical cells.[171]

The commercial use of a magnesium metal anode is significantly more advantageous over a comparable lithium metal anode, as the volumetric capacity is nearly double (3833 mAh mL^{-1} vs. 2062 mAh mL^{-1}, respectively) and the deposition morphology has been described as non-dendritic.[172] In addition, magnesium is much more abundant in the Earth's crust in addition to being more stable in both humid and oxygen-rich environments. As such, considerable attention has been focused the development of magnesium electrochemical cells utilizing a magnesium metal anode, high capacity cathode, and suitable electrolyte.[173] However, most conventional electrolyte solutions may not be applicable for magnesium batteries due to a high polarizing nature of the divalent Mg^{2+} cation.[174] So far, studies of magnesium batteries have been limited to either Mg(AlCl$_2$EtBu)$_2$/THF or (PhMgCl)$_2$–AlCl$_3$/THF APC ("all phenyl" complex)

electrolyte systems.[175] The APC electrolyte has been more widely applied due to its highly reversible Mg deposition capability, lower overpotential, and wider electrochemical windows.

Another threshold factor to realize the application of MIBs is the choice of cathode with relatively stable electrochemical performances. The leading cathode material is the Chevrel-phase Mo_6S_8, was introduced in 2000 with an experimentally determined specific capacity of 105 mAh g^{-1}. Nowadays, various cathode materials such as transition metal oxides (V_2O_5, RuO_2, MnO_2, Co_3O_4), have been used successfully to achieve the reversible insertion and extraction of Mg cation.[66-70] However, these cathodes suffer from sluggish kinetics of Mg^{2+} ion diffusion through the structure due to the strong electrostatic effect of the divalent Mg cation.

Anatase TiO_2, a typical lithium intercalation electrode, is considered to be a magnesium battery cathode candidate.[176] A prototype system for magnesium/anatase TiO_2 has been reported by Sheha et al.[177] The discharge capacity is found insufficient for various applications. Wang and co-workers greatly improved magnesium insertion ability of anatase TiO_2 by employing $LiBH_4$ in $Mg(BH_4)_2$/tetraglyme electrolyte.[178] This electrolyte has large concentration of lithium salt. In order to prevent the lithium insertion interference, we decide to investigate the feasibility of TiO_2 as an electrode for MIBs in All Phenyl Complex (APC) electrolyte.[175] This electrolyte contains pure magnesium salt in THF solution and has electrochemical windows wider than 3 V. This widely acknowledged electrolyte in MIBs is thus the best candidate to examine the magnesium insertion into anatase TiO_2. Both spectroscopic and microscopic techniques have been applied to confirm the limitation of magnesium insertion into anatase TiO_2 through both electrochemical and chemical process.

7.2. Experimental

7.2.1. Electrolyte Preparation

All chemicals purchased were used as obtained without further purification. Aluminum chloride (99%) was obtained from Alfa Aesar while $AlCl_3$ (99.999%) was purchased from Sigma-Aldrich. THF was purchased from BASF with a reported water concentration of 20 ppm. 2 M phenylmagnesium chloride in THF was obtained from Sigma-Aldrich. Water analysis was performed using a Mettler-Toledo Karl Fischer Coulometric Titrator. All work, unless otherwise noted, was performed in an M. The electrolyte solution for magnesium deposition was prepared in a glove box filled with high purity argon gas. Firstly $AlCl_3$ was added slowly to the vigorously stirred THF solvent to obtain the desired concentration $AlCl_3$ solution. Then, this solution was added dropwise to a predetermined quantity of 2 M Phenylmagnesiumchloride (PhMgCl) solution in THF. Both reactions are very exothermic. The resulting solution was stirred for additional 20 h or more (at room temperature). A conventional electrolyte solution; ethylene carbonate (EC) and dimethyl carbonate (DMC) mixed solvent containing 1M of lithium hexafluorophosphate (LiPF6) was used for the electro deposition of lithium.

7.2.2. Electrolyte Characterization

All the electrochemical process of magnesium and lithium were performed by using a three electrode cell in a glove box filled with high purity argon. A polished magnesium ribbon was used as the working, reference and counter electrode for the magnesium deposition. The electro deposition of lithium was performed by using well polished lithium foil as a working electrode, reference and the counter electrode. The electro deposition of the magnesium and lithium were carried out by galvanostatic method under two different current densities 4.0 and

2.0 mA cm^{-2}. The electro deposition processes for one cycle were terminated by total electric charge at 14.4 and 7.2 C cm^{-2} for magnesium and lithium, respectively. The whole process for each case was conducted for 10 cycles. After 10 cycles' electro deposition, the magnesium deposits were immediately rinsed with THF for 3 times to remove electrolyte solution and transferred to SEM as soon as possible to avoid an exposure of the sample into air. In the case of the lithium, obtained specimens were rinsed with DMC instead of THF and transferred to SEM by following the same procedure as magnesium specimens.

7.2.3. Electrochemical Testing with TiO$_2$ Electrode

Commercially available TiO$_2$ (Sigma Aldrich, <20 nm particle size) was used without further treatment. The cathode electrode consisted of 70 wt. % active materials, 20 wt. % carbon black, and 10 wt. % PTFE. Individual electrode were punched with a desired mass of < 5 mg. Magnesium counter electrode was purchased from Alfa-Aesar and the surface was mechanically cleaned in an inert gas environment prior to use. The electrolyte (All Phenyl Complex, APC) was prepared by adding a tetrahydrofuran solution of phenylmagnesium chloride (2.0 M, Sigma Aldrich) into a THF solution of aluminum chloride (Sigma Aldrich, 99.999%) [13]. A glass fiber GF/F (Whatman) filter was used as the separator.

Swagelok-type cells were assembled in an Ar-filled glove box (H$_2$O < 0.1 ppm). Electrochemical measurements were conducted on an Arbin BT2000 battery cycler at ambient temperature. Galvanostatic experiments were performed at a current density of 5 μA mg^{-1} between 2.2 – 0.05 V. Potentiostatic experiments were performed at a constant voltage at 2.2 V until a cutoff current at 5 μA mg^{-1}. Cyclic voltammetry measurements were performed on the same battery cycler between 2.35 – 0.05 V with a scan rate of 0.1 mV s^{-1}.

7.2.4. Structural Characterizations

Following electrochemical galvanostatic/ potentiostatic charge/ discharge experiments, TiO_2 electrodes were carefully removed from electrochemical cells in an argon filled glove box and examined under various of spectroscopic and microscopic techniques. The electrodes were washed using battery grade THF solvent three times prior to use. The powders from the cycled electrode were then mounted in hermitically sealed capillary tubes for *ex situ* XRD. Powder diffraction spectra of all samples were taken using synchrotron XRD at the Advanced Photon Source (APS) on beamline 11-ID-C. The beamline uses a sagittal focused X-ray beam with a high precision diffractometer circle and perfect Si (111) crystal analyzer detection for high sensitivity and resolution. Following a careful transfer step to reduce any exposure to oxygen, the TiO_2 electrodes were examined using scanning electron microscopy (Phillips XL30) with an equipped energy dispersive X-ray detector (EDX). UV−vis spectra were carried out in an absorption mode on a Lambda 1050 UV−Vis spectrometer.

7.3. Results and Discussion

7.3.1. Electrolyte Characterization

Electrolyte stability is a key factor in exploring the electrochemical performance of a magnesium battery system. As shown in Figure 7.1, APC electrolyte used in this work shows highly reversible Mg deposition with low overpotential. Large initial overpotential for Mg plating is associated with oxides on Mg anode surface. High coulombic efficiency is purported to be the result of the absence of surface layer on magnesium surface following the initial plating.
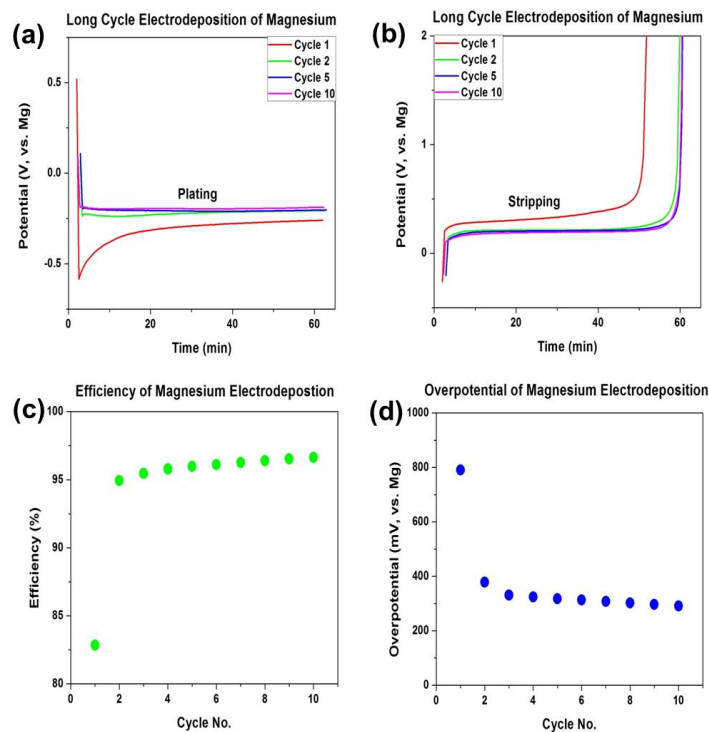
Figure 7.1. (a), (b) are the potential response results during chronopotentiometry experiments carried out with 0.25 M APC electrolyte in THF at room temperature for 10 cycles; (c), (d) are coulombic efficiency and overpotential calculated from the chronopotentiometry experiments.

SEM images of the magnesium deposits are shown in Figure 7.2. The counter electrode of magnesium deposits obtained at 4 mA cm^{-2} after 10 cycles showed even surface morphology as shown in Figure 7.2 (c) and (d). The magnesium deposits on the counter electrode have round shaped grains with uniform size approximately 2–3 μm. The magnified images of these deposits showed that each grain has clear edge which is reflecting the hexagonal structure of magnesium. Although the mechanism is still under investigated, it is noted that the over potential for magnesium deposition and dissolution is quite different.
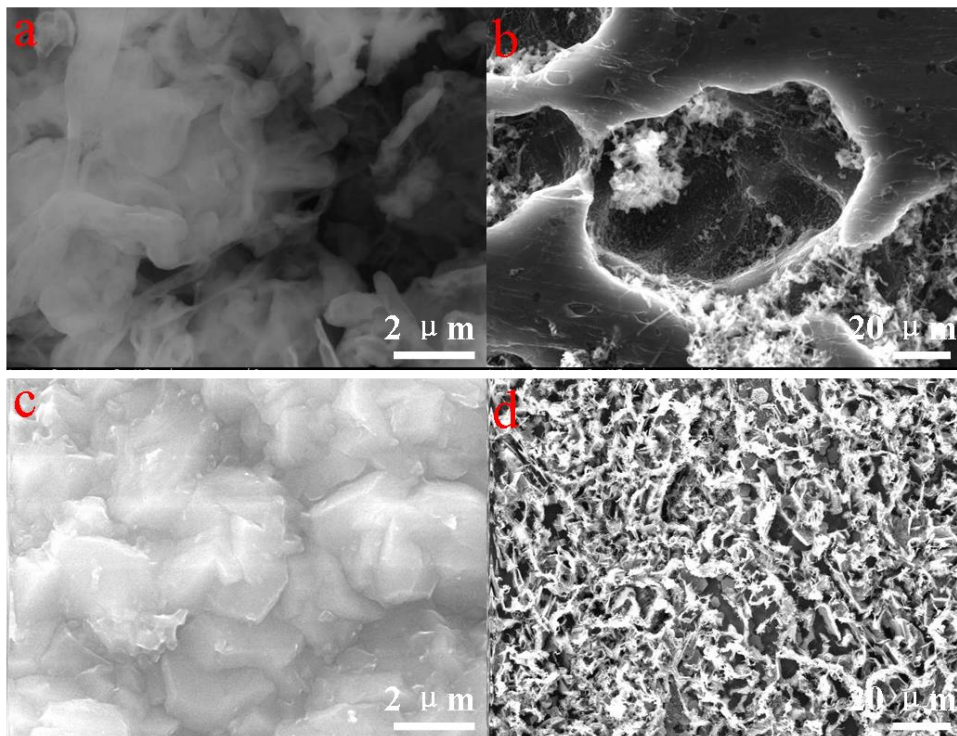
Figure 7.2. Comparison SEM images of the electrodeposited: (a, b) lithium counter electrode, and (c, d) magnesium counter electrode.

On the other hand, the lithium deposits showed very different surface morphology compared with the magnesium deposits as shown in Figure 7.2. The lithium deposits obtained at 4 mA cm^{-2} showed uneven surface morphology as shown in Figure 7.2 (a) and (b). Some whisker like lithium deposits (usually called just dendrite) were gathering to form porous deposition products. On the contrary, it can be said that all the magnesium deposits did not show a typical dendritic morphology even at such a large current density after 10 cycles.

7.3.2. Electrochemical Properties of Anatase-TiO$_2$

The crystal structure of anatase TiO$_2$ in polyhedral representation is presented in Figure 7.3, which was drawn using Crystal maker software by imputing the space group, the cell parameters, the atomic parameters, etc. Typical octahedral and tetrahedral patterns could be recognized. TiO$_2$ (anatase) has a tetragonal phase (space group I41/amd, number 141). The overall orthorhombic distortion of the atomic positions in the change from magnesium insertion is small and leads to more regularly shaped TiO$_6$ octahedra in magnesium titanate than in anatase. The change in symmetry is accompanied by a decrease of the unit cell along the c-axis and an increase along the b-axis, resulting in an increase of 4% of the unit cell volume.
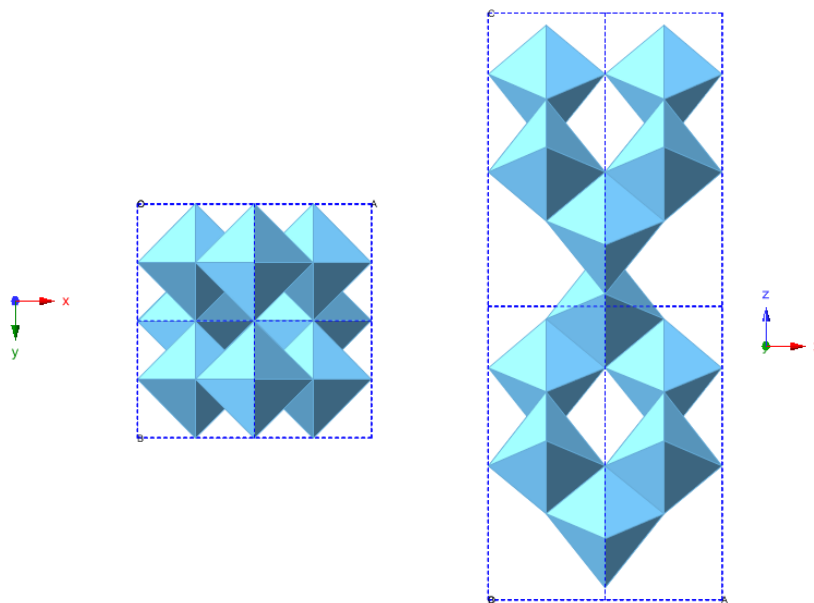
Figure 7.3. Anatase TiO$_2$ crystal structure in polyhedral representation.

Cyclic voltammograms of anatase TiO$_2$ electrode at a low scan rate of 0.1mV s^{-1} between 0.02 V and 2.35 V were shown in Figure 7.4. The results indicated Mg batteries with anatase TiO$_2$ electrode undergo two-step reversible Mg intercalation and conversion reactions.

Correspondingly, from the CV test, we have two redox couples, at around 0.8 V and 0.25 respectively. It should be noted that to extract Mg ion out is much easier than move it in.
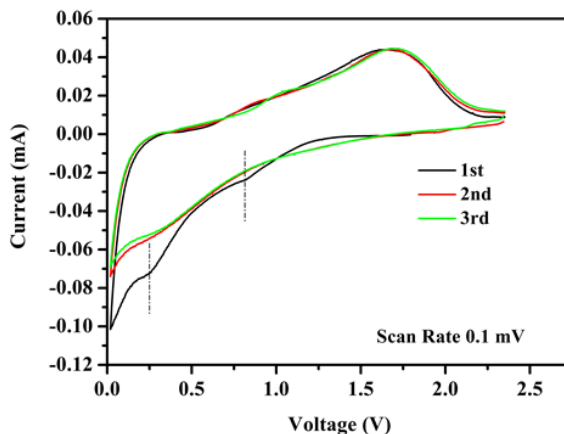
Figure 7.4. Cyclic voltammograms of anatase TiO_2 electrode at a scan rate of 0.1mV s^{-1} in a typical steady state.

The cathodic peak (magnetisation) at around 0.8 V, 0.25 V and the anodic peak (de-magnetisation) at around 1.7 V in the cyclic voltammograms correspond to the charge–discharge curves shown in Figure 7.5, this is consistent with a previous report by Li. As can be seen from Figure 7.5, when charged and discharged at a rate of 0.1 C, the sample can deliver a discharge capacity over 80 mAh g^{-1} with a little irreversible capacity, which shows a promising application for magnesium ion battery. However, due to the side reaction between the electrolyte and the current collector, the cycling performance of the battery was still under optimized.
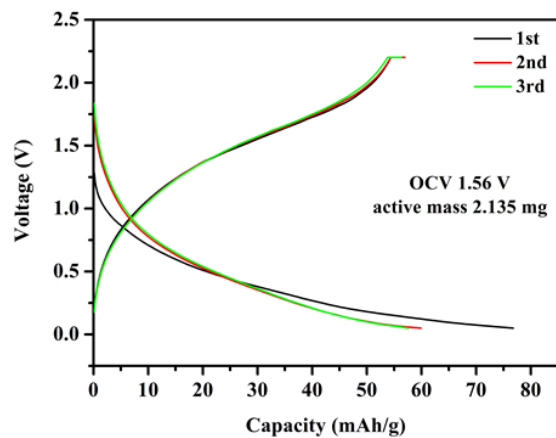
Figure 7.5. First three discharge and charge plots of the anatase TiO$_2$ electrode.

Figure 7.6 presents the cycling performance as well as discharge profiles for 5th, 10th, 15th and 20th cycles of the sample anatase TiO$_2$ electrode under a current density of 5 mA g^{-1}, in the voltage range of 0.02–2.2 V. Clearly, the sample anatase TiO$_2$ electrode not only shows a large discharge capacity at the starting period, it also exhibits a good retention after 20 cycles, which means the sample anatase TiO$_2$ electrode is promising to use as electrode for magnesium ion batteries.
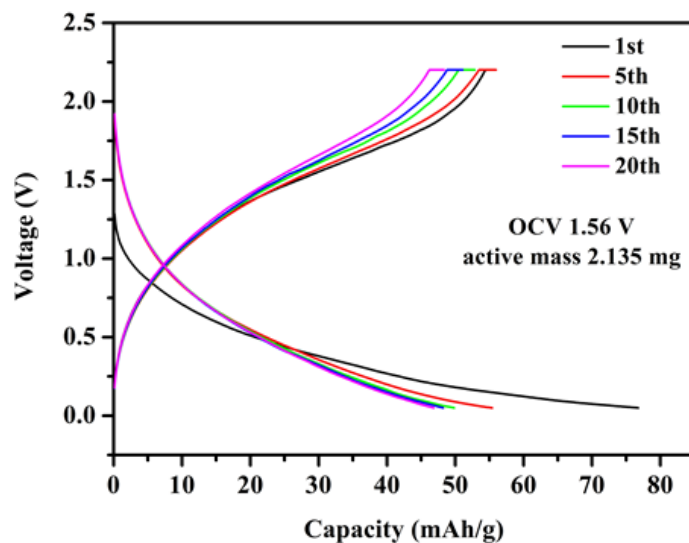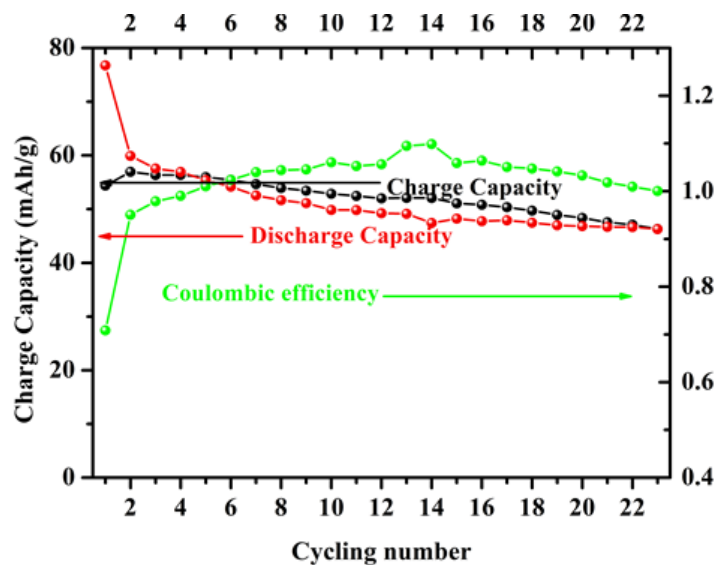
Figure 7.6. Cycling performance of the sample anatase TiO_2 electrode.

7.3.3. Investigation of Magnesium Insertion into Anatase-TiO_2

In order to investigate the phase transitions, *ex-situ* XRD patterns were collected at different states of charge-discharge in Figure 7.7. The pristine electrode demonstrates a typical tetragonal anatase phase with space group I41/amd. No explicit changes are found at all different states, showing the retention of the tetragonal anatase phase.
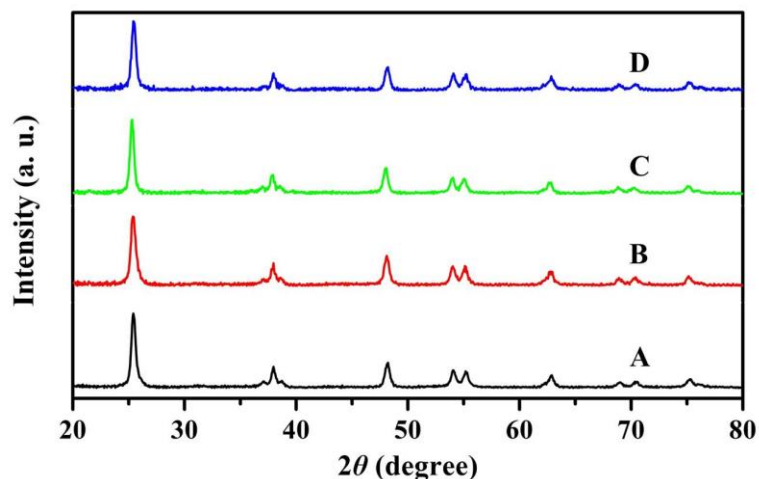
Figure 7.7. *Ex-situ* XRD patterns at different states of discharge and charge during the first electrochemical cycle of anatase TiO_2/Mg battery. (A) pristine state; (B) and (C) discharged to 0.6 V and 0.05 V at a current density of 5 mA g^{-1}; (D) charged to 2.2 V at a current density of 5 mA g^{-1}.

Figure 7.8 further shows the detailed crystal structure evolution during the first cycle based on high resolution synchrotron X-ray diffraction. Despite their similar crystal structures, Table 7.1 quantitatively exhibits the a- and c-lattice parameters for each electrode at different state by Rietveld refinement. The R factors from the Rietveld refinements are less than 8%, which indicates that the results are reliable to describe the crystal structure. The lattice parameters of pristine TiO_2 electrode are a = 3.789 Å and c = 9.512 Å, which are in good agreement with previous XRD study. As a comparison, the lattice parameters of fully discharged electrode are a = 3.792 Å and c = 9.503 Å. This observation confirms the slight increase of a- lattice parameter and shrink of c- lattice parameter. During Mg-ion insertion, the a- lattice parameter, which is dominated by the M–M distance, increases slightly as expected from the oxidation of Ti ions. The shrink of c- lattice parameter of the fully

114

discharged electrode is due to less electrostatic repulsion between adjacent oxygen layers. Both a- and c- lattice parameters change back more or less to the original numbers for the fully charged state, where only the tetragonal phase remains, indicative of good reversibility. It should be noted, the relatively slight changes of the lattice parameter, yet within the error range as indicated from Table 7.1, results from only Mg:Ti ratio of ~0.1:1 (inferred from the initial discharge capacity) inserted into TiO_2 structure at the fully discharge state by the electrochemical method.
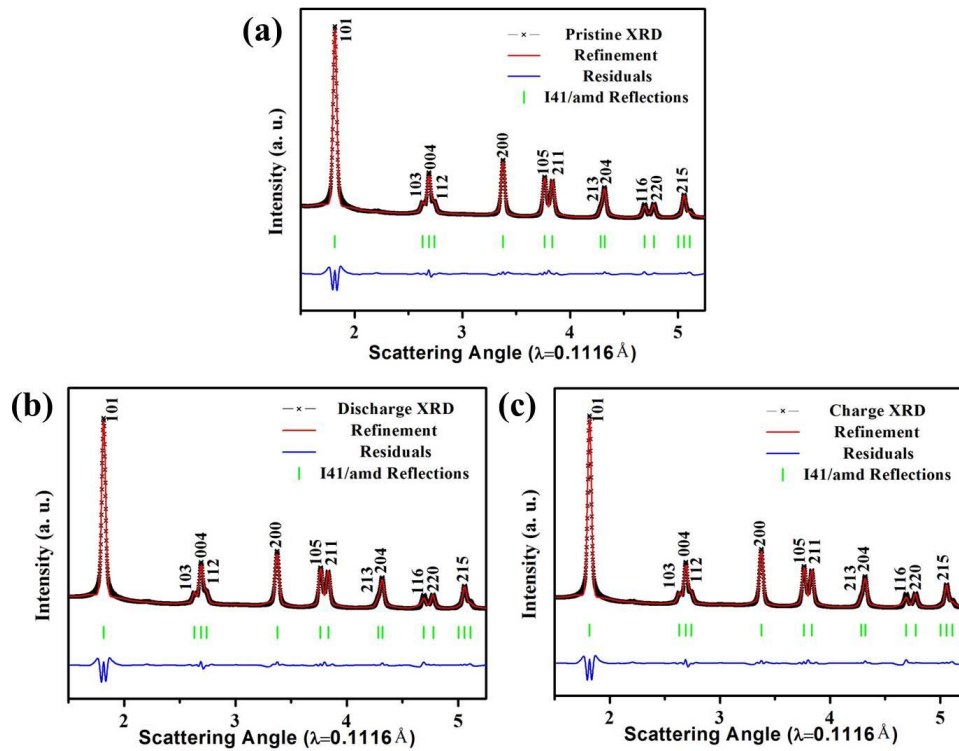
Figure 7.8. (a)-(c) *Ex-situ* synchrotron XRD patterns for the TiO_2 electrode at pristine, fully discharged and charged states, respectively.

Table 7.1. Rietveld refinement method fitted parameters of TiO_2 electrode.

Material	$a=b$ (Å)	c (Å)	R_{wp} (%)	R_B (%)
Pristine	3.7896(3)	9.5124(7)	6.74	3.99
Discharge	3.7927(3)	9.5039(7)	6.58	4.30
Charge	3.7908(3)	9.5086(7)	7.32	5.40

In order to quantify Mg insertion into anatase TiO_2 structure, the electrodes were examined using scanning electron microscopy (Phillips XL30) with an equipped energy dispersive X-ray detector (EDX). It was found that following discharge of the cell to 0.05 V, a magnesium signal is observed in the EDX mapping (Figure 7.9a). Quantitation of this finding resulted in a Mg:Ti ratio of ~0.1:1, which is also inferred from the initial discharge capacity. To determine the ability of Mg to reversibly shuttle between the working and counter electrodes, magnesiated TiO_2 electrode was charged from 0.05 – 2.2 V and removed for SEM/EDX analysis. No obvious magnesium signal can be seen in the EDX mapping (Figure 7.9b), indicating that magnesium ions can reversibly diffuse between the magnesium metal counter electrode and titanium dioxide working electrode.
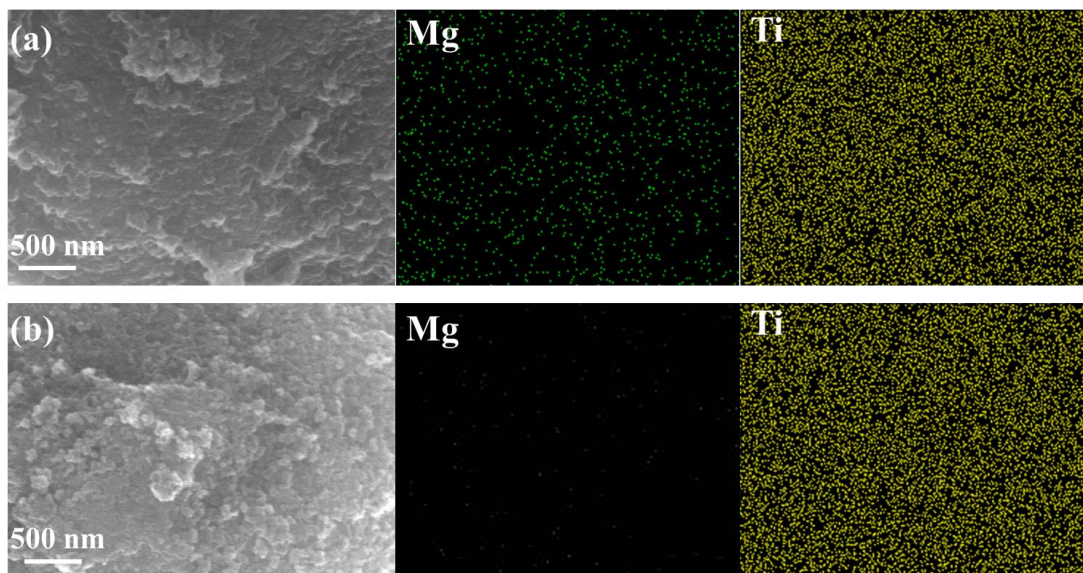
Figure 7.9. (a), (b) SEM/EDX mapping for the TiO_2 electrode at fully discharged and charged states, respectively.

As discussed above, a Mg:Ti ratio of ~0.1:1 could be inserted into anatase TiO_2 through electrochemical method. To investigate the limitation of Mg insertion into anatase TiO_2, chemical magnesiation was attempted using a method shown in scheme 1. A strong color change was observed (Figure 7.10a), with the white TiO_2 powder suspension solution becoming a deep blue. This phenomena has been previously described for chemical lithiation of anatase TiO_2 using the analogous *n*-butyl lithium.[179] Elemental analysis using EDX was likewise performed on this proprietary material. As shown in Figure 7.11, an obvious magnesium signal is visible in the elemental mapping, with a quantitation value nearly identical to that of the electrochemically magnesiated TiO_2. This is interesting to note, as the starting stoichiometric ratio of Mg:Ti for chemical magnesiation is 1:4, not 1:10. As a result, a limiting magnesiation capacity is reached for both electrochemical and chemical ion insertion.

$$\text{TiO}_2 + 2.5\ \text{Bu}_2\text{Mg} \xrightarrow[\text{5 days RT}]{\text{heptane}} \text{Mg}_x\text{TiO}_2 + \text{Bu}_2$$

Calculation:
$$E = hc/\lambda$$
λ = Interception wavelength
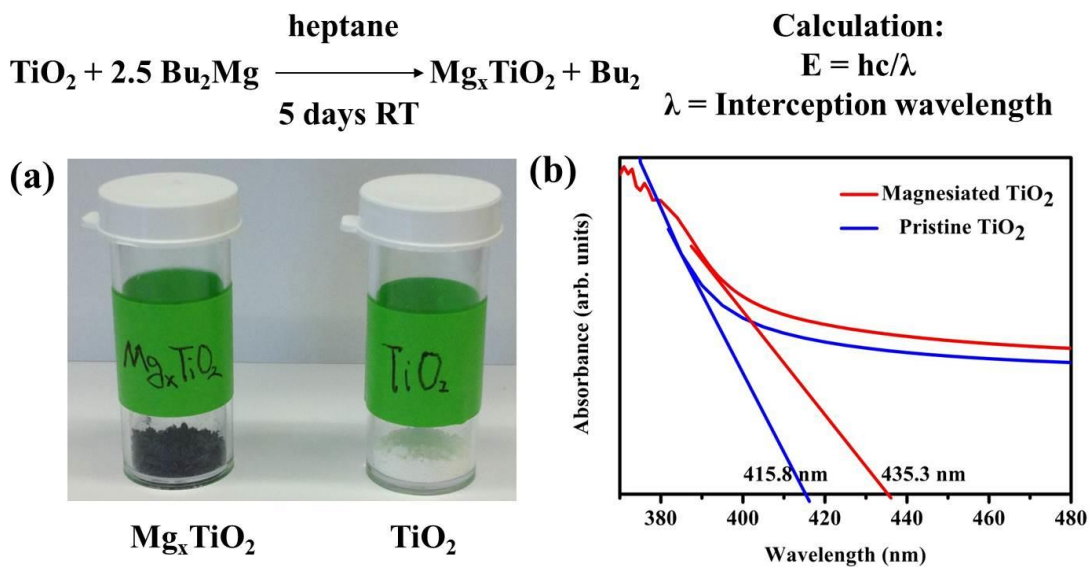
Figure 7.10. (a) Chemical magnesiation process and samples obtained; (b) UV−vis spectra for the pristine and magnesiated samples.
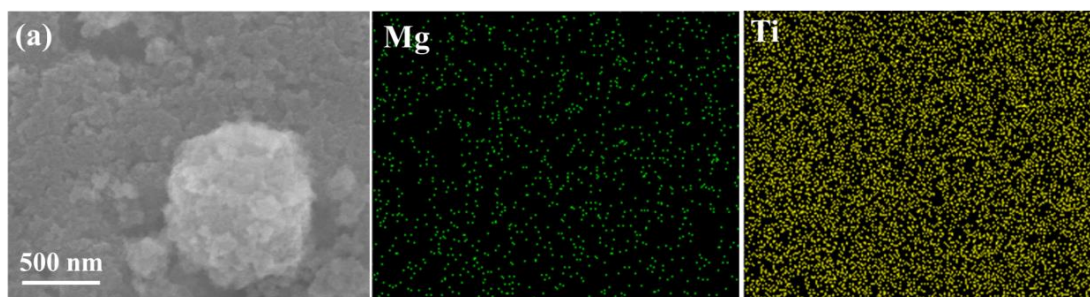
Figure 7.11. (a) The SEM image of the chemical magnesiation sample and corresponding quantitative EDX element mapping of Mg and Ti.

Insertion of an electrochemically active ion into a host structure results in a reduction of one of the metal ion in the host structure. As a result, the energy difference between the valence and conduction bands of the host metal ion should change upon intercalation. This phenomena has been observed in the lithiation of titanium dioxide.[180] Therefore, as another method to confirm that magnesium ions inserted into the anatase TiO_2 host structure, UV−vis spectra were

118

carried out in an absorption mode for the pristine and magnesiation samples (Figure 7.10b). As summarized in Table 7.2, the interception wavelength of magnesiation sample increases dramatically compared with that of pristine TiO_2, which makes it clearly magnesium insertion indeed changes the energy difference between the valence and conduction bands of the host structure.

Table 7.2. Interception wavelength and band gap calculated results from UV-vis spectra.

Sample	Wavelength Edge (nm)	Band Gap (eV)
Pristine	415.8	2.99
Magnesiated	435.3	2.87

The decrease of bandgap leads to improvement of the electronic conductivity of TiO_2 after magnesiation, which indicates a good rate capability as shown in Figure S4. The material still exhibits a discharge capacity of ~45 mAh g^{-1} at a current density of 40 mA g^{-1}.
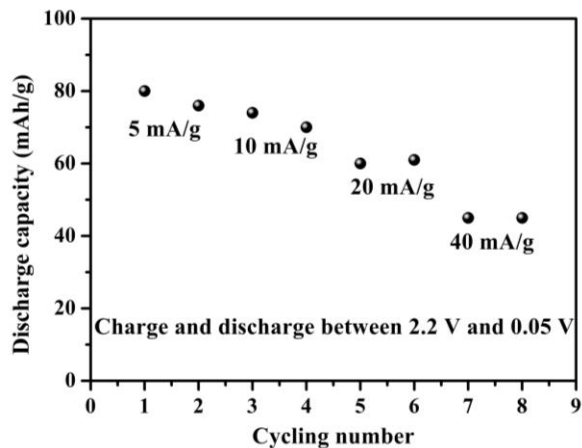
Figure 7.12. Rate capability of anatase TiO$_2$/Mg battery in APC electrolyte.

7.4. Conclusion

In conclusion, commercial anatase TiO$_2$, as cathode material for magnesium batteries, exhibits promising electrochemical performance in APC electrolyte. Both spectroscopic and microscopic techniques confirm that a Mg:Ti ratio of ~0.1:1 could be inserted into anatase TiO$_2$ electrochemically or chemically. And magnesium ions can reversibly diffuse between the magnesium metal counter electrode and titanium dioxide working electrode. Although tetragonal anatase phase is reserved throughout insertion/extraction process, the energy difference between the valence and conduction bands of the host material changes confirmed by UV−vis spectra. The different insertion ability of lithium and magnesium ions into anatase TiO$_2$ once more manifests kinetic sluggish of Mg^{2+} ion diffusion process.

This chapter in full, is a reprint of the material "Investigation of Anatase-TiO$_2$ as an Efficient Electrode Material for Magnesium-Ion Batteries" as it appears in Journal of The Electrochemical Society, Zhang, M.; MacRaea, A. C.; Liu, H. D.; Meng, Y. S., 2016, 163(10), A2368. The dissertation author was the primary investigator and first author of this paper. All of the experiment parts were performed by the author except for the UV−vis spectra.

Chapter 8. Summary and Outlook

With the increasing demand of energy and power in all electric devices and vehicles, a high capacity with a high-rate long-life lithium-ion battery must be achieved, which drives the discovery of a novel composite cathode. Presently, one of the most promising candidates for the next generation of lithium-ion battery cathode materials is the lithium-rich layered oxide. It has an extraordinary high capacity of up to 320 mAh g^{-1} versus a practical capacity of ~150 mAh g^{-1} for the commercial $LiCoO_2$ whose increase is subject of active research in the battery community. However, this material undergoes voltage fading and instability that is rooted in structural failure, and despite their importance, deep understanding of the structural transformation has not been explored. The focus of my thesis was to investigate meso-structure controlled synthesis, surface modification method, and defects elimination strategy to address the cycling stability issue of Li-rich layered oxide cathode.

In Chapter 4, a modified co-precipitation (MCP) method has been developed to synthesize meso-structure controlled Li-rich layered oxide material. Different from the co-precipitation method with ammonia addition, this MCP method produces smaller spherical secondary particles with an average diameter of approximately 3 μm. Though sacrificing some tap density, the designed meso-structure is more mechanically stable during electrochemical cycling compared with the secondary particles with 10~20 μm. Spherical shape secondary particles still well maintain without internal cracks and high stress generation after cycling. These observations indicate a balance between tap density and structure stability needs to be considered for optimization of this class of materials synthesized by co-precipitation method. Additionally, the designed meso-structure has a much smaller surface area compared with the sample with dispersive particles. Consequently, no obvious capacity fading and voltage

degradation is observed for the meso-structure controlled sample even after 150 cycles, which shows the MCP method is promising for minimizing the capacity and voltage fading problem during cycling of Li-rich layered material. Long cycling duration of these materials still needs to be optimized based on the atomic structure transformation to fully suppress the voltage decay and capacity fading.

In Chapter 5, a facile but effective approach to surface modification based on GSIR has been applied to create oxygen vacancies homogeneously without causing structural destruction. Oxygen vacancies in the surface regions up to 20-nm thick are found to facilitate Li diffusion by activating the Li in the tetrahedral sites and suppress the release of gas from the surface, which finally lead to higher discharge capacity and a better rate capability in the Li-rich layered oxides. To the best of our knowledge, this study also clarifies for the first time the critical influence of the activity of surface oxygen in enhancing the electrochemical performance. We believe this facile, scalable and inexpensive approach opens a door for comprehensive designing and controlling oxygen activity in transition-metal-oxide systems to achieve excellent energy and power density in their commercial applications.

In Chapter 6, combined ND, STEM, SXRD, and first principles calculations on high-capacity LR-NCM materials reveals the structure metastability of the cycled structure responsible for the voltage decay in Li-rich layered electrode materials. This study pinpoints the critical influence of defects generation on the structure metastability and voltage decay. More importantly, these results suggest research directions that defects elimination can help obviate the voltage decay issue. Based on the mechanistic description above we design a path to remove the defects in the structure by high temperature annealing. The treatment at high temperature recovers the superstructure and average discharge voltage. This novel understanding of the

123

structure metastability and reversibility phenomenon will provide clues for identifying more realistic pathway to fully address voltage decay issue of high-capacity Li-rich layered oxide electrodes.

Given the abovementioned work, there is definitely room for further mechanism understanding and cycling performance improvement of lithium-rich layered oxide cathode. For future work, the first proposition is to investigate how the meso-structure control affects TM migration and phase transformation throughout the whole secondary particles. As mentioned in my thesis, the oxygen evolution from the initial cycle triggers the migration of TM into the Li layer to form defect spinel phase as well as segregation between nickel and manganese on the particles' surface. In the meso-structure controlled sample, exterior primary particles act as coating layer to prevent majority of interior primary particles direct contact with the electrolyte, which will introduce less side reactions between released oxygen and the electrolyte species. Less TM migration and phase transformation is thus expected to form on the interior particles' surface, which enables a minimized capacity and voltage fading during cycling process. In order to better understand the mechanism, detailed studies including TM migration and phase transformation are needed for both interior and exterior primary particles through HRSTEM and EELS mapping.

The second proposition is to apply lithium conductor coating on the particle surface to further improve the cycling performance of Li-rich layered oxide. Experimentally, coating with LLTO (lithium lanthanum titanium oxides) could significantly improve the cycling performance. However, understanding the mechanism of LLTO coating is of extreme importance to eventually solve the disadvantages in the material and realize final commercialization. In this proposed study, the following scientific questions should be answered: 1) How would the coating affect

the oxygen vacancy formation? 2) How would the coating influence the TM migration and phase transformation? 3) Is the coating a continuous effect? Because the commercialization requires long cycle life with steady improvement on the performance, whether the coating has a continuous effect is critical for the further optimization of this family of materials.

The third proposition is to explore the effects of different elements substitution on the presence of oxygen vacancy in Li-rich layered oxide materials. As mentioned in this thesis, the oxygen vacancy is generated when more than 1/2 Li ions are extracted out from the structure. These oxygen vacancies assist TM migration mechanism for the phase transition. In order to form strong bond with oxygen and increase the oxygen vacancy formation energy, searching a proper element to substitute Mn or slightly Ni is of great importance.

In addition, magnesium rechargeable batteries which have been studied for a long time, have begun to draw attention for next generation power storage applications. Magnesium is a low-cost, safe to handle, environmentally friendly and naturally abundant, and most importantly dendrite free electrodeposition metal. This makes Mg metal can be directly applied as the anode in MIBs, which will double the specific volumetric capacity of the energy storage system. This thesis also focused on the potential cathode for MIBs, which is the major barrier of MIBs development. Both spectroscopic and microscopic techniques confirm that a Mg:Ti ratio of $\sim$0.1:1 can be inserted into anatase TiO_2 electrochemically or chemically without phase transformation. The different insertion ability of lithium and magnesium ions into anatase TiO_2 once more manifests the sluggish kinetics of Mg^{2+} ion diffusion process.

The major challenge for MIBs is to develop low cost electrodes with longer cycling life for the various applications discussed in this thesis. New approaches in making unique

nanostructures with carbon incorporation will be the next step for oxides to allow for multi-electron transitions enabling higher energy densities. In comparison to oxide materials, Chevrel phases are promising as the next generation cathode material which can effectively screen the large electrostatic force. In particular, compared to electrolytes used in lithium-ion batteries, magnesium-based electrolytes at present show much narrower potential windows. The development of electrolyte systems with wide electrochemical windows and high compatibility with battery components is crucial to discovering novel type of cathodes.

References

(1)   Tarascon, J.-M.; Armand, M. *Nature* **2001**, *414*, 359.

(2)   Zhou, F.; Zhao, X.; Dahn, J. R. *J. Electrochem. Soc.* **2010**, *157 (7)*, A798.

(3)   Baginska, M.; Blaiszik, B. J.; Merriman, R. J.; Sottos, N. R.; Moore, J. S.; White, S. R. *Adv. Energy Mater.* **2012**, *2 (5)*, 583.

(4)   Scrosati B. *Electrochim. Acta* **2000**, *45*, 2461.

(5)   Ma, J.; Hu, P.; Cui, G.; Chen, L. *Chem. Mater.* **2016**, *28 (11)*, 3578.

(6)   Kang, K. S.; Meng, Y. S.; Breger, J.; Grey, C. P.; Ceder, G. *Science* **2006**, *311*, 977.

(7)   Periasamy, P.; Kalaiselvi, N.; Kim, H. S. *Int. J. Electrochem. Sci.* **2007**, *2*, 689.

(8)   Padhi, A. K.; Nanjundaswamy, K. S.; Goodenough, J. B. *J. Electrochem. Soc.* **1997**, *144*, 1188.

(9)   Johnson, C. S.; Kim, J. S.; Lefief, C.; Li, N.; Vaughey, J. T.; Thackeray, M. M. *Electrochem. Commun.* **2004**, *6*, 1085.

(10)   Arunkumar, T. A.; Wu, Y.; Manthiram, A. *Chem. Mater.* **2007**, *19*, 3067.

(11)   Armstrong, R.; Holzapfel, M.; Novak, P.; Johnson, C. S.; Kang, S. H.; Thackeray, M. M.; Bruce, P. G. *J. Am. Soc.* **2006**, *128*, 8694.

(12)   Sung, N. E.; Sun, Y. K.; Kim, S. K.; Jang, M. S. *J. Electronchem. Soc.* **2008**, *155*, A845.

(13)   Kang, S. H.; Johnson, C. S.; Vaughey, J. T.; Amine, K.; Thackeray, M. M.; *J. Electrochem. Soc.* **2006**, *153*, A1186.

(14)   Manthiram, A. *J. Phys. Chem. Lett.* **2011**, *2*, 176.

(15)   Wu, Y.; Manthiram, A. *Electrochem. Solid-State Lett.* **2006**, *9*, A221.

(16)   Shin, D.; Wolverton, C.; Croy, J. R.; Balasubramanian, M.; Kang, S. H.; Rivera, C. M. L.; Thackeray, M. M. *J. Electrochem. Soc.* **2012**, *159*, A121.

(17)   Peng, B.; Liang, J.; Tao, Z.; Chen, J. *J. Mater. Chem.* **2009**, *19*, 2877.

(18)   NuLi, Y.; Guo, Z.; Liu, H.; Yang, J. *Electrochem. Commun.* **2007**, *9*, 1913.

(19)   Li, W. Y.; Li, C. S.; Zhou, C. Y.; Ma, H.; Chen, J. *Angew. Chem., Int. Ed.* **2006**, *45*, 6009.

(20)   Whittingham, M. S. *Science* **1976**, *192*, 1126.

(21) Mizushima, K.; Jones, P. C.; Wiseman, P. J.; Goodenough, J. B. *Mater. Res. Bull.* **1980**, *15*, 783.

(22) Roy, P.; Srivastava, S. K. *J. Mater. Chem. A* **2015**, *3*, 2454.

(23) Dahn, J. R.; Fuller, E. W.; Obrovac, M.; Von Sacken, U. *Solid State Ionics* **1994**, *69*, 265.

(24) Amatucci, G. G.; Tarascon, J. M.; Klein, L. C. *J. Electrochem. Soc.* **1996**, *143*, 1114.

(25) Van der Ven, A.; Aydinol, M. K.; Ceder, G.; Kresse, G.; Hafner, J. *Phys. Rev. B: Condens. Matter Mater. Phys.* **1998**, *58*, 2975.

(26) Thackeray, M. M.; David, W. I. F.; Bruce, P. G.; Goodenough, J. B. *Mater. Res. Bull.* **1983**, *18*, 461.

(27) David, W. I. F.; Thackeray, M. M.; Bruce, P. G.; Goodenough, J. B. *Mater. Res. Bull.* **1984**, *19*, 99.

(28) Aurbach, D.; Levi, M. D.; Gamulski, K.; Markovsky, B.; Salitra, G.; Levi, E.; Heider, U.; Heider, L.; Oesten, R. *J. Power Sources* **1999**, *81*, 472.

(29) Shin, Y. J.; Manthiram, A. *J. Electrochem. Soc.* **2004**, *151*, A204.

(30) Xia, Y. Y.; Zhou, Y. H.; Yoshio, M. *J. Electrochem. Soc.* **1997**, *144*, 2593.

(31) Prosini, P. P.; Zane, D.; Pasquali, M. *Electrochim. Acta* **2001**, *46*, 3517.

(32) Chung, S-Y.; Bloking, J. T.; Chiant, Y-M. *Nat. Mat.* **2002**, *1*, 123.

(33) Jugovic, D.; Uskokovic, D. *J. Power Sources* **2009**, *190*, 538.

(34) Huang, H.; Yin, S-C.; Nazar, L.F. *Electrochem. Solid-St. Lett.* **2001**, *4(10)*, A170.

(35) Delmas, C.; Mené trier, M.; Croguennec, L.; Saadoune, I.; Rougier, A.; Pouillerie, C.; Prado, G.; Grüne, M.; Fournes, L. *Electrochim. Acta* **1999**, *45*, 243.

(36) Dahn, J. R.; Von Sacken, U.; Juzkow, M. W.; Al-Janaby, H. *J. Electrochem. Soc.* **1991**, *138*, 2207.

(37) Bruce, P. G.; Armstrong, A. R.; Gitzendanner, R. L. *J. Mater. Chem.* **1999**, *9*, 193.

(38) Armstrong, A. R.; Bruce, P. G. *Nature* **1996**, *381*, 499.

(39) Ohzuku, T.; Makimura, Y. *Chem. Lett.* **2001**, *30*, 744.

(40) Ohzuku, T.; Makimura, Y. *Chem. Lett.* **2001**, *30*, 642.

(41) Thackeray, M. M.; Kang, S.-H.; Johnson, C. S.; Vaughey, J. T.; Benedek, R.; Hackney, S. A. *J. Mater. Chem.* **2007**, *17*, 3112.

(42) Lu, Z. H.; MacNeil, D. D.; Dahn, J. R. *Electrochem. Solid-State Lett.* **2001**, *4*, A191.

(43) Lu, Z. H.; Beaulieu, L. Y.; Donaberger, R. A.; Thomas, C. L.; Dahn, J. R. *J. Electrochem. Soc.* **2002**, *149*, A778.

(44) Ammundsen, B.; Paulsen, J. *Adv. Mater.* **2001**, *13*, 943.

(45) Ammundsen, B.; Paulsen, J.; Davidson, I.; Liu, R. S.; Shen, C. H.; Chen, J. M.; Jang, L. Y.; Lee, J. F. *J. Electrochem. Soc.* 2002, 149, A431.

(46)   Meng, Y. S.; Ceder, G.; Grey, C. P.; Yoon, W. S.; Jiang, M.; Breger, J.; Shao-Horn, Y. *Chem. Mater.* **2005**, *17*, 2386.

(47) Rozier, P.; Tarascon, J.-M. *J. Electrochem. Soc.* **2015**, *162*, A2490.

(48) Lu, Z. H.; Dahn, J. R. *J. Electrochem. Soc.* **2002**, *149*, A815.

(49) Massarotti, V.; Bini, M.; Capsoni, D.; Altomare, A.; Moliterni, A. G. *J. Appl. Crystallogr.* **1997**, *30*, 123.

(50) Robertson, A. D.; Bruce, P. G. *Electrochem. Solid-State Lett.* **2004**, *7*, A294.

(51) Hy, S.; Liu, H.; Zhang, M.; Qian, D.; Hwang, B.-J.; Meng, Y. S. *Energy Environ. Sci.* **2016**, *9*, 1931.

(52) Seo, D. H.; Lee, J.; Urban, A.; Malik, R.; Kang, S.; Ceder, G. *Nat. Chem.* **2016**, *8*, 692.

(53)   Luo, K.; Roberts, M. R.; Hao, R.; Guerrini, N.; Pickup, D. M.; Liu, Y. S.; Edstrom, K.; Guo, J.; Chadwick, A. V.; Duda, L. C.; Bruce, P. G. *Nat. Chem.* **2016**, *8*, 684.

(54) McCalla, E.; Abakumov, A. M.; Saubanere, M.; Foix, D.; Berg, E. J.; Rousse, G.; Doublet, M. L.; Gonbeau, D.; Novak, P.; Van Tendeloo, G.; Dominko, R.; Tarascon, J. M. *Science* **2015**, *350*, 1516.

(55) Sathiya, M.; Rousse, G.; Ramesha, K.; Laisa, C. P.; Vezin, H.; Sougrati, M. T.; Doublet, M. L.; Foix, D.; Gonbeau, D.; Walker, W.; Prakash, A. S.; Ben Hassine, M.; Dupont, L.; Tarascon, J. M. *Nat. Mater.* **2013**, *12*, 827.

(56) Saubanere, M.; McCalla, E.; Tarascon, J. M.; Doublet, M. L. *Energy Environ. Sci.* **2016**, *9*, 984.

(57) Grimaud, A.; Hong, W. T.; Shao-Horn, Y.; Tarascon, J. M. *Nat. Mater.* **2016**, *15*, 121.

(58) Qian, D.; Xu, B.; Chi, M.; Meng, Y. S. *Phys. Chem. Chem. Phys.* **2014**, *16*, 14665.

(59) Carroll, K. J.; Qian, D.; Fell, C.; Calvin, S.; Veith, G. M.; Chi, M.; Baggetto, L.; Meng, Y. S. *Phys. Chem. Chem. Phys.* **2013**, *15*, 11128.

(60) Xu, B.; Fell, C. R.; Chi, M.; Meng, Y. S. *Energy Environ. Sci.* **2011**, *4*, 2223.

(61) Zhu, Z.; Kushima, A.; Yin, Z.; Qi, L.; Amine, K.; Lu, J.; Li, J. *Nat. Energy* **2016**, *1*, 16111.

(62) Yoo, H. D.; Shterenberg, I.; Gofer, Y.; Gershinsky, G.; Pour, N.; Aurbach, D. *Energy Environ. Sci.* **2013**, *6*, 2265.

(63) Aurbach, D.; Schechter, A.; Moshkovich, M.; Cohen, Y. *J. Electrochem. Soc.* **2001**, *148 (9)*, A1004.

(64) Yagi, S.; Tanaka, A.; Ichikawa, Y.; Ichitsubo, T.; Matsubara, E. *Res. Chem. Intermed.* **2014**, *40(1)*, 3.

(65) Ha, S. Y.; Lee, Y. W.; Woo, S. W.; Koo, B.; Kim, J. S.; Cho, J.; Lee, K. T.; Choi, N. S. *ACS Appl. Mater. Interfaces* **2014**, *6*, 4063.

(66) Aurbach, D.; Suresh, G. S.; Levi, E.; Mitelman, A.; Mizrahi, O.; Chusid, O.; Brunelli, M. *Adv. Mater.* **2007**, *19*, 4260.

(67) Jiao, L. F.; Yuan, H. T.; Wang, Y. J.; Cao, J. S.; Wang, Y. M. *Electrochem. Commun.* **2005**, *7*, 431.

(68) Inamoto, M.; Kurihara, H.; Yajima, T. *Electrochemistry* **2012**, *80*, 421.

(69) Sutto, T. E.; Duncan, T. T. *Electrochim. Acta* **2012**, *79*, 170.

(70) Rasul, S.; Suzuki, S.; Yamaguchi, S.; Miyayama, M. *Electrochim. Acta* **2012**, *82*, 243.

(71) Bonino, F.; Busani, L.; Manstretta, M.; Rivolta, B.; Scrosati, B. *J. Power Sources* **1981**, *6*, 261.

(72) Huang, S. Y.; Kavan, L.; Exnar, I.; Graָtzel, M. *J. Electrochem. Soc.* **1995**, *142*, L142.

(73) Aurbach, D.; Lu, Z.; Schechter, A.; Gofer, Y.; Gizbar, H.; Turgeman, R.; Cohen, Y.; Moshkovich, M.; Levi, E. *Nature* **2000**, *407*, 724.

(74) Williamson, G. K.; Hall, W. H. *Acta Metall.* **1953**, *1*, 22.

(75) Wang, J. (2017, November 15). Transmission X-ray Microscopy Beamline X8C NSLS, BNL. Retrieved from https://sites.google.com/site/nslsx8ctxm/beamline

(76) Wang, J.; Chen,Y.-c.K.; Yuan, Q.; Tkachuk, A.; Erdonmez, C.; Hornberger, B.; Feser, M. *Appl. Phys. Lett.* **2012**, *100*, 143107.

(77) Natterer, F. *The Mathematics of Computerized Tomography*; Wiley, New York, 1986.

(78) Chen, Y.-c.K.; Liu, Z.; Faber, K. T.; Barnett, S. A.; Wang, J. *Electrochem. Commun.* **2013**, *28*, 127.

(79) Qian, D.; Ma, C.; More, K. L.; Meng, Y. S.; Chi, M. *NPG Asia Mater.* **2015**, *7*, e193.

(80) Peng, Y. P.; Nellist, P. D.; Pennycook, S. J. *J. Electron Microsc.* **2004**, *53*, 257.

(81) Findlay, S. D.; Lugg, N. R.; Shibata, N.; Allen, L. J.; Ikuhara, Y. *Ultramicroscopy* **2011**, *111*, 1144.

(82) Egerton, R. F. *Rep. Prog. Phys.* **2009**, *72*, 016502.

(83) Chi, M. F.; Mizoguchi, T.; Martin, L. W.; Bradley, J. P.; Ikeno, H.; Ramesh, R.; Tanaka, I.; Browning, N. *J. Appl. Phys.* **2011**, *110*, 046104.

(84) Cho, T.; Park, S.; Yoshio, M. *Chem. Lett.* **2004**, *133*, 704.

(85) Park, S.; Cho, T.; Yoshio, M. *Chem. Lett.* **2004**, *133*, 748.

(86) Lee, D. K.; Park, S. H.; Amine, K.; Bang, H. J.; Parakash, J.; Sun, Y. K. *J. Power Sources* **2006**, *162*, 1346.

(87) Chen, L.; Su, Y.; Chen, S.; Li, N.; Bao, L.; Li, W.; Wang, Z.; Wang, M.; Wu, F. *Adv. Mater.* **2014**, *26*, 6756.

(88) Li, L.; Song, S.; Zhang, X.; Chen, R.; Lu, J.; Wu, F.; Amine, K. *J. Power Sources* **2014**, *272*, 922.

(89) Park, S. H.; Kanga, S. H.; Belharouak, I.; Sun, Y. K.; Amine, K. *J. Power Sources* **2008**, *177*, 177.

(90) Wang, D.; Belharouak, I.; Ortega, L. H.; Zhang, X.; Xu, R.; Zhou, D.; Zhou, G.; Amine, K. *J. Power Sources* **2015**, *274*, 451.

(91) Wang, D.; Belharouak, I.; Koenig, G. M.; Zhou, G.; Amine, K. *J. Mater. Chem.* **2011**, *21*, 9290.

(92) Oh, P.; Myeong, S.; Cho, W.; Lee, M. J.; Ko, M.; Jeong, H. Y.; Cho, J. *Nano Lett.* **2014**, *14*, 5965.

(93) Chen, C. J.; Pang, W. K.; Mori, T.; Peterson, V. K.; Sharma, N.; Lee, P. H.; Wu, S.; Wang, C. C.; Song, Y. F.; Liu, R. S. *J. Am. Chem. Soc.* **2016**, *138*, 8824.

(94) Chen, W. C.; Song, Y. F.; Wang, C. C.; Liu, Y.; Morris, D. T.; Pianetta, P. A.; Andrews, J. C.; Wud, H. C.; Wu, N. L.; *J. Mater. Chem. A* **2013**, *1*, 10847.

(95) Liu, H. D.; Chen, Y.; Hy, S.; An, K.; Venkatachalam, S.; Qian, D.; Zhang, M.; Meng, Y. S. *Adv. Energy Mater.* **2016**, 1502143.

(96) Armstrong, A. R.; Holzapfel, M.; Novak, P.; Johnson, C. S.; Kang, S. H.; Thackeray, M. M.; Bruce, P. G. *J. Am. Chem. Soc.* **2006**, *128*, 8694.

(97) Zhang, J.; Guo, X.; Yao, S.; Zhu, W.; Qiu, X. *J. Power Sources* **2013**, *238*, 245.

(98) Song, B.; Sui, T.; Ying, S.; Li, L.; Lu, L.; Korsunsky, A. M. *J. Mater. Chem. A* **2015**, *3*, 18171.

(99) Wilson, J. R.; Cronin, J. S.; Duong, A. T.; Rukes, S.; Chen, H. Y.; Thornton, K.; Mumm, D. R.; Barnett, S. A. *J. Power Sources* **2010**, *195*, 1829.

(100) Jinnai, H.; Koga, T.; Nishikawa, Y.; Hashimoto, T.; Hyde, S. *Phys. Rev. Lett.* **1997**, *78*, 2248.

(101) Lim, C.; Yan, B.; Yin, L.; Zhu, L. *Electrochim. Acta* **2012**, *75*, 279.

(102) Adler, S. B. *Chem. Rev.* **2004**, *104*, 4791.

(103) Liao, P.; Carter, E. A. *Chem. Soc. Rev.* **2013**, *42*, 2401.

(104) Huang, R.; Ikuhara,Y. H.; Mizoguchi, T.; Findlay, S. D.; Kuwabara, A.; Fisher, C. A. J.; Moriwake, H.; Oki, H.; Hirayama, T.; Ikuhara, Y. *Angew. Chem. Int. Ed.* **2011**, *50*, 3053.

(105) Okamoto, Y. *J. Electrochem. Soc.* **2012**, *159*, A152.

(106) Sushko, P. V.; Rosso, K. M.; Zhang, J.-G.; Liu, J.; Sushko, M. L. *Adv. Funct. Mater.* **2013**, *23*, 5530.

(107) Kim, J.-H.; Myung, S.-T.; Yoon, C. S.; Kang, S. G.; Sun, Y.-K. *Chem. Mater.* **2007**, *16*, 904.

(108) Jung, S.-K.; Gwon, H.; Hong, J.; Park, K.-Y.; Seo, D.-H.; Kim, H.; Hyun, J.; Yang, W.; Kang, K. *Adv. Energy Mater.* **2014**, *4*, 201300787.

(109) Lin, F.; Markus, I. M.; Nordlund, D.; Weng, T.-C.; Asta, M. D.; Xin, H. L.; Doeff, M. M. *Nature Commun.* **2014**, *5*, 3529.

(110) Yu, H.; Ishikawa, R.; So, Y.-G.; Shibata, N.; Kudo, T.; Zhou, H.; Ikuhara, Y. *Angew. Chem. Int. Ed.* **2013**, *52*, 5969.

(111) Rossouw, M. H.; Thackeray, M. M. *Mater. Res. Bull.* **1991**, *26*, 463.

(112) Xia, Q.; Zhao, X.; Xu, M.; Ding, Z.; Liu, J.; Chen, L.; Iveyb, D. G.; Wei, W. *J. Mater. Chem. A* **2015**, *3*, 3995.

(113) Koga, H.; Croguennec, L.; Ménétrier, M.; Douhil, K.; Belin, S.; Bourgeois, L.; Suard, E.; Weill, F.; Delmas, C. *J. Electrochem. Soc.* **2013**, *160*, A786.

(114) Koga, H.; Croguennec, L.; Ménétrier, M.; Mannessiez, P.; Weill, F.; Delmas, C. *J. Power Sources* **2013**, *236*, 250.

(115) Sathiya, M.; Ramesha, K.; Rousse, G.; Foix, D.; Gonbeau, D.; Prakash, A. S.; Doublet, M. L.; Hemalatha, K.; Tarascon, J.-M. *Chem. Mater.* **2013**, *25*, 1121.

(116) Oishi, M.; Yogi, C.; Watanabe, I.; Ohta, T.; Orikasa, Y.; Uchimoto, Y.; Ogumi, Z. *J. Power Sources* **2015**, *276*, 89.

(117) Kubota, K.; Kaneko, T.; Hirayama, M.; Yonemura, M.; Imanari, Y.; Nakane, K.; Kanno, R.; *J. Power Sources* **2012**, *216*, 249.

(118) Song, B.; Liu, H.; Liu, Z.; Xiao, P.; Lai, M. O.; Lua, L. *Sci. Rep.* **2013**, *3*, 3094.

(119) Kang, S. H.; Johnson, C. S.; Vaughey, J. T.; Amine, K.; Thackeray, M. M. *J. Electrochem. Soc.* **2006**, *153*, A1186.

(120) Zhao, J.; Huang, R.; Gao, W.; Zuo, J.-M.; Zhang, X. F.; Misture, S. T.; Chen, Y.; Lockard, J. V.; Zhang, B.; Guo, S.; Khoshi, M. R.; Dooley, K.; He, H.; Wang Y. *Adv. Energy Mater.* **2015**, *5*, 201401937.

(121) Yu, D. Y. W.; Yanagida, K.; Nakamura, H. *J. Electrochem. Soc.* **2010**, *157*, A1177.

(122) Sun, Y.-K.; Lee, M.-J.; Yoon, C. S.; Hassoun, J.; Amine, K.; Scrosati, B. *Adv. Mater.* **2012**, *24*, 1192.

(123) Villevieille, C.; Lanz, P.; Bünzli, C.; Novák, P. *J. Mater. Chem. A* **2014**, *2*, 6488.

(124) An, K.; Wang, X. L.; Stoica, A. D. *ORNL Report*, **2012**, 621.

(125) Toby, B. H. *J. Appl. Crystallogr.* **2001**, *34*, 210.

(126) Pearson, D. H.; Ahn, C. C.; Fultz, B. *Phys. Rev. B: Condens. Matter Mater. Phys.* **1993**, *47*, 8471.

(127) Kraft, S.; Stümpel, J.; Becker, P.; Kuetgens, U. *Rev. Sci. Instrum.* **1996**, *67*, 681.

(128) Lanz, P.; Sommer, H.; Schulz-Dobrick, M.; Novák, P. *Electrochim. Acta* **2013**, *93*, 114.

(129) Castel, E.; Berg, E. J.; El Kazzi, M.; Novák, P.; Villevieille, C. *Chem. Mater.* **2014**, *26*, 5051.

(130) Kresse, G.; Joubert, D. *Phys. Rev. B* **1999**, *59*, 1758.

(131) Kresse, G.; Furthmüller, J. *Comp. Mater. Sci.* **1996**, *6*, 15.

(132) Kresse, G.; Furthmüller, J. *Phys. Rev. B* **1996**, *54*, 11169.

(133) Kresse, G.; Hafner, J. *Phys. Rev. B* **1994**, *49*, 14251.

(134) Perdew, J. P.; Burke, K.; Wang, Y. *Phys. Rev. B* **1996**, *54*, 16533.

(135) Hinuma, Y.; Meng, Y. S.; Kang, K.; Ceder, G. *Chem. Mater.* **2007**, *19*, 1790.

(136) Yabuuchi, N.; Yoshii, K.; Myung, S. T.; Nakai, I.; Komaba, S. *J. Am. Chem. Soc.* **2011**,

133, 4404.

(137) Qiu, B.; Wang, J.; Xia, Y.; Wei, Z.; Han, S.; Liu, Z. *ACS Appl. Mater. Interfaces* **2014**, *6*, 9185.

(138) Liu, H.; Fell, C. R.; An, K.; Cai, L.; Meng, Y. S. *J. Power Sources* **2013**, *240*, 772.

(139) Armand, M.; Tarascon, J.-M. *Nature* **2008**, *451*, 652.

(140) Palacin, M. R. *Chem. Soc. Rev.* **2009**, *38*, 2565.

(141) Whittingham, M. S. *Chem. Rev.* **2014**, *114*, 11414.

(142) Qiu, B.; Zhang, M.; Xia, Y.; Liu, Z.; Meng, Y. S. *Chem. Mater.* **2017**, *29*, 908.

(143) Saubanère, M.; McCalla, E.; Tarascon, J. M.; Doublet, M. L. *Energy Environ. Sci.* **2016**, *9*, 984.

(144) Jarvis, K. A.; Deng, Z.; Allard, L. F.; Manthiram, A.; Ferreira, P. J. *Chem. Mater.* **2011**, *23*, 3614.

(145) Fell, C. R.,; Chi, M.; Meng, Y. S.; Jones, J. L. *Solid State Ionics* **2012**, *207*, 44.

(146) Bréger, J.; Meng, Y. S.; Hinuma, Y.; Kumar, S.; Kang, K.; Shao-Horn, Y.; Ceder, G.; Grey C. P. *Chem. Mater.* **2006**, *18*, 4768.

(147) Croy, J. R.; Gallagher, K. G.; Balasubramanian, M.; Chen, Z.; Ren, Y.; Kim, D.; Kang, S. H.; Dees, D. W.; Thackeray, M. M. *J. Phys. Chem. C* **2013**, *117*, 6525.

(148) Mohanty, D.; Sefat, A. S.; Li, J.; Meisner, R. A.; Rondinone, A. J.; Payzant, E. A.; Abraham, D. P.; Wood, D. L.; Daniel, C. *Phys. Chem. Chem. Phys.* **2013**, *15*, 19496.

(149) Genevois, C.; Koga, H.; Croguennec, L.; Ménétrier, M.; Delmas, C.; Weill, F.; *J. Phys. Chem. C* **2015**, *119*, 75.

(150) Singer, A. Zhang, M.; Hy, S.; Cela, D.; Fang, C.; Wynn, T. A.; Qiu, B.; Xia, Y.; Liu, Z.; Ulvestad, A.; Hua, N.; Wingert, J.; Liu, H.; Sprung, M.; Zozulya, A. V.; Maxey, E.; Harder, R.; Meng, Y. S.; Shpyrko, O. G. *arXiv*, **2017**, 1706.03031.

(151) Croy, J. R.; Balasubramanian, M.; Gallagher, K. G.; Burrell, A. K. *Acc. Chem. Res.* **2015**, *48*, 2813.

(152) Oh, P.; Ko, M.; Myeong, S.; Kim, Y.; Cho, J. *Adv. Energy Mater.* **2014**, *4*, 201400631.

(153) Yu, Z.; Shang, S.-L.; Gordin, M. L.; Mousharraf, A.; Liu, Z.-K.; Wang, D. *J. Mater. Chem. A* **2015**, *3*, 17376.

(154) Zheng, F.; Yang, C.; Xiong, X.; Xiong, J.; Hu, R.; Chen, Y.; Liu, M. *Angew. Chem. Inter. Ed.* **2015**, *54*, 13058.

(155) Qiu, B.; Zhang, Q.; Hu, H.; Wang J.; Liu, J.; Xia, Y.; Zeng, Y.; Wang, X.; Liu, Z. *Electrochim. Acta* **2014**, *123*, 317.

(156) Yang, T.-Y.; Wen, W.; Yin G.-Z.; Li X.-L.; Gao M.; Gu Y.-L.; Li L.; Liu Y.; Lin H.; Zhang X.-M.; Zhao B.; Liu T.-K.; Yang Y.-G.; Li Z.; Zhou X.-T.; Gao X.-Y. *Nuclear Sci. Techniques* **2015**, *26*, 020101.

(157) Malashenko, V. V. *Phys. Solid State* **2015**, *57*, 2461.

(158) Yabuuchi, N.; Kim, Y.-T.; Li, H. H.; Shao-Horn, Y. *Chem. Mater.* **2008**, *20*, 4936.

(159) Liu, H.; Chen, Y.; Hy, S.; An, K.; Venkatachalam, S.; Qian, D.; Zhang, M.; Meng, Y. S. *Adv. Energy Mater.* **2016**, 1502143.

(160) Bareño, J.; Lei, C. H.; Wen, J. G.; Kang, S.-H.; Petrov, I.; Abraham, D. P. *Adv. Mater.* **2010**, *22*, 1122.

(161) Williamson, G. K.; Hall, W. H. *Acta Meta.* **1953**, *1*, 22.

(162) Delmas, C.; Fouassier, C.; Hagenmuller, *P. Physica B+C* **1980**, *99*, 81.

(163) Radin, M. D.; Hy, S.; Sina, M.; Fang, C.; Liu, H.; Vinckeviciute, J.; Zhang, M.; Whittingham, M. S.; Meng, Y. S.; Van der Ven, A. *Adv. Energy Mater.* **2017**, *7*, 1602888.

(164) Mills, G.; Jonsson, H. *Phys. Rev. Lett.* **1994**, *72*, 1124.

(165) Kushima, A.; Yildiz, B. *J. Mater. Chem.* **2010**, *20*, 4809.

(166) Malashenko, V. V. *Phys. Solid State* **2007**, *49*, 82.

(167) Etacheri, V.; Marom, R.; Elazari, R.; Salitra, G.; Aurbach, D. *Energy Environ. Sci.* **2011**, *4*, 3243.

(168) Dunn, B.; Kamath, H.; Tarascon, J.-M. *Science*, **2011**, *334*, 928.

(169) Liu, H.; Qian, D.; Verde, M. G.; Zhang, M.; Baggetto, L.; An, K.; Chen, Y.; Carroll, K. J.; Lau, D.; Chi, M.; Veith, G. M.; Meng, Y. S. *ACS Appl. Mater. Inter.* **2015**, *7 (34)*, 19189.

(170) Muldoon, J.; Bucur, C. B.; Gregory, T. *Chem. Rev.* **2014**, *114*, 11683.

(171) Xu, J.; Liu, H.; Meng, Y. S. *Electrochem. Commun.* **2015**, *60*, 13.

(172) Kim, H. S.; Arthur, T. S.; Allred, G. D.; Zajicek, J.; Newman, J. G.; Rodnyansky, A. E.; Oliver, A. G.; Boggess, W. C.; Muldoon, J. *Nat. Commun.* **2011**, *2*, 427.

(173) Li, W. Y.; Li, C. S.; Zhou, C. Y.; Ma, H.; Chen, J. *Angew. Chem., Int. Ed.* **2006**, *45*, 6009.

(174) Peng, B.; Liang, J.; Tao, Z.; Chen, J. *J. Mater. Chem.* **2009**, *19*, 2877.

(175) Mizrahi, O.; Amir, N.; Pollak, E.; Chusid, O.; Marks, V.; Gottlieb, H.; Larush, L.; Zinigrad, E.; Aurbach, D. *J. Electrochem. Soc.* **2008**, *155 (2)*, A103.

(176) Huang, S. Y.; Kavan, L.; Exnar, I.; Gratzel, M. *J. Electrochem. Soc.* **1995**, *142*, L142.

(177) Sheha, E. *Int. J. Electrochem. Sci.* **2013**, *8*, 3653.

(178) Su, S. J.; Huang, Z. G.; Nuli, Y.; Tuerxun, F.; Yang, J.; Wang, J. L. *Chem. Commun.* **2015**, *51*, 2641.

(179) Wagemaker, M.; Krol, R.; Kentgens, A.; Well, A.; Mulder, F. M. *J. Am. Chem. Soc.* **2001**, *123*, 11454.

(180) Stashans, A.; Lunell, S.; Bergstrom, R. *Phys. Rev. B.* **1996**, *53*, 159.